SEARCHING FOR OPTICAL COUNTERPARTS TO GRAVITATIONAL WAVES

A Thesis

by

RICHARD CAMUCCIO

Submitted to the Graduate College of
The University of Texas Rio Grande Valley
In partial fulfillment of the requirements for the degree of

MASTER OF SCIENCE

May 2020

Major Subject: Physics

SEARCHING FOR OPTICAL COUNTERPARTS TO GRAVITATIONAL WAVES

A Thesis
by
RICHARD CAMUCCIO

COMMITTEE MEMBERS

Dr. Mario C. Díaz
Chair of Committee

Dr. Juan Madrid
Committee Member

Dr. Nicolas Pereyra
Committee Member

May 2020

ABSTRACT

Camuccio, Richard, Searching for Optical Counterparts to Gravitational Waves. Master of Science (MS), May, 2020, 116 pp., 22 tables, 39 figures, 129 references.

The era of multi-messenger astronomy has begun. The coordinated activities of multiple, distinct observatories play a critical role in both responding to astrophysical transients and building a more comprehensive interpretation otherwise inaccessible to individual observations. The Transient Robotic Observatory of the South (TOROS) Collaboration has a global network of instruments capable of responding to several transient targets of opportunity. The purpose of this thesis is to demonstrate how optical observatories with small fields of view ($<$1 square degree) can follow up and observe astrophysical transients. TOROS facilities responded to three unique gravitational wave events during the second and third observational campaigns of the Laser Interferometer Gravitational-Wave Observatory. We found no optical transients associated with the binary black hole merger GW170104 or the neutron star-black hole merger S190814bv. We detected the optical counterpart AT2017gfo during the follow-up response to the binary neutron star merger GW170817. Elliptical isophote modeling and subtraction of the host galaxy NGC 4993 reveal an isolated optical transient not seen in previous archival data. We performed relative time-series photometry in SDSS *gri*-bands on the detected transient. AT2017gfo exhibits rapid dimming in all bands and color change over the $\sim$1.5 hours of time-series observations. We observe colors of AT2017gfo to be $g-r=0.79\pm0.08$, $r-i=0.23\pm0.08$, and $g-i=1.02\pm0.08$ at $\sim$35 hours post-merger. We calculate the corresponding absolute magnitudes $M_g=-14.40\pm0.06$, $M_r=-15.06\pm0.05$, and $M_i=-15.22\pm0.06$. We observe AT2017gfo to have an angular offset of $\sim$10.4" from the galactic core, corresponding to a linear diameter of $\sim$2 kpc at redshift $z=0.00973$. Although AT2017gfo is generally recognized to be consistent with an r-process-

powered thermal transient, or kilonova, our observations are in partial disagreement with the accepted picture. We address the plausible reasons for the discrepancies in our measurements. We developed a reduction and photometry pipeline during the processing and analysis of data from these events. The CTMO Analysis Pipeline (CAL) is currently at an early phase of operation, with plans for automation and further inclusion of additional analysis methods to optimize the TOROS search and characterization of astrophysical transients.

DEDICATION

This is dedicated to my mother, Deborah.

I am forever grateful for your unconditional love, support, and patience.

To my father, Joseph.

Thank you for teaching me how to stand up for myself and to always do the right thing.

To my sister, Gabrielle.

You inspire me with your endless courage, talent, passion, and fighting spirit.

ACKNOWLEDGMENTS

To Mario Claudio Díaz, for your unwavering support as a research advisor; for being an optimistic, passionate, and fair leader who looks out for his team; for handing me the keys to the observatory; for sending me on adventures to France, Sicily, and Mexico; for being a mentor in both research and in life; for believing in my capabilities and my potential even when I had my doubts.

To Moises Castillo, for helping me take my first steps at Nompuewenu; for being my partner in research; for life-changing adventures in Texas, Louisiana, Colorado, and Sicily; for being a talented astronomer, engineer, and educator; for being my good friend.

To Joseph Romano and Suzanne Lalonde, for being fantastic hosts for two years; for your mentorship, hospitality, and generosity; for accepting me as family and giving me a home in the unknown.

To Martin Beroiz, for your knowledge and guidance as a mentor; for being a role model in research and academics; for patiently helping to get me unstuck in research, writing, and homework.

To Adam Zadrożny, for helping me outline my thesis and guide me in writing; for spending your precious sleeping hours across seven hours of time difference to ask how things are going; for being an inspiring astronomer, programmer, and father.

To the Time Domain Astronomy Group... Wahltyn Rattray, Americo Hinojosa, Andrea Hinojosa, Alejandro Hinojosa, Erick Vallarino, Alan Hendrick, Victor Perez, Wendy Mendoza, Brina Martinez, Tanya Llanas, Martell Valencia, Karina Hernandez, and Abby Martinez. I cannot thank you all enough for the countless observing sessions, observatory events, TDAG meetings, astrophysics seminars, late-night conversations, and giving me more during my time in

Brownsville than I can ever hope to express.

To Carla Giardini, Lupe Duran, Brittany Gomez, Sebastian Colom, and Elizabeth Caputa... I am grateful for having the opportunity to meet and work with you during your time in Brownsville. Each of you left a lasting impression on me that I will carry with me forever.

To Aldo Fonrouge, for making sure I was being nourished with food, good company, and an endless supply of anime and computer knowledge.

To Victor de los Santos, for your friendship, your enthusiasm, your drive, and your selfless generosity.

To Lucas Macri, for your invaluable lessons on photometry and for being a role model in observational astronomy.

To Diego Garcia Lambas, for providing me unique opportunities to observe and for teaching me cosmology.

To Juan Madrid and Nicolas Pereyra, for your willingness to serve as committee members for my thesis and your commitment and belief in helping me build this project.

To Jing Luo, Andy Danford, Andrés Cuéllar, and Keith Böhler... thank you for your companionship and the memories I will cherish forever.

To Kasia Wardęga, for your patience, your compassion, and your willingness to brave this adventure with me.

The Digitized Sky Surveys were produced at the Space Telescope Science Institute under U.S. Government grant NAG W-2166. The images of these surveys are based on photographic data obtained using the Oschin Schmidt Telescope on Palomar Mountain and the UK Schmidt Telescope. The plates were processed into the present compressed digital form with the permission of these institutions. The National Geographic Society - Palomar Observatory Sky Atlas (POSS-I) was made by the California Institute of Technology with grants from the National Geo-

graphic Society. The Second Palomar Observatory Sky Survey (POSS-II) was made by the California Institute of Technology with funds from the National Science Foundation, the National Geographic Society, the Sloan Foundation, the Samuel Oschin Foundation, and the Eastman Kodak Corporation. The Oschin Schmidt Telescope is operated by the California Institute of Technology and Palomar Observatory. The UK Schmidt Telescope was operated by the Royal Observatory Edinburgh, with funding from the UK Science and Engineering Research Council (later the UK Particle Physics and Astronomy Research Council), until 1988 June, and thereafter by the Anglo-Australian Observatory. The blue plates of the southern Sky Atlas and its Equatorial Extension (together known as the SERC-J), as well as the Equatorial Red (ER), and the Second Epoch [red] Survey (SES) were all taken with the UK Schmidt. All data are subject to the copyright given in the copyright summary. Copyright information specific to individual plates is provided in the downloaded FITS headers. Supplemental funding for sky-survey work at the ST ScI is provided by the European Southern Observatory.

TABLE OF CONTENTS

Page

LIST OF TABLES

Page

LIST OF FIGURES

CHAPTER I

INTRODUCTION

We have entered the era of multi-messenger astronomy (MMA). The field of MMA involves the contribution of multiple instruments, each using distinct observational "channels" or "messengers" and positioned at different locations, in order to observe the same astrophysical event. Having multiple channels of observation for a single event provides a comprehensive view into the astrophysics of the event that would otherwise be inaccessible for a single instrument. The multi-messengers can be similar in nature, like two instruments observing light at different wavelengths, or quite distinct, like coincident observations using different forces of nature (e.g. gravity and photons).

We cannot place the birth of MMA on a single day in history. There are several discoveries that have marked unprecedented breakthroughs in observational MMA that have led to the current paradigm. I will highlight five such breakthroughs all occurring within the span of three decades. These events are the supernova 1987A, the GRB of 28 February 1997, the second GRB of 3 June 2013, the GW of 17 August 2017, and the high-energy neutrino event IceCube-170922A of 22 September 2017. These five MMA breakthrough events are summarized in Table 1.1.

The supernova (SN) 1987A was discovered on 24 February 1987 by Ian Shelton and Oscar Duhalde at Las Campanas Observatory in Chile and Albert Jones in New Zealand [83]. Subsequent optical/infrared photometry and spectroscopy were carried out by several independent observers of SN 1987A over the following days and months. These observations determined SN 1987A to be a Type II supernova, having occurred in the Large Magellanic Cloud $\sim$ 51.4 kiloparsecs from Earth, and possessing large infrared excess [29] [30] [36] [90] [114]. The progenitor of SN 1987A was the B3 supergiant Sanduleak -69 202 in the constellation Dorado [126].

At 07:35 UT on 23 February 1987, three neutrino observatories detected a 13-second burst of 25 anti-neutrinos. The Kamioka Observatory detected 12 anti-neutrinos, Irvine-Michigan-Brookhaven detected eight, and the Baksan Neutrino Observatory detected five [17]. Not only did this remarkable coincident discovery mark the beginning of neutrino astronomy, but I would argue that it also signified the birth of MMA. Two distinct observational channels — EM radiation and neutrino interaction — were used for the first time in a single astronomical measurement.

On 28 February 1997 at 02:58 UT the Gamma-Ray Burst Monitor onboard the Giuseppe "Beppo" Occhialini Satellite per Astronomia a raggi X (BeppoSAX) detected an $\sim$ 80-second gamma-ray burst (GRB) centered at $\alpha =$ 05:01:57 and $\delta =$ +11:46.4with an error radius of three arcseconds. The BeppoSAX Low and Medium Energy Concentrator Spectrometers observed a spatially-coincident X-ray source 1SAX J0501.7+1146 at $\sim$ eight hours post-burst at position $\alpha =$ 05:01:44 and $\delta =$ +11:46.7 and with a 50 arcsecond radius of error. The 4.2-meter William Herschel Telescope (WHT) took 300-second V- and I-band exposures on 28 February 1997 at 23:48 UT in follow-up to the GRB in order to localize a potential optical counterpart. Additionally, the WHT obtained a second 900-second I-band reference image on 8 March at 21:12 UT and the 2.5-meter Isaac Newton Telescope obtained a 2500-second V-band reference on 8 March at 20:42 UT. Comparison of initial observations with these references showed a fading optical transient within the error box of the GRB, at a position consistent with the X-ray source, and appearing associated with a faint galaxy. The optical transient was found at position $\alpha =$ 05:01:46.66 and $\delta =$ +11:46:53.9, the first time a GRB was localized to that level of precision. The X-ray and optical counterparts to GRB 970228 were the first discovered EM counterparts of a GRB [42] [43] [121].

On 3 June 2013 at 15:49:14 UT the Burst Alert Telescope onboard NASA's Neil Gehrels *Swift* Observatory and the Konus-Wind satellite detected a short gamma-ray burst (sGRB). GRB 130603B lasted $\sim$ 0.4 seconds and had a single-spike structure with a peak rate of $\sim$ 60000 counts per second in the 15-350 keV band. The sGRB was initially localized to position $\alpha =$ 11:28:50 and $\delta =$ +17:02:42 with a three-arcsecond radius of uncertainty. The *Swift* X-ray tele-

scope conducted observations $\sim$ 59 seconds post-trigger and detected a source with an enhanced position α = 11:28:48.16 and δ = +17:04:18.8 with a 2.7-arcsecond radius of uncertainty. The centers of each localization were separated by 101 seconds of arc with overlapping error circles, allowing for more precise follow-up efforts. The center of GRB 130603B was offset $\sim$ 12 arcseconds from the galaxy NGC 3691 at redshift $z = 0.003566$ [62] [88]. Several follow-up efforts, including ground and Hubble Space Telescope (HST) observations, detected a fading, near-infrared (NIR) transient [35] [38] [45] [47] [76]. The observed NIR excess faded rapidly between $t \approx 8 - 32$ hours post-trigger and matched the expected brightness and color of an r-process-powered thermal transient, or "kilonova" (see Chapter 2.2). The detection of GRB 130603B and an optical counterpart consistent with kilonova models provided early support for the compact merger hypothesis being the origin of sGRBs, and is considered the first plausible observation of a kilonova [23] [111].

The first detection of gravitational waves (GWs) in 2015 from a binary black hole (BBH) merger by the Laser Interferometer Gravitational-Wave Observatory (LIGO) was followed two years later on 17 August 2017 by the first detection of GWs from a binary neutron star (BNS) merger. The Fermi and INTEGRAL satellites observed an sGRB $\sim$ 1.7 seconds after the detection of GW170817. Several teams responded to survey the overlapping localization regions of the GW and GRB 170817A for a potential counterpart. An optical transient was discovered by responding teams $\sim$ 11 hours post-merger, officially AT2017gfo, and was subsequently observed across every wavelength in the EM spectrum. These observations supported the hypothesis of BNS mergers as the cause of GW170817 (as well as sGRBs in general) and a kilonova as the most plausible explanation for AT2017gfo. The details of this particular event are further discussed in Chapters 2.1 and 2.2. Regardless, the unprecedented significance of this first multi-messenger GW-EM observation cannot be dismissed. Never before has an object in the universe been observed so extensively across so many coincident channels at once.

The IceCube Neutrino Observatory detected a high-energy ($\sim$ 290 TeV) neutrino called "IceCube-190722A" on 22 September 2017 at 20:54:30.43 UT. Reconstruction of the neutrino

direction produced an incident position $\alpha \approx 77.43$ and $\delta \approx +5.72$. The source location was consistent with that of a known BL Lacertae-type gamma-ray blazar TXS 0506+056 at redshift $z = 0.3365$ and position $\alpha \approx 77.3$ and $\delta \approx +5.69$. The Fermi Large Area Telescope observed the blazar on 28 September 2017 and found it in a flaring state, evidently having been in one since April 2017 according to observational record. Over the course of days and weeks following the coincident detection, follow-up teams observed TXS 0506+056 across all wavelengths of the EM spectrum. The discovery of a spatially- and temporally-coincident high-energy neutrino and gamma-ray flare-up in a blazar suggests that these sites are the source of high-energy cosmic rays, a previously-unresolved question in high-energy astrophysics. Furthermore, astrophysical neutrinos were only previously observed from the Sun and SN 1987A, so the discovery of IceCube-170922A and the associated TXS 0506+056 flare-up was the third observation of a neutrino from a known astrophysical source [1].

Date	Event	Observational channels
23 Feb 1987	SN 1987A	EM (γ, X, UVOIR, radio) + ν
28 Feb 1997	GRB 970228	EM (γ, X, optical, IR)
3 Jun 2013	GRB 130603B	EM (γ, X, optical, IR)
17 Aug 2017	GW170817 GRB 170817A AT2017gfo	GW + EM (γ, X, UVOIR, radio)
22 Sep 2017	IceCube-170922A TXS 0506+056	ν + EM (γ, X, UVOIR, radio)

Table 1.1: Multi-messenger astronomy milestones.

Although the concept of MMA is not new, we have certainly entered an era of MMA involving the coordinated activities among several types of observatories spread all over the world and in space. The ability to respond to transient astrophysical events is an important feature any observatory must equip to participate in these time-sensitive moments, or "targets of opportunity" (TOO). *Time domain astronomy* deals with any astrophysical event that changes in time. Transient events occur over a wide range of timescales [25]. Transients such as fast radio bursts (FRBs) and GRBs can occur over $\sim$ millisecond-second timescales. Other bursts such as kilonovae and supernovae can occur from hours and days to over months and years.

Large optical observatories are much better at covering more ground and depth faster than smaller observatories. Larger optical systems are more sensitive, in much better locations, and handled by many more specialists. However, large observatories are typically limited by available telescope time useful for both long-term transient surveys and responding to TOOs, the latter which might occur at a rate of several times per month. Typically, participating astronomers in these large facilities have access to a limited schedule throughout the year. Teams with telescope time might have TOO status approval for only a few hours for a given scheduling term lasting a quarter of a year or more. The limited observing time at large facilities proves to be cumbersome in responding to events that need to be observed over long duration, such as GW triggers or GRBs, which might involve a rapidly-fading optical or IR transient on the order of days or weeks. Time is the most precious resource. Extensive follow-up campaigns are better handled by smaller, more time-available facilities. Small observatories can provide critical and robust data in following up TOOs and conducting longer-term measurements of detected yet unclassified sources. The limitations of small observatories become those of instrumentation quality, site conditions, and post-observational analysis methods.

The challenge I am addressing is — *How can small astronomical observatories follow-up and observe astrophysical transients?* The purpose of this thesis is to demonstrate (1) how an astronomical observatory should respond to a GW event, (2) how one should process the imaging data obtained during such a follow-up, and (3) how one measures the optical counterpart to a GW, should one be discovered in response to a GW alert.

In Chapter 2, I discuss the historical attempt to detect GWs, the discovery of GWs in 2015, and the detection of GW170817 and measurements of the associated counterparts GRB 170817A and AT2017gfo. I provide a summary of kilonovae and AT2017gfo, the optical counterpart of GW170817. In Chapter 3, I describe the methods required for observing optical counterparts to GWs. I show how one measures the properties of the CCD imaging system (for selecting a proper optical system to see a transient) and the signal of a stellar source (which a transient would look like, albeit rapidly-fading). I demonstrate how one estimates the angular offset of an

object out to nearby ($z \lesssim 0.1$) galaxies, since we expect many BNS mergers, and hence many thermal transients, to occur within or nearby galaxies. In Chapter 4, I discuss the TOROS project and the development of the Cristina Torres Memorial Observatory (CTMO). In Chapter 5, I present data from the observational response to three GW events between 2017 and 2019. I perform relative time-series photometry on the detected transient AT2017gfo and measure its angular offset from the center of its galactic host. In Chapter 6, I discuss the validity of my measurements. I remark on the implications of GW170817 on the ability of CTMO and the TOROS network to conduct observational follow-ups to transient events. I present my sources of error, intended areas of improvement, and summarize the project.

CHAPTER II

BACKGROUND

2.1 Gravitational waves

Albert Einstein published the theory of general relativity in 1915 and conjectured the existence of GWs in 1916 [59]. GWs are traveling perturbations in the spacetime metric caused by very massive or energetic events. At the suggestion of Hermann Weyl, by changing coordinate systems, Einstein demonstrated the existence of three kinds of GWs. Arthur Eddington showed in 1922 that two of the three types of conjectured waves were coordinate artifacts [57]. Einstein and Nathan Rosen demonstrated the existence of cylindrical GWs in 1937, although the question as to whether or not GWs carry energy was still up for debate, and would not be settled for another two decades [60]. In 1956 Felix Pirani predicted the observable properties of GWs and demonstrated that a passing wave should move particles back and forth [37] [99]. The 1957 Chapel Hill Conference at University of North Carolina featured Richard Feynman giving his "sticky bead argument" which, in tandem with Pirani's work, convinced most physicists that GWs carry energy [37].

Joseph Weber proposed the detection of GWs by measuring resonant vibrations induced in a large metal cylinder as the waves pass [124]. Weber constructed two aluminum cylinders, each 66 centimeters in diameter, 153 centimeters in length, and weighing three tons. Each cylinder was suspended by steel wire in a vacuum chamber and separated by 950 kilometers. Unfortunately, their sensitivity was limited by thermal agitation in the mechanical system to relative changes in length $\sim 10^{-16}$, which is above the sensitivity necessary to detect GWs [37]. Indirect evidence for GWs came with Hulse and Taylor's 1974 discovery of the binary pulsar PSR B1913+16 [68]. The orbital behavior of PSR B1913+16 demonstrated evidence of energy loss as

expected from GW emission for a decaying binary system [113].

A global network of ground-based Michelson interferometers is currently observing the GW sky. The Laser Interferometer Gravitational-Wave Observatory (LIGO) operates two such interferometers in the United States, the LIGO Livingston Observatory (LLO) in Livingston, Louisiana, and the LIGO Hanford Observatory (LHO) in Hanford, Washington (see Figures 2.1 and 2.2) [10]. Each LIGO detector is a Michelson interferometer in perpendicular "L-shaped" configuration (see Figure 2.4). The length L of each LIGO arm is 4 kilometers. The suspended mirrors act as "freely-falling" test masses in horizontal planes for frequencies much larger than the swinging frequency of the pendulum [10] [100]. Following a remarkable and rich history of development over the span of four decades, LIGO is currently sensitive to changes in arm length $\Delta L \sim 10^{-18}$ meters, or roughly 1000 times smaller than the diameter of a proton. To quote Clarke's Third Law, *"Any sufficiently advanced technology is indistinguishable from magic."* Given that the strain h is calculated from $2\Delta L/L$, a GW detector with 4-kilometer-long arms and a sensitivity to changes in length $\sim 10^{-18}$ meters should be sensitive to strains $h \sim 10^{-21}$ [100]. LIGO is currently in its advanced stage (aLIGO) following a series of testing runs and technological upgrades [2]. The Virgo Collaboration operates a similar detector in Cascina, near Pisa in Italy — a Michelson interferometer with 3 kilometer-long arms [11]. Virgo has also entered its advanced stage of observations [12].

The LIGO-Virgo Collaboration (LVC) can detect the GWs emitted from compact binary coalescence (CBC). The cases of CBC expected are BNS mergers, BBH mergers, and binary neutron star-black hole (NSBH) mergers. Currently, the Advanced LIGO-Virgo network can detect CBC from these types of events out to several hundreds of megaparsecs [8]. Every stage of upgrades yields a greater sensitivity to detect CBC (see Table 2.1). The planned "aLIGO+" will have a BNS range of 325 Mpc and a BBH range of 2563 Mpc [100].

The first observing run (O1) of LIGO was from 12 September 2015 to 19 January 2016. LIGO started its second observing run (O2) on 30 November 2016. Advanced Virgo began its first observational campaign on 1 August 2017, joining LIGO during the last few weeks of its O2

Phase	BNS range [Mpc]	BBH range [Mpc]
Early	40-80	415-775
Mid	80-120	775-1110
Late	120-170	1110-1490
Design	190	1640
Plus	325	2563

Table 2.1: Phases of plausible target detector sensitivities. Adapted from Table 1 of Abbott et al (2018) with added terms from Quetschke (2019).

campaign — the first time three GW detectors were operating together. The concurrent LIGO-Virgo O2 campaign ended on 25 August 2017. At the time of writing (January 2020), the LIGO and Virgo detectors have been operating for the third observing run (O3) since 1 April 2019. The LLO and LHO took a month-long commissioning break, which concluded on 1 November 2019, and O3 will continue until 30 April 2020. Beyond this time, the GW network will observe yearly as it reaches full design sensitivity, with O4 beginning at the end of 2020 and the planned addition of LIGO-India in 2024 [8].

Figure 2.1: The Livingston detector site of LIGO. Credit: Caltech/MIT/LIGO Lab.

The LHO, LLO, and Virgo Observatory form a global network of GW detectors, along with other detectors at various stages of development (see Figure 2.3 for a current picture of the global network). Why should we have multiple detectors? Having more than one detector observing the same event provides coincidence, and hence confidence, of a true astrophysical detection.

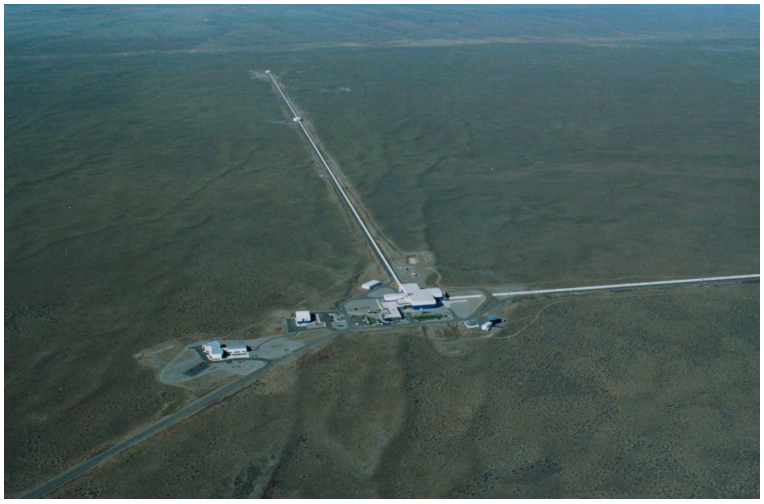

Figure 2.2: The Hanford detector site of LIGO. Credit: Caltech/MIT/LIGO Lab.

Given three or more detectors, we can reduce the localization uncertainty on the sky and improve the chances of observing the GW source progenitor. Finally, if we have at least two detectors rotated 45 degrees relative to each other, we maximize our sensitivity to both GW polarization modes [8] [100].

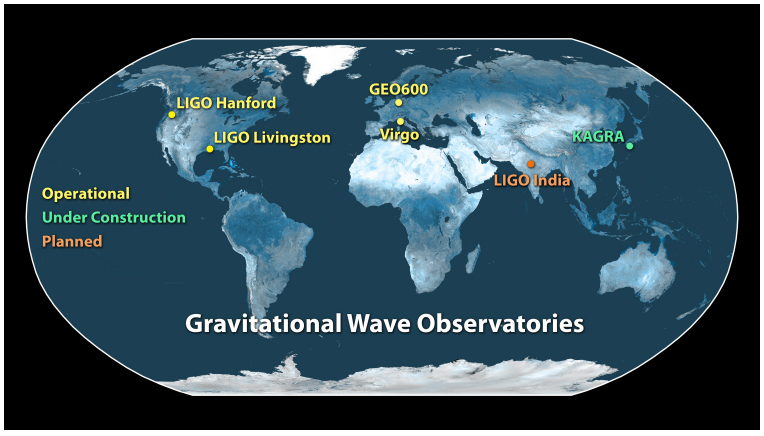

Figure 2.3: The global distribution of gravitational wave detectors. Credit: Caltech/MIT/LIGO Lab.

The era of GW astronomy began on 14 September 2015 at 09:50:45 UT when both LIGO facilities detected GWs from a BBH merger. The discovery was remarkable for demonstrating the existence of binary stellar-mass black hole systems, observing one merge, and for being the first direct detection of GWs [3]. Equally remarkable was that GW150914 showed that rela-

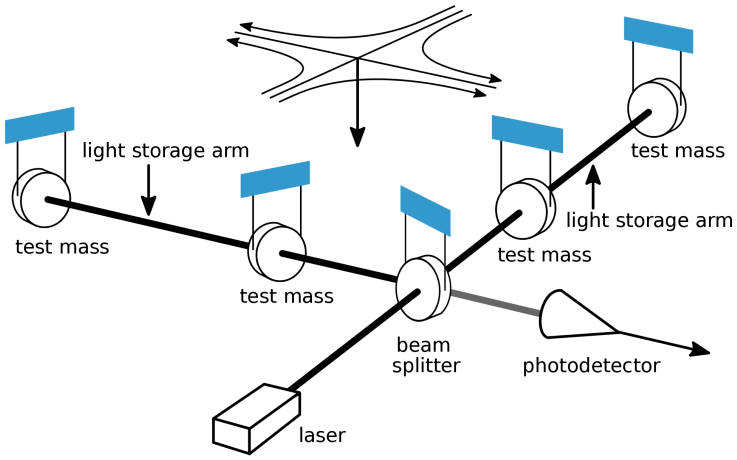

Figure 2.4: Cartoon schematic of a gravitational wave laser interferometer. Credit: MOBle, Wikimedia Commons.

tively "heavy" stellar-mass black holes ($\gtrsim 25M_\odot$) form in nature [4]. The measured properties of GW150914 are in Table 2.2.

Initial masses	$36M_\odot$ and $29M_\odot$
Final mass	$62M_\odot$
Total energy radiated	$3M_\odot c^2$
Frequency sweep	35-250 Hz
In-band timescale	~ 150 ms
Peak GW luminosity	3.6×10^{56} erg/s
Distance	410 Mpc
Redshift	$z = 0.09$
Peak strain	$h \sim 1.0 \times 10^{-21}$
Signal-to-noise ratio	~ 24
False alarm rate	1 in 2.03×10^5 yrs
Significance	5.1σ

Table 2.2: GW150914 properties. Adapted from Abbott et al (2016) and Quetschke (2019).

On 17 August 2017 at 12:41:04 UTC the Advanced LIGO and Virgo detectors observed the first BNS merger. GW170817 had a signal-to-noise ratio (SNR) of ~ 32.4 and false alarm rate of 1 in 8.0×10^4 years. The component masses were both calculated to be in the range $1.17 - 1.60M_\odot$ implying the progenitors were both likely to be neutron stars. The GW signal was localized to within 28 deg^2 at 90% confidence and estimated to have a luminosity distance of ~ 40 Mpc [6].

Approximately 1.7 seconds following the detection of GW170817, the Fermi Gamma-Ray Burst Monitor (Fermi-GBM) and INTEGRAL satellites detected a sGRB [40] [105] [7] [6]. The sGRB uncertainty region overlapped that of the GW, improving overall localization estimates for follow-up observations. The near-simultaneous spatial and temporal localization of GW170817 and GRB 170817A had a 1 in 5.0×10^{-8} chance of occurring randomly and, hence, is strong evidence for the link between BNS mergers being the progenitors of sGRBs [6] [7].

An IceCube neutrino candidate was initially determined to be coincident with GW170817, but an updated GW skymap showed no coincidence of any plausible neutrino event [20] [21]. X-ray [61] [117] and radio [41] [95] counterparts were detected and observed over the following weeks and months.

Subsequent follow-up observations detected an optical counterpart named AT2017gfo $\sim$ 11 hours post-merger approximately 10 arcseconds from the galaxy NGC 4993 [15] [16] [24] [44] [50] [89] [112] [118] [119] [129]. Cross-matching HST imaging with the Gaia astrometric catalog gave the position of AT2017gfo to be $\alpha =$ 13:09:48.071 and $\delta =$ -23:22:53.37 [13]. The observation of GWs and EM radiation from the same source was an unprecedented milestone in astronomy and marked a new phase in the era of MMA. The observation of GW170817 and its associated EM counterpart was one of the most important observations in the history of astronomy.

The results from three CBC searches ($> 1M_{\odot}$) during O1 and O2 include 10 BBHs detections and 1 BNS detection. No NSBH detections were made. The results are summarized in the First Gravitational Wave Transient Catalog (GWTC-1) of Compact Binary Mergers [9]. A representative skymap of GWTC-1 is shown in Figure 2.6 and the GW waveforms and frequency plots are shown in Figure 2.7.

2.2 Compact binary coalescence

The compact objects in either a BNS or NSBH system will inevitably collide after losing sufficient rotational energy to gravitational radiation. When two neutron stars or a neutron star and black hole collide, they produce a significant amount of ejected mass caused by the intense

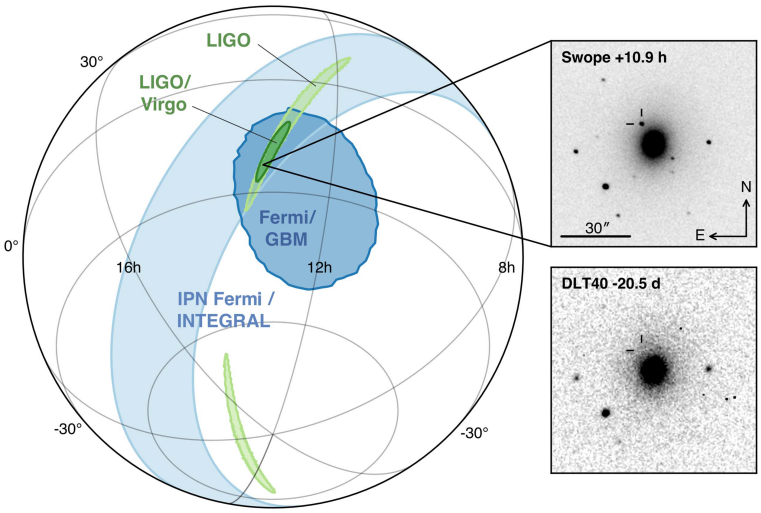

Figure 2.5: Localization skymaps of GW170817 detected by LIGO and Virgo and GRB 170817A detected by Fermi and INTEGRAL. Images of optical counterpart AT2017gfo by Swope Supernova Survey and reference field by DLT40 collaboration. Credit: LIGO Scientific Collaboration and Virgo Collaboration.

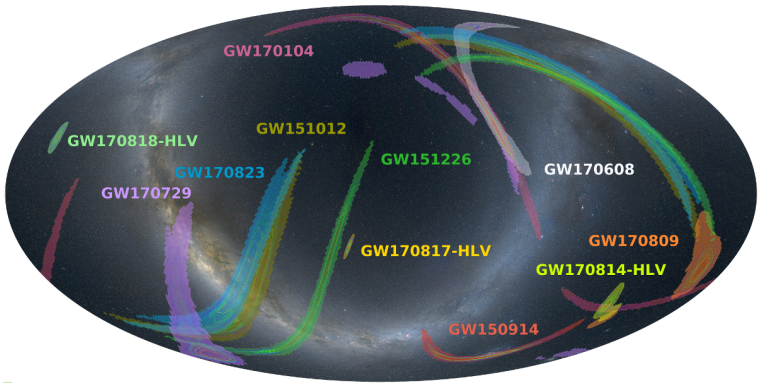

Figure 2.6: Skymap of all GW localizations in the LIGO/Virgo first and second observing runs. Credit: Virgo Collaboration.

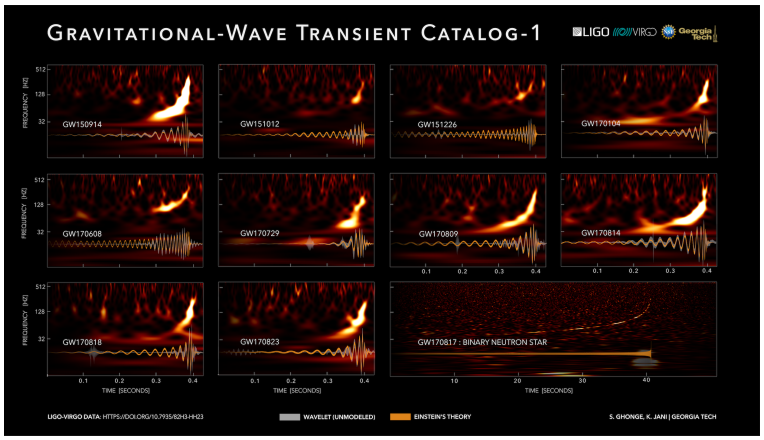

Figure 2.7: The Gravitational Wave Transient Catalog of Compact Binary Mergers. Credit: LIGO/Virgo/Georgia Tech/S. Ghonge & K. Jani.

tidal forces between the two objects. Even with one progenitor being a black hole, enough matter can be broken up outside the event horizon and ejected at sub-relativistic or relativistic velocities [75] [77] [110]. Within merely a few milliseconds post-merger, there are three morphological regions that can already be identified of the post-merger product, namely (1) a rapidly-spinning central compact object between 2.5-3$M_{\odot}$ which has a high probability of further collapse into a black hole within milliseconds; (2) a thick disk a few tenths of a solar mass surrounding the central object; and (3) a low density region surrounding the thick disk [63].

It is expected that an EM counterpart will accompany a GW if one of the progenitors is a neutron star [75]. A summary of the potential EM counterparts to a BNS or NSBH merger are found in Figure 2.8, adapted from Metzger & Berger (2012) [93]. BNS mergers should produce bursts of gamma-rays [58]. Two processes can provide the GRB energy, namely (1) neutrino-antineutrino annihilation into electron-positron pairs during the merger and (2) magnetic flares generated by the differentially-rotating post-merger disk [97]. Additionally, numerical simulations show that BNS and NSBH mergers release ultra-relativistic jets and spherical, sub-relativistic ejecta (the latter of which includes dynamically-ejected tidal tails and accretion disk outflows). Non-thermal radio emission is produced from the interaction of outflow with the surrounding interstellar environment. These radio remnants are expected to appear weeks or years after the merger event [93] [96].

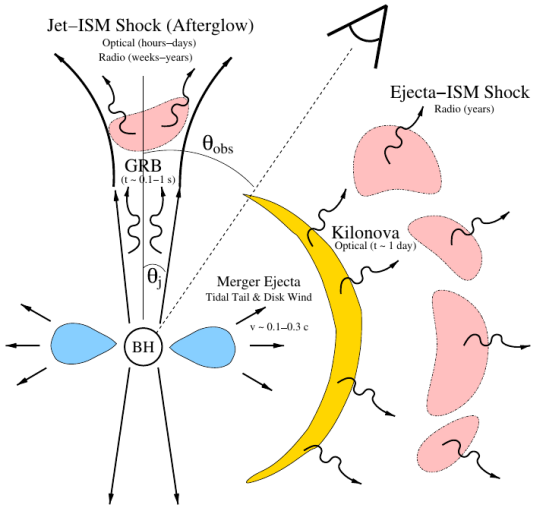

Figure 2.8: Summary of EM counterparts to BNS and NSBH mergers. Figure 1 from Metzger & Berger (2012).

The ejected material contains a high density ($\sim 10^{11}$ to 10^{14} g cm^{-3}) of neutrons which undergoes rapid decompression as the material moves away from the system. Decreased pressure caused by the decompression of neutron-rich material allows neutrons to move more readily and rapidly. Nuclei above the iron group ($A > 90$) require successive capturing of neutrons in order to form. There are two such processes in nature which allow for seed nuclei to capture free neutrons. One such process is the slow neutron capture process (s-process), which occurs in situations if the beta-decay half-life

$$ {}^{A+1}_{Z}\mathrm{X} \rightarrow {}^{A+1}_{Z+1}\mathrm{X} + e^{-} + \bar{\nu}_e + \gamma \tag{2.1} $$

is short compared to the timescale for free neutron capture

$$ {}^{A}_{Z}\mathrm{X} + n \rightarrow {}^{A+1}_{Z}\mathrm{X} + \gamma \tag{2.2} $$

where A is the mass number, Z is the atomic number, and X is the particular species of seed nuclei [33]. The other process is the rapid neutron capture process (r-process), which occurs in situations if the beta-decay half-life is long compared to the neturon capture timescale.

BNS and NSBH mergers, which involve rapid decompression of highly-dense neutron material, are candidate sites for the production of neutron-rich heavy nuclei via the r-process and could account for the entire observable abundances of r-process elements in the universe [58] [63] [75] [77] [110]. In fact, the observations of AT2017gfo are consistent with the inference that BNS mergers are the dominant source of r-process nucleosynthesis in the universe [123].

One of the likeliest sources of isotropic EM emission is a supernova-like transient powered by the radioactive decay of r-process-synthesized elements (e.g. lanthanide elements) in the decompressed material. The r-process heats the material at early ($\lesssim$ 1 second) times, followed by radioactive heating on timescales $\sim$ hours to days produced by fission and β-decay of these synthesized elements. These supernova-like transient counterparts are called *kilonovae*, since their expected peak luminosity is anticipated to be $\sim 10^3$ brighter than a nova. The expected mass ejected is $\sim 10^{-2} M_\odot$ to $\sim 10^{-3} M_\odot$, the peak timescale is $\sim$ 1 day, and a peak V-band luminosity of $\sim 3 \times 10^{41}$ erg s^{-1} (corresponding to $M_V \approx -15$). The presence of lanthanide elements corresponds to a reddening in color of the kilonova. Observers have been advised to find a transient that exhibits optical emission on the order of days (from lanthanide-free components) and week-long NIR emission (from lanthanide-rich components). Kilonovae are most useful for obtaining redshift and localization information, making them high targets of interest for optical follow-up campaigns [92] [93] [94].

The optical counterpart to GW170817 is consistent with pre-existing kilonova models. The overall UVOIR picture provided by 647 total follow-up measurements was consistent with a spherical, three-component kilonova model ejecting a mass of $\approx 0.078 M_\odot$ at $v \approx 0.15c$. The data are well modeled by (1) a "blue" lanthanide-poor component, (2) an intermediate-opacity "purple" component, and (3) a "red" lanthanide-rich component. The origin of the merger appears to be truly a BNS (and not a NSBH) merger since the lanthanide-poor component indicates material having been dynamically-ejected from the poles during the merger process. What about the fate of the final merger product? The "purple" intermediate-opacity and "red" lanthanide-rich components indicate the presence of delayed outflow from an accretion disk which formed post-merger,

an indication which disfavors a long-lived ($\simeq$ 100 ms) central hypermassive neutron star remnant, and instead favors prompt collapse into a black hole [123].

CHAPTER III

METHOD

3.1 Optical follow-up response

The NASA Goddard Gamma-ray Coordinates Network (GCN) and Transient Astronomy Network (TAN) provide information related to transient astronomical events. The GCN system distributes (1) the locations of GRBs and other transients ("notices") and (2) reports of follow-up observations ("circulars"). Typical event notices are transmitted from various spacecraft (e.g. Fermi), GW detectors (e.g. LIGO), and neutrino detectors (e.g. IceCube) [25].

The TOROS alert robot is a Python script running constantly on a virtual machine. When the LVC detects a GW signal, they issue a GCN notice formatted as a Virtual Observatory Event (VOE) file and sent via the VOEvent Transport Protocol to a list of predefined static IPs and ports [25]. Upon receiving a notice from the LVC, the TOROS alert robot follows three steps. First, the robot sends an email to a subscriber list with the attached VOE file. Next, the robot parses the XML-formatted VOE file and sends a follow-up email with the parsed event parameters, such as event identification, detection time, alert type, probability of involving a neutron star, probability of having a remnant, and a rapid localization skymap by BAYESTAR [107]. Finally, the robot generates a list of targets for each TOROS observatory and uploads the targets to a broker website. The TOROS alert pipeline, designed by M. Beroiz (2017), is shown in Figure 3.1 [25].

The ability to localize a GW source in the sky depends on the geographical configuration of the GW detector network and the relative sensitivity of the detectors. With only two detectors active, localization regions can be as large as ~ 1000 square degrees. Three detectors (all within a factor of $\sim$2 relative sensitivity) are required to improve the localization region to $\sim 5 - 20$

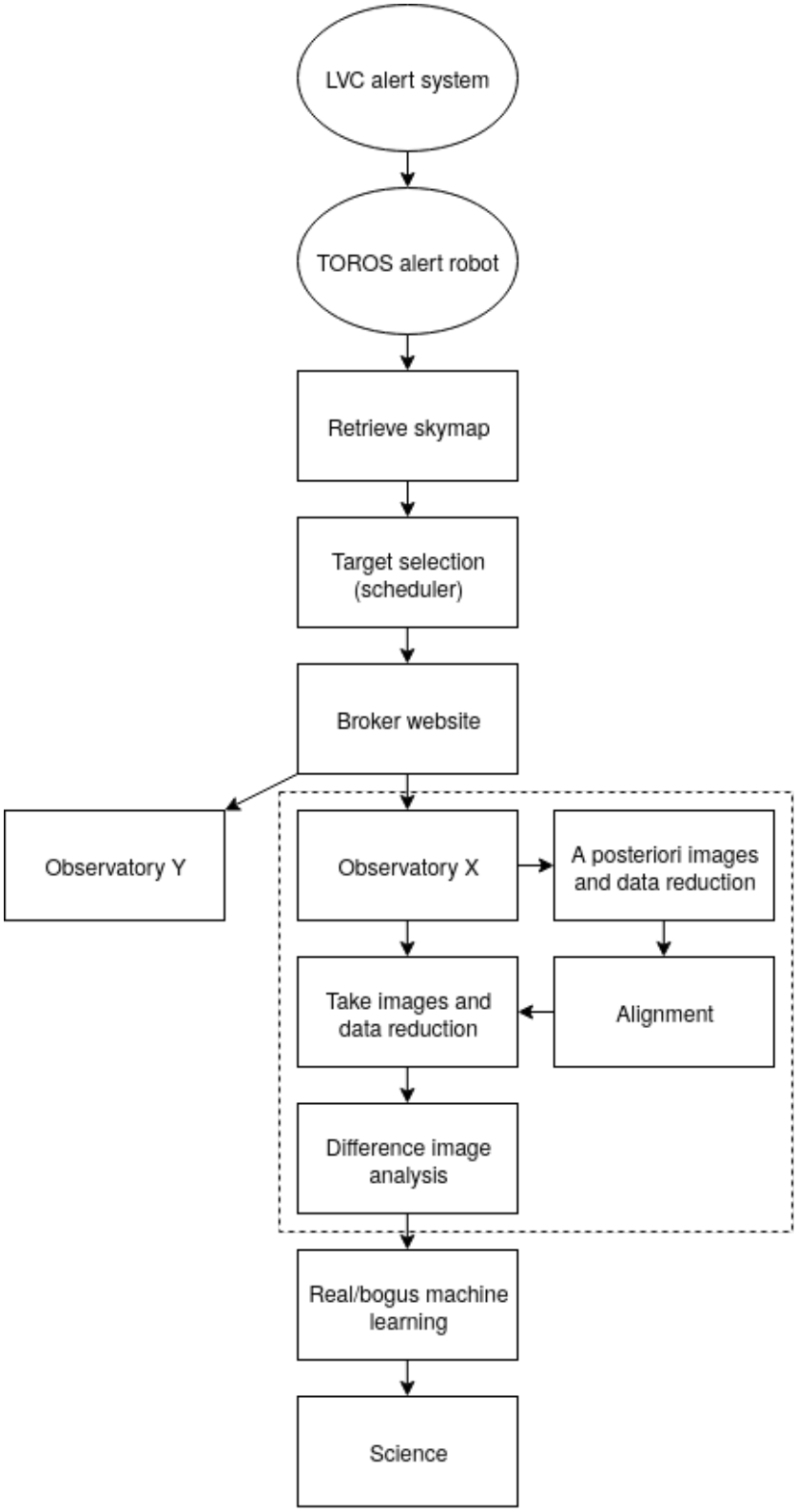

Figure 3.1: The TOROS alert pipeline. Adapted from Beroiz (2017). Credit: M. Beroiz.

square degrees [8].

Telescopes with < 1 square degree field-of-view (FOV) are not effective at completely tiling these large localization regions. For follow-up systems like CTMO, we adopt a target selection strategy — one appropriate for the combination of small FOV and large localization uncertainty [25]. The target selection strategy can improve the success rate of detecting a GW source transient [65]. Initially, the TOROS target selection employed the Gravitational Wave Galaxy Catalogue (GWGC), which contains 55,325 galaxies [127]. The current selection strategy uses the Galaxy List for the Advanced Detector Era (GLADE), which contains 3,262,883 entries [25] [46]. Target selection is based on three criteria, namely (1) localization uncertainty per pixel of LIGO skymap, (2) visibility of targets at moment of event based on geographical information, and (3) several cuts on parameters such as distance, magnitude, and luminosity [25].

My work coincides within the gray dashed line of Figure 3.1. Once the broker is uploaded with targets, the strategy becomes a rapid follow-up of assigned targets (per observatory within the network) followed by image reduction and analysis. If one wishes to find an optical transient within a reasonable search time, one should employ a prompt, systematic response, with a well-organized data flow, and possibly incorporating a variety of analysis strategies depending on the given situation [26]. The analysis strategies I have investigated and helped to implement at CTMO are collectively known as the CTMO Analysis Pipeline (CAL).

Observational data should be obtained and stored in an organized and procedural way. The directory tree for a standard nightly CTMO observation is shown in Figure 3.2. The tree assumes that there are multiple objects taken on a given night and possibly in different filters.

Once the raw data are stored from a given observing session, the next step is to reduce the raw data to calibrated data ready for scientific measurement. The procedure I have adapted is called the Static Image Series Reduction (SISR, pronounced “scissor”) pipeline and shown in Figures 3.3 and 3.4. The SISR pipeline assumes the tree structure implemented at CTMO. First, SISR grabs the dark and flat frames and creates a median-combined master dark (per integration time) and a normalized, dark-reduced flatfield (per filter). Then, the master darks and flatfields

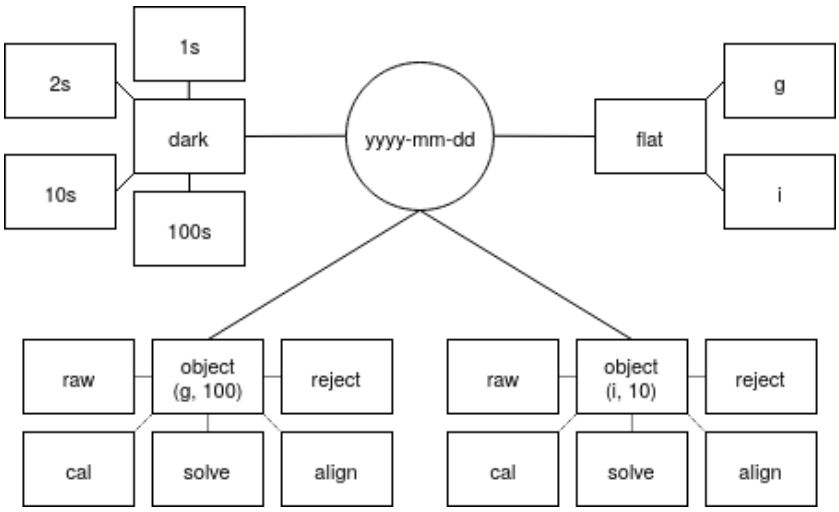

Figure 3.2: The directory structure implemented at CTMO.

are applied to the corresponding raw object series. Additional cleaning routines include transient artifact detection and background subtraction. Transient artifacts, such as cosmic rays, are localized sources of noise commonly found in astronomical images. CAL employs Astro-SCRAPPY [87], a Python-wrapped package encapsulating the L.A.Cosmic algorithm [120]), to remove transient artifacts. CAL employs two optional methods for background estimation and subtraction. One such method uses a sigma-clipped global median via the Astropy Photutils package [102]. Another method CAL uses for background subtraction is to estimate a spatially-varying mesh employed by the Source Extraction and Photometry (SEP) Python package, based on the original SExtractor algorithm [19] [27]. Once the raw objects are reduced, the next step involves plate solving the reduced frames using a local instance of Astrometry.net [73]. SISR aligns the solved frames using the Astropy Reproject [102] package or, if it fails, SISR calls on the Astroalign package to match via three-point asterisms and without having to rely on any WCS solution [26] [32] [64]. The final step of the reduction process is to stack the aligned frames and then to plate solve this final stack. The resulting stacks are ready for comparison to reference images and measurements like photometry.

When searching for an astrophysical transient near or within a galaxy, there are a number of analysis strategies one can follow to confirm a detection. One method is to compare the

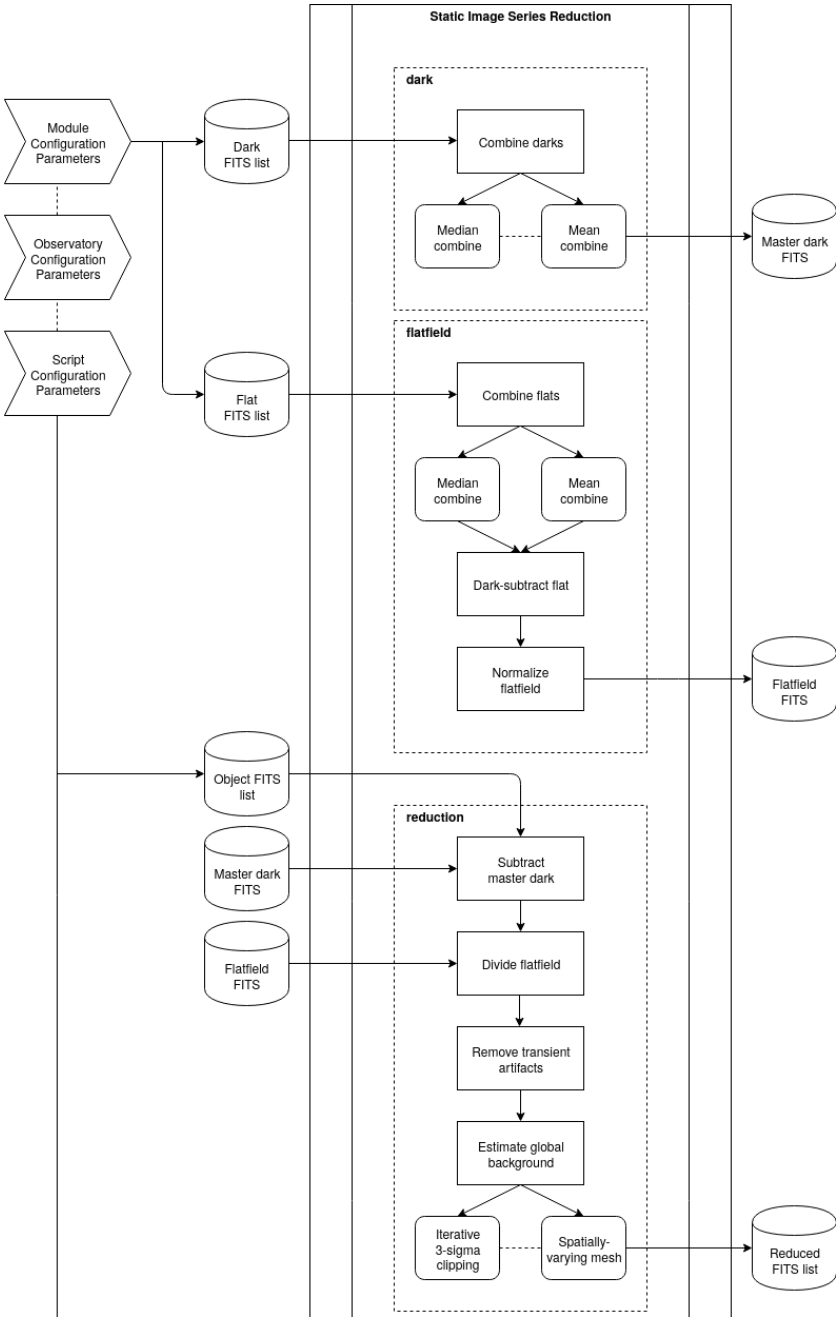

Figure 3.3: The Static Image Series Reduction (SISR) pipeline for CAL (part one).

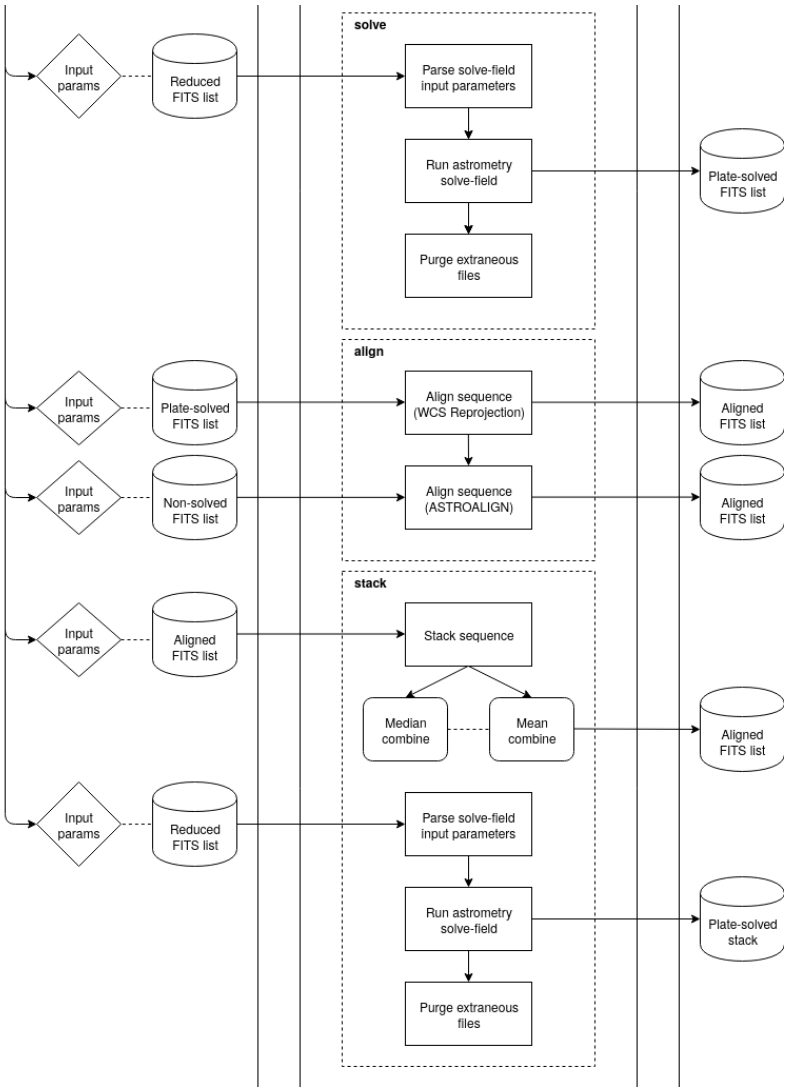

Figure 3.4: The Static Image Series Reduction (SISR) pipeline for CAL (part two).

number and positions of the sources detected in the image with those of a reference from archive. The process of detecting sources and comparing them with those detected in an archival image is called "cross-matching" catalogs, and is the first of three methods designed for the CTMO transient analysis pipeline. Another method commonly used for detecting transients is *difference image analysis (DIA)*, which involves aligning one's "target" image with a "reference" image taken from archive. Ideally, when it comes to DIA, the properties of the two compared images should be identical. The most ideal situation is to have target and reference images taken from the same optical system. However, many cases of difference imaging involve subtraction of a target image from a reference taken on a different system and during a separate epoch. In order to properly subtract two images from each other, not only do they need to be aligned with each other, but their point-spread functions should be matched. There are several methods in the literature for accomplishing this, including analytical solutions [14], numerical solutions [31], and even case studies involving machine learning solutions [104]. My work does not focus on the DIA-branch of the CAL, however this particular method is planned for future iterations of the pipeline. A variant of DIA is to model and subtract the host galaxy from the image entirely (before subtracting it from a galaxy-subtracted reference). Galaxy modeling can be accomplished using analytical models, like fitting Sérsic profiles, or numerically, like calculating an elliptical isophote model. The latter strategy, employing elliptical isophotes to generate a numerical model of the galaxy, is used in CAL. Ellipse-fitting requires several (i.e. hundreds) iterations to converge to an accurate model and introduces errors into photometry that are hard to quantify. The three strategies, in the order presented, are of increasing order of complication and shown in Figure 3.5.

3.2 CCD image theory

Astronomical imaging began involving electronic detectors in the late 1970s. The charge-coupled device (CCD) became the winner of contending electronic detectors by the end of the 1980s — having replaced all photographic plates except for large field imagers [128]. Early CCDs had 30-μm pixels in a 400×400 or 800×800 detector array [28].

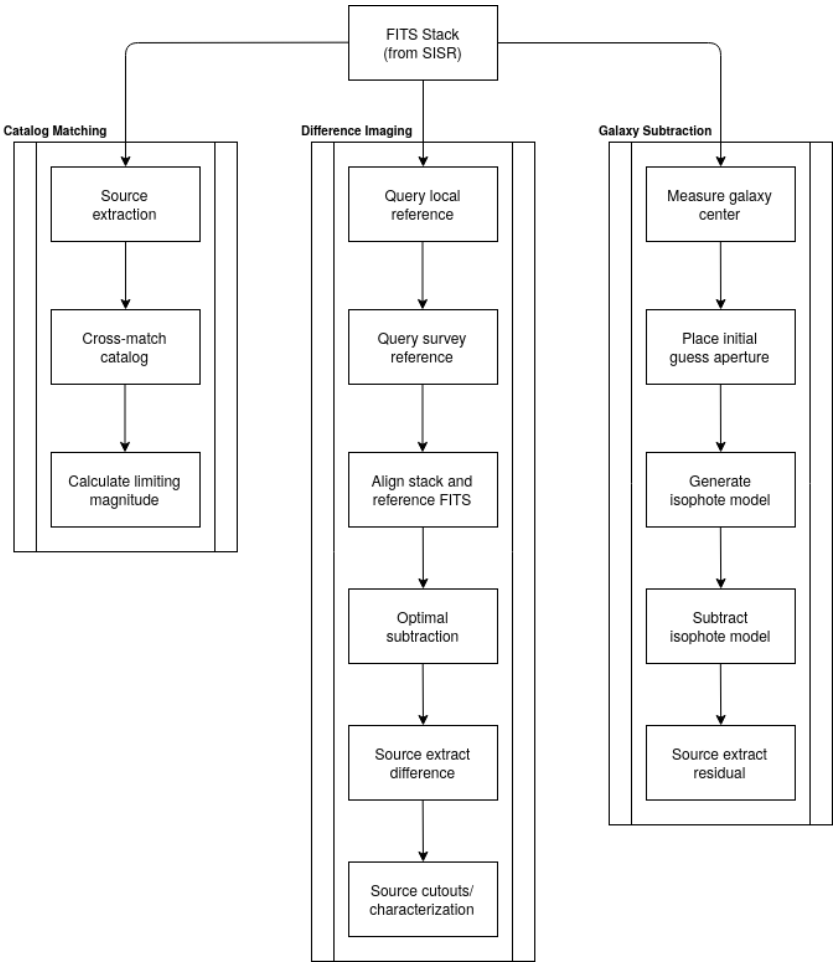

Figure 3.5: The analysis pipeline for CAL.

3.2.1 CCD imaging

A CCD chip is a silicon semiconductor. The chip is an array of etched silicon wells which act as individual photometers. A photon striking a silicon well is absorbed and converted into an electron via the photoelectric effect and stored within the well. For conversion to a digital image, the top row of the array is read out serially through a pre-amplifer, an amplifier, and an analog-to-digital converter. The remaining array is shifted up by a row and the process repeats until all rows are read out and reconstructed as a digital frame of pixels [28]. The pixel array is stored in the Flexible Image Transport System (FITS) file format, which includes the data array and a header data unit (HDU) containing image metadata [125].

By exposing the CCD array to the night sky, we can measure the signal from photons, which are converted and stored in pixel wells and which are used to determine the flux from a given source. There are several sources of noise, both systematic and random, intrinsic to CCD images. One source is from a constant voltage offset, or bias, which is applied across the entire array. One can produce a bias frame by reading the CCD chip with a "zero"-second exposure (i.e. the shortest possible exposure for the given CCD camera). All frames have this bias offset, which must be removed before making measurements.

After exposure of the chip, each well contains a certain number of thermally-oscillating electrons — hence a CCD must be cooled (typically by thermoelectric fans or liquid nitrogen) to reduce the thermal noise generated by electrons. Unless one is using a large-scale CCD camera with liquid-cooling, one must remove the thermal noise or "dark current" from the CCD frame through image reduction. Dark frames reflect the total thermal noise generated by electrons at a given integration time, chip temperature, and binning. For every object frame exposed per observation, one must create a series of dark frames with the same conditions as the object frames. The more dark frames, the better, and one should create a mean or median "master dark" per integration time, temperature, and binning. The master dark should be subtracted from the object frame.

No optical system is perfect. Artifacts including vignetting, dust particles, smudges, CCD structure, and uneven illumination introduce aberrations in object frames. These aberrations are

removed by exposing an evenly-illuminated canvas with the same filter, temperature, and binning of the object frames, which produces a "flat" frame. The canvas for creating the flats could be twilight flats or dome flats [84]. Typically, one should expose a flat to create a mean frame value of 30-50% saturation limit of the particular CCD being used. Similar to the creation of dark frames, a "master flat" should be produced by creating a mean or median of the sequence of individual flats, per filter, temperature, and binning. Finally, one should divide each resulting master flat by the mean frame value of the master flat itself, to produce a normalized "flatfield" (normalization preserves the photon-counting statistic). The dark-corrected object frame should be divided by the normalized flatfield.

3.2.2 CCD properties

We consider a mathematical formulation of the properties of a CCD, following the derivation given by Veilleux (2006) [122] by considering an array of M pixels consisting of N_{col} rows and N_{col} columns such that $M = N_{\text{row}} \times N_{\text{col}}$. We assume that each pixel on the array is exposed to a light source so that there are n electron charges accumulated on each pixel. The charges must be amplified before conversion into a digital number for computers to read, therefore the output signal of the CCD electronics S is not equal to the number of electrons accumulated per pixel n. However, $S \propto n$, and the factor that makes this statement an equation is called the "gain" and is denoted G. On a CCD chip, we are truly measuring electrons (converted from photons), which are subsequently multiplied in the CCD registry and expressed in terms of analog-to-digital units (ADUs). Consequently, one should properly define the "gain" G in terms of ADU/e^-. In that case, what most authors call the "gain" is really the *inverse gain*, since they express "gain" in terms of e^-/ADU. Hence, in this report, the inverse gain is denoted g and the true gain is denoted G, or

$$G\,[\text{ADU}/e^-] = \frac{1}{g\,[e^-/\text{ADU}]} \tag{3.1}$$

Additionally, we assume that a constant bias voltage is added across the frame and that

the exposure time is short enough so that the dark current is negligible. The mean bias level $\bar{B}$ [ADU] across the frame is

$$\bar{B} = \frac{1}{M} \sum_{i=1}^{N_{\text{row}}} \sum_{j=1}^{N_{\text{col}}} B_{ij} \tag{3.2}$$

where B_{ij} is the output signal of the bias at pixel (i, j) [ADU]. The overall output signal from the bias signal across the frame B is given by

$$B = \bar{B} + \sigma_B \tag{3.3}$$

where σ_B is the standard deviation of the readout noise [ADU] and which represents random fluctuations about the mean value of the bias from pixel-to-pixel. Given a cool and stable CCD chip, one can treat $\bar{B}$ and the probability distribution of σ_B both constant across the frame. Moreover, the mean value of the readout noise should vanish, or

$$\bar{\sigma_B} = \frac{1}{M} \sum_{i=1}^{N_{\text{row}}} \sum_{j=1}^{N_{\text{col}}} [\sigma_B]_{ij} = 0 \tag{3.4}$$

By including the gain and bias terms, the proportionality $S \propto n$ can be converted to an equality and expressed as

$$S = Gn + \bar{B} + \sigma_S \tag{3.5}$$

where σ_S is the standard deviation of the output signal of the CCD [ADU] and accounts for fluctuations in the mean value of the output signal. We need to remove the constant bias level $\bar{B}$ before taking measurements. Removing the bias involves subtracting the bias frame from the object frame,

$$S' = S - B \tag{3.6}$$

$$= Gn + \bar{B} + \sigma_S - \bar{B} - \sigma_B \tag{3.7}$$

$$= Gn + \sigma_S - \sigma_B \tag{3.8}$$

We consider that $S' = S'_{ij}$ and, therefore, $S' = \bar{S}'$. The average bias-subtracted signal is now

$$\bar{S}' = G\bar{n} + \bar{\sigma}_S - \bar{\sigma}_B \tag{3.9}$$

and, knowing that the fluctuations in the bias and total signal both average to zero, we are left with

$$\bar{S}' = G\bar{n} \tag{3.10}$$

We are now in a position to calculate the variance in the bias-subtracted signal. Starting with the definition of the variance in terms of the signal,

$$\sigma^2_{S'} = \overline{(S' - \bar{S}')^2} \tag{3.11}$$

$$= \overline{(Gn + \sigma_S - \sigma_B - G\bar{n})^2} \tag{3.12}$$

$$= \overline{[G(n - n') + \sigma_S - \sigma_B]^2} \tag{3.13}$$

Knowing that $\sigma_n = n - \bar{n}$, we can write

$$\sigma^2_{S'} = \overline{(G\sigma_n + \sigma_S - \sigma_B)^2} \tag{3.14}$$

We expand the square to eliminate cross-terms and simplify the expression,

$$(G\sigma_n + \sigma_S - \sigma_B)^2 = (G\sigma_n + \sigma_S - \sigma_B)(G\sigma_n + \sigma_S - \sigma_B) \tag{3.15}$$

$$= G^2\sigma_n^2 + G\sigma_n\sigma_S - G\sigma_n\sigma_B + G\sigma_n\sigma_S + \sigma_S^2 - \sigma_S\sigma_B - G\sigma_n\sigma_B - \sigma_S\sigma_B - \sigma_B^2 \tag{3.16}$$

$$= G^2\sigma_n^2 + 2G\sigma_n(\sigma_S - \sigma_B) + (\sigma_S - \sigma_B)^2 \tag{3.17}$$

$$\implies \sigma_{S'}^2 = G^2\overline{\sigma_n^2} + 2G\overline{\sigma_n(\sigma_S - \sigma_B)} + \overline{(\sigma_S - \sigma_B)^2} \tag{3.18}$$

$$= G^2\overline{\sigma_n^2} + 2G\overline{\sigma_n\sigma_S} - 2G\overline{\sigma_n\sigma_B} + \overline{\sigma_S^2} - 2\overline{\sigma_S\sigma_B} + \overline{\sigma_B^2} \tag{3.19}$$

The terms $\overline{\sigma_n\sigma_S}$, $\overline{\sigma_n\sigma_B}$, and $\overline{\sigma_S\sigma_B}$ are all treated as negligible, because σ_n, σ_S, and σ_B are uncorrelated and the total number of pixels M is large. The mean variance in S and B are equal, hence

$$\sigma_{S'}^2 = G^2\overline{\sigma_n^2} + 2\overline{\sigma_B^2} \tag{3.20}$$

From Equation 3.4 we can define the root mean square of the bias frame σ_B as

$$\sigma_B \equiv \sqrt{\overline{\sigma_B^2}} = \sqrt{\frac{1}{M}\sum_{ij}[\sigma_B]_{ij}^2} = \sqrt{\frac{1}{M}\sum_{ij}(B_{ij} - \overline{B})^2} \tag{3.21}$$

which means that $\overline{\sigma_B^2} = \sigma_B^2$ and

$$\sigma_{S'}^2 = G^2\overline{\sigma_n^2} + 2\sigma_B^2 \tag{3.22}$$

Photons striking the CCD detector will eject electrons with a mean value corresponding to the intensity of incident light. The individual electrons counted by the pixels will obey a Poisson distribution,

$$\sigma_n = \sqrt{N} = \sqrt{\overline{n}} = \overline{\sigma_n} \tag{3.23}$$

and, therefore, we can write

$$\sigma_{S'}^2 = G^2\overline{n} + 2\sigma_B^2 \tag{3.24}$$

Finally, using $\overline{S'} = G\overline{n}$, we can write

$$\boxed{\sigma_{S'}^2 = G\overline{S'} + 2\sigma_B^2} \tag{3.25}$$

which demonstrates that we need to measure $\overline{S'}$ and $\sigma_{S'}$ in order to determine the key CCD properties of gain G and readout noise σ_B. Equation 3.25 is a linear equation of the form $y = mx + b$ with a slope of G and a y-intercept of $2\sigma_B^2$. In the form of Equation 3.25, the independent variable is $\overline{S'}$ and the dependent variable is $\overline{\sigma_{S'}^2}$. By preference, we choose to swap the independent and dependent variables so that $x = \sigma_B^2$ [ADU^2] and $y = \overline{S'}$ (in ADU). The gain G [ADU/e$^-$] is calculated directly from the slope m as the inverse

$$m = \frac{1}{G} \tag{3.26}$$

and the y-intercept b gives us the readout noise σ_B as

$$\sigma_B = \sqrt{-\frac{bG}{2}} \text{ (in ADU)} \tag{3.27}$$

$$\sigma_B = \sqrt{-\frac{b}{2G}} \text{ (in e}^-\text{)} \tag{3.28}$$

The form, which is used in experimental testing of instruments, now reads

$$\boxed{\overline{S'} = \frac{1}{G}\sigma_{S'}^2 - \frac{2}{G}\sigma_B^2} \tag{3.29}$$

The readout noise limits detection at short integration times (i.e. when the number of electrons is of order σ_B^2 or less). Situations in which the readout noise becomes important include measurements with either spectrometers, narrowband filters, high time resolution, or high angular resolution [122].

One can sample the entire frame using this method, which gives reasonable measurements for the gain and readout noise. However, the best approach is to sample different regions across the chip, since flatfields are never perfect nor evenly-illuminated. Furthermore, a more realistic approach still would need to account for two additional complications, namely that (1) the sensitivity of pixels across the frame is not constant and that (2) pixels do not eject electrons at the same rate. These complications are addressed by Veilleux (2006) but not treated in this work [122].

3.3 Relative photometry

Relative photometry is the process by which one measures the signal from a star and places that signal on a calibrated measurement scale. The process involves measuring the total integrated signal from a source measured on a detector array and converting the total signal, or flux, to an instrumental magnitude. The same is done in parallel for a suitable comparison star (or multiple stars averaged together), suitable being defined as similar in color index and relatively localized in the sky. By comparing these multiple instrumental magnitudes with the corresponding reference magnitudes on a known photometric system, an offset can be applied to the instrumental magnitude to place that value on the same photometric scale.

Since the purpose of relative photometry is to measure stellar signals, we must understand the shape of their signal as detected by optical instrumentation. King (1971) was the first to piece together the profile of a stellar source, out to a radius of six degrees. He determined the profile can be organized into three components, namely (1) a central core, followed by (2) an exponential drop, and (3) an extended inverse-square "aureole" [72]. The central core is a nearly-uniform disk, surrounded by region of steeply-falling brightness. The size of the disk is determined by the resolving power of the telescope and is directly proportional to seeing and telescope aberrations. The center is well-represented by a Gaussian curve (although other formulae work as well over a small range). The steep drop that follows is not as steep as a Gaussian drop — an exponential drop represents the steep drop phase. The slope moderates abruptly to an inverse-square law followed over a factor of 1000 in angular distance from the center of the star. King showed that

integration of the inverse-square halo ("aureole") contains approximately 5% of the stellar signal [72].

Placing an optimal aperture on a stellar source becomes the next problem to solve before one can measure the flux accurately. There are several methods that have been adopted routinely, which include using some factor (e.g. 2-3) times the FWHM of the source or calculating particular characterizing radii (e.g. the "Kron radius"). These methods underestimate the stellar signal by a non-negligible amount. Howell (1990) demonstrated CCD growth curves as a means to measure the optimal aperture to place for conducting aperture photometry [66] . Once the optimal aperture has been measured, it can be placed on the center of the source at that optimal radius. Integration of a source using CCD growth curves ensures the capture of the entire stellar signal.

3.3.1 Measuring flux

We follow the methods described by Howell and Merline (1995) for understanding how one measures flux and flux error when performing aperture photometry [67] [91]. The total integrated photometric signal, which we call flux and denote as F, is given by

$$F = \sum_{i=1}^{N_A} (S_i^* + S_i^D + S_i^B + S_i^O) - N_A \bar{B} + N_A \bar{d} \tag{3.30}$$

where S_i^* is the total counts on pixel i due to the source [ADU], S_i^D is the total counts on pixel i due to dark current [ADU], S_i^B is the total counts on pixel i due to the background [ADU], S_i^O is the total counts on pixel i due to the DC bias offset [ADU], $\bar{B}$ is the mean background level [ADU], and $\bar{d}$ is the digitization offset [ADU]. Each pixel is summed in series over the entire area of the stellar aperture of N_A pixels.

If we define S_i to be the sum of all counts recorded on pixel i [ADU] given by

$$S_i = S_i^* + S_i^D + S_i^B + S_i^O \tag{3.31}$$

then the expression for the total integrated photometric signal F is simplified to

$$F = \sum_{i}^{N_A} S_i - N_A \bar{B} + N_A \bar{d} \tag{3.32}$$

We interpret the term $N_A \bar{d}$ as describing the net effect of conversion from electrons to ADU. The process of analog-to-digital conversion involves making a digital approximation of both the stellar and background pixel arrays. Given an idealized analog-to-digital converter, the average fractional ADU lost (gained) per pixel $\bar{f}^*$ in the stellar array is the same lost (gained) in the background array $\bar{f}^B$, such that

$$\bar{d} = \bar{f}^* - \bar{f}^B = 0 \tag{3.33}$$

Therefore, we can further simplify the expression for the total integrated photometric signal F to

$$\boxed{F = \sum_{i=1}^{N_A} S_i - N_A \bar{B}} \tag{3.34}$$

with the mean background $\bar{B}$ (in ADU) given by

$$\bar{B} = \frac{1}{N_B} \sum_{j=1}^{N_B} S_j = \frac{1}{N_B} \sum_{j=1}^{N_B} (S_j^D + S_j^B + S_j^O) \tag{3.35}$$

where S_j^D is the total counts on pixel j due to dark current [ADU], S_j^B is the total counts on pixel j due to the background [ADU], and S_j^O is the total counts on pixel j due to DC bias offset [ADU]. The mean (or median) is taken over N_B pixels. It is neither necessary, nor desirable, to have N_B and N_A to be the same number. The error in the photometry of a point-source depends on the number of background pixels used in the measurement.

3.3.2 Measuring flux error

There are five primary sources of noise associated with the signal measured on a CCD array. These sources are (1) photon statistics generated from the source, (2) photon statistics generated by the sky, (3) noise in the dark level, (4) readout noise, and (5) noise resulting from digiti-

zation of the analog signal. The expression for the one-sigma variance in the flux measurement is given by formal error propagation of the equation

$$F = \sum_{i=1}^{N_A} S_i - N_A \bar{B} + N_A \bar{d} \tag{3.36}$$

where, by ignoring pixel-to-pixel correlations and, hence, the covariance terms, we write the one-sigma variance as

$$\sigma_F^2 = \sum_{i=1}^{N_A} \left(\frac{\partial F}{\partial S_i} \right)^2 \sigma_{S_i}^2 + \left(\frac{\partial F}{\partial \bar{B}} \right)^2 \sigma_{\bar{B}}^2 + \left(\frac{\partial F}{\partial \bar{d}} \right)^2 \sigma_{\bar{d}}^2 \tag{3.37}$$

$$\boxed{\sigma_F^2 = \sum_{i=1}^{N_A} \sigma_{S_i}^2 + N_A^2 \sigma_{\bar{B}}^2 + N_A^2 \sigma_{\bar{d}}^2} \tag{3.38}$$

The first term is the variance in the total signal of each pixel, written explicitly as

$$\sigma_{S_i}^2 = \sigma_R^2 + g(S_i^* + S_i^D + S_i^B) \tag{3.39}$$

where g is the "inverse gain" [e^-/ADU] and σ_R is the read noise associated with one read from one pixel [e^-/pixel/read]. Given the previous simplification in notation for the total counts S_i that

$$S_i = S_i^* + S_i^D + S_i^B + S_i^O \tag{3.40}$$

we can write the first error term finally as

$$\boxed{\sigma_{S_i}^2 = \sigma_R^2 + g(S_i - S_i^O)} \tag{3.41}$$

Next, the variance in the mean background is given by

$$\sigma_{\bar{B}}^2 = \frac{1}{N_B^2} \sum_{j=1}^{N_B} (\sigma_R^2 + \sigma_{S_j^D}^2 + \sigma_{S_j^B}^2 + \sigma_{S_j^O}^2) \tag{3.42}$$

In general, we assume that we are dealing only with photon noise, so $\sigma_S^2 = gS$. We can further assume that the bias level is well-determined across the chip, so $\sigma_{S_j^O}^2 = 0$. Carrying that out leads to

$$\sigma_{\bar{B}}^2 = \frac{1}{N_B^2}\sum_{j=1}^{N_B}(\sigma_{S_j^D}^2 + \sigma_{S_j^B}^2 + \sigma_{S_j^O}^2 + \sigma_R^2) \tag{3.43}$$

$$\sigma_{\bar{B}}^2 = \frac{1}{N_B^2}\sum_{j=1}^{N_B}(gS_j^D + gS_j^B + \sigma_R^2) \tag{3.44}$$

$$\sigma_{\bar{B}}^2 = \frac{1}{N_B^2}\sum_{j=1}^{N_B}(gS_j - gS_j^O\sigma_R^2) \tag{3.45}$$

$$\sigma_{\bar{B}}^2 = \frac{1}{N_B^2}\sum_{j=1}^{N_B}\left[g(S_j - S_j^O)\right] + \frac{1}{N_B^2}\sum_{j=1}^{N_B}\sigma_R^2 \tag{3.46}$$

$$\boxed{\sigma_{\bar{B}}^2 = \frac{1}{N_B^2}\sum_{j=1}^{N_B}\left[g(S_j - S_j^O)\right] + \frac{\sigma_R^2}{N_B}} \tag{3.47}$$

Finally, we characterize the digitization noise. In general, the fractional count lost (gained) per pixel in the source integration is automatically compensated, because the average background per pixel is also over-estimated (under-estimated) by the same fractional count. This compensation is independent of the number of pixels in either the source or background arrays. Hence, in general, assuming the distribution functions for $\bar{f}^*$ and $\bar{f}^B$ are the same, then there should be no digitization offset so that

$$\bar{d} = \bar{f}^* - \bar{f}^B = 0 \pm \sigma_{\bar{d}} \tag{3.48}$$

The variance, or *digitization noise*, is the extent to which the above compensation is uncertain. The standard errors in the means $\bar{f}^*$ and $\bar{f}^B$ are given by

$$\sigma^2_{\bar{f}^*} = \frac{\sigma^2_f}{N_A} \tag{3.49}$$

and

$$\sigma^2_{\bar{f}^B} = \frac{\sigma^2_f}{N_B} \tag{3.50}$$

If we treat the standard errors in the means $\bar{f}^*$ and $\bar{f}^B$ as uncorrelated, then we can write the digitization noise in quadrature sum as

$$\sigma^2_{\bar{d}} = g^2(\sigma^2_{\bar{f}^*} + \sigma^2_{\bar{f}^B}) \tag{3.51}$$

$$\sigma^2_{\bar{d}} = g^2\left(\frac{\sigma^2_{\bar{f}}}{N_A} + \frac{\sigma^2_{\bar{f}}}{N_B}\right) \tag{3.52}$$

$$\boxed{\sigma^2_{\bar{d}} = \frac{g^2}{N_A}\left(1 + \frac{N_A}{N_B}\right)\sigma^2_f} \tag{3.53}$$

where σ_f is the uncertainty in estimating the true mean of the distribution of f from the fractional count in a single pixel. Newberry (1991) [98] showed that, for f uniformly distributed on $(-\frac{1}{2}, \frac{1}{2})$, the variance will be

$$\sigma^2_f = \int_{-\frac{1}{2}}^{\frac{1}{2}} (f - \bar{f})^2 df \tag{3.54}$$

which gives $\sigma_f = \sqrt{1/12}$ ADU $\simeq 0.289$ ADU. The digitization noise in most cases is small — the contribution from the digitization noise is typically only a few percent of the read noise. For the final expression for the one-sigma noise variance in the flux, we take the three variance terms and plug them into the expression as such

$$\sigma^2_F = \sum_{i=1}^{N_A} \sigma^2_{S_i} + N_A^2\sigma^2_{\bar{B}} + N_A^2\sigma^2_{\bar{d}} \tag{3.55}$$

$$\sigma_F^2 = \sum_{i=1}^{N_A}\left[\sigma_R^2 + g(S_i - S_i^O)\right] + N_A^2\left\{\frac{1}{N_B^2}\sum_{j=1}^{N_B}\left[g(S_j - S_j^O)\right] + \frac{\sigma_R^2}{N_B}\right\} + \frac{N_A^2}{N_A}\left(1 + \frac{N_A}{N_B}\right)g^2\sigma_f^2 \quad (3.56)$$

$$\sigma_F^2 = \sum_{i=1}^{N_A}\sigma_R^2 + \sum_{i=1}^{N_A}\left[g(S_i - S_i^O)\right] + \frac{N_A^2}{N_B^2}\sum_{j=1}^{N_B}\left[g(S_j - S_j^O)\right] + \frac{N_A^2}{N_B}\sigma_R^2 + N_A\left(1 + \frac{N_A}{N_B}\right)g^2\sigma_f^2 \quad (3.57)$$

$$\boxed{\sigma_F^2 = N_A\left(1 + \frac{N_A}{N_B}\right)\sigma_R^2 + \sum_{i=1}^{N_A}\left[g(S_i - S_i^O)\right] + \frac{N_A^2}{N_B^2}\sum_{j=1}^{N_B}\left[g(S_j - S_j^O)\right] + N_A\left(1 + \frac{N_A}{N_B}\right)g^2\sigma_f^2} \quad (3.58)$$

Equation 3.58 is the final expression for the photometric error in integration. The first term describes the effect of readout noise on both the star and background measurements. The second term describes the photon noise in the star measurement and the third term describes the photon noise in the background measurement. The fourth term describes the noise introduced by the digitization process. We can make approximations to Equation 3.58 by considering are previous assumptions about dealing only with photon noise and a well-determined bias. The source term can be approximated as

$$\sum_{i=1}^{N_A}\left[g(S_i - S_i^O)\right] = \sum_{i=1}^{N_A}\left[g(S_i^* + S_i^D + S_i^B)\right] \quad (3.59)$$

$$\sum_{i=1}^{N_A}\left[g(S_i - S_i^O)\right] = \sum_{i=1}^{N_A} gS_i^* + \sum_{i=1}^{N_A}(gS_i^D + gS_i^B) \quad (3.60)$$

$$\boxed{\sum_{i=1}^{N_A}\left[g(S_i - S_i^O)\right] \simeq S^* + N_A(\sigma_D^2 + \sigma_B^2)} \quad (3.61)$$

and the background term can be approximated as

$$\sum_{j=1}^{N_B}\left[g(S_j - S_j^O)\right] = \sum_{j=1}^{N_B}\left[g(S_j^* + S_j^D + S_j^B)\right] \tag{3.62}$$

$$\sum_{j=1}^{N_B}\left[g(S_j - S_j^O)\right] = \sum_{j=1}^{N_B} gS_j^* + \sum_{j=1}^{N_B}(gS_j^D + gS_J^B) \tag{3.63}$$

$$\boxed{\sum_{j=1}^{N_B}\left[g(S_j - S_j^O)\right] \simeq 0 + N_B(\sigma_D^2 + \sigma_B^2)} \tag{3.64}$$

If we plug Equations 3.61 and 3.64 back into Equation 3.58, we get more practical and still accurate approximation, written as

$$\sigma_F^2 \simeq N_A\left(1 + \frac{N_A}{N_B}\right)\sigma_R^2 + \left[S^* + N_A(\sigma_D^2 + \sigma_B^2)\right] + \frac{N_A^2}{N_B^2}\left[N_B(\sigma_D^2 + \sigma_B^2)\right] + N_A\left(1 + \frac{N_A}{N_B}\right)g^2\sigma_f^2 \tag{3.65}$$

$$\sigma_F^2 \simeq N_A\sigma_R^2 + \frac{N_A^2}{N_B}\sigma_R^2 + S^* + N_A\sigma_B^2 + N_A\sigma_D^2 + \frac{N_A^2}{N_B}\sigma_B^2 + N_A g^2\sigma_f^2 + \frac{N_A^2}{N_B}g^2\sigma_f^2 \tag{3.66}$$

$$\sigma_F^2 \simeq S^* + \left(N_A + \frac{N_A^2}{N_B}\right)\sigma_R^2 + \left(N_A + \frac{N_A^2}{N_B}\right)\sigma_B^2 + \left(N_A + \frac{N_A^2}{N_B}\right)\sigma_D^2 + \left(N_A + \frac{N_A^2}{N_B}\right) \tag{3.67}$$

$$\boxed{\sigma_F^2 \simeq S^* + N_A\left(1 + \frac{N_A}{N_B}\right)(\sigma_B^2 + \sigma_D^2 + \sigma_R^2 + g^2\sigma_f^2)} \tag{3.68}$$

For practical purposes, given modern detectors and cooling capabilities, we can neglect the readout noise, dark current, and digitization noise (i.e. $\sigma_R, \sigma_D, \sigma_f \longrightarrow 0$). Therefore, Equation 3.68 reduces to

$$\sigma_F^2 \simeq S^* + N_A\left(1 + \frac{N_A}{N_B}\right)\sigma_B^2 \tag{3.69}$$

Masci (2008) introduced two additional factors to consider: the situation of co-added frames and a small correction to the variance if one uses a median background estimation rather than the mean [85] [86]. The co-addition of frames is accounted for by dividing the Poisson source term in the error equation by the number of stacked frames. The correction term for using the median as the background estimation method is accounted for by considering the difference between estimating the mean and the median of a dataset. The median is noisier (i.e. less efficient to calculate) than the mean for a randomly-drawn sample. In other words, if $\bar{B}$ is taken as the median rather than the mean, then the variance in the background is underestimated by a factor of $\pi/2$. However, the median is robust against outliers, so transient artifacts will tend to skew the results less.

Lastly, we observe that the flux from the source alone S^* is a sum over pixels within the aperture of the difference between the total signal and the background signal. Note that S^* is in units of electrons (since the Poisson statistic comes from counting electrons, not ADU). Therefore, we must introduce an "inverse gain" term when expressing the signal as a measured flux in ADU. Taking into account the additional "inverse gain" factor, co-addition factor N, and statistic factor k, we get

$$\sigma_F^2 \simeq \frac{1}{gN}\sum_{i=1}^{N_A}(S_i - \bar{B}) + N_A\left(1 + k\frac{N_A}{N_B}\right)\sigma_B^2 \tag{3.70}$$

$$\boxed{\sigma_F^2 \simeq \frac{F}{gN} + N_A\left(1 + k\frac{N_A}{N_B}\right)\sigma_B^2} \tag{3.71}$$

If $\bar{B}$ is taken as the mean, then $k = 1$. If $\bar{B}$ is taken as the median, then $k = \pi/2$. Equation 3.71 is a simple yet effective expression for estimating the one-sigma variance of a flux measurement on a CCD array. The first term is the Poisson counting statistic from the source; the second term is the background variance, but this time taking into account the number of background pixels used in the estimation and the method of estimation (mean or median) [85] [86].

3.3.3 Instrumental and calibrated magnitudes

In order to report flux measurements, one must convert the flux to the magnitude scale and then calibrate that instrumental magnitude to place it onto a photometric system. Otherwise, astronomers would not understand how to compare measurements. The first step is to convert the flux to an instrumental magnitude, given by the fundamental relation of flux-to-magnitude, or

$$\boxed{m' = -2.5 \log F + ZP_e} \tag{3.72}$$

where F is the measured flux [ADU], ZP_e is the effective zeropoint, and m' is the instrumental magnitude. One must scale the instrumental magnitude to a normalized one-second exposure, which is achieved using

$$m' \text{ (scaled)} - m' \text{ (unscaled)} = -2.5 \log \left(\frac{t \text{ (scaled)}}{t \text{ (unscaled)}} \right) \tag{3.73}$$

By error propagation, the one-sigma variance in the magnitude is given by

$$\sigma_{m'}^2 = \left(\frac{\partial m_I}{\partial F} \right)^2 \sigma_F^2 \tag{3.74}$$

$$\boxed{\sigma_{m'}^2 = \left(-\frac{2.5}{\ln(10) F} \right)^2 \sigma_F^2} \tag{3.75}$$

Finally, we place the normalized instrumental magnitude onto a calibrated apparent magnitude scale. We make a plot of magnitude difference (instrumental magnitude less calibrated magnitude) on the y-axis versus the color of the photometric system to which we are comparing. Let us assume we are dealing with three SDSS filters, g, r, and i. We want to make plots for each passband, so we make plots of $g' - g$, $r' - r$, and $i' - i$ all versus $g - i$. By fitting a polynomial to the values on these plots, we can calculate the effective zeropoint ZP_e (per band) and calibrate the instrumental magnitude. The three second-order polynomials for each band are

$$g' - g = C_g + A_g(g-i) + B_g(g-i)^2 \tag{3.76}$$

$$r' - r = C_r + A_r(g-i) + B_r(g-i)^2 \tag{3.77}$$

$$i' - i = C_i + A_i(g-i) + B_i(g-i)^2 \tag{3.78}$$

where the A coefficients are first-order color terms, the B coefficients are second-order color terms, and the C offsets are the zeropoints for sources with color $g-i=0$. The A and B describe the photometric differences between the system that observed the instrumental magnitude and the system that observed the reported apparent magnitudes to which we are comparing. The effective zeropoint ZP_e is the entire RHS of the polynomial, and the calibrated apparent magnitude is the instrumental magnitude less ZP_e [82]. The errors in the calibrated magnitude for all three bands are determined from error propagation and given by

$$\sigma_g = \sqrt{\sigma_{g'}^2 + \sigma_g^2(-A_g - 2gB_g + 2iB_g)^2 + \sigma_i^2(-A_g + 2gB_g - 2iB_g)^2} \tag{3.79}$$

$$\sigma_r = \sqrt{\sigma_{r'}^2 + \sigma_g^2(-A_r - 2gB_r + 2iB_r)^2 + \sigma_i^2(-A_r + 2gB_r - 2iB_r)^2} \tag{3.80}$$

$$\sigma_i = \sqrt{\sigma_{i'}^2 + \sigma_g^2(-A_i - 2gB_i + 2iB_i)^2 + \sigma_i^2(-A_i + 2gB_i - 2iB_i)^2} \tag{3.81}$$

To compare unfiltered instrumental magnitudes to a photometric standard, we can use a similar polynomial-fitting technique as previously described [53]. If we consider a generic photometric system of blue b, red r, and "infrared" i passbands, and we observed unfiltered instrumental magnitudes u, then the polynomial would read

$$u - r = C + A(b-i) + B(b-i)^2 \tag{3.82}$$

with A and B as the first- and second-order color terms, respectively, and C is the zero-point for sources with a color of $b - i = 0$.

3.4 Angular diameter distance

Coalescing compact objects such as BNS and NSBH mergers are expected to be observed within or nearby galaxies out to modest cosmological distances. If the BNS or NSBH system is not dynamically kicked from the galaxy during its creation, its merger could occur physically within the galaxy. An observer wants to image galaxies and their surrounding field for an offset source, possibly within the galactic limb, with separation from the core. An angular observation of this separation translates to a physical separation if the distance to the source is known. We want to translate an angular diameter θ [arcsec] into a linear diameter D [pc] via known angular diameter distance to the source d_A [pc] via small-angle approximation

$$d_A = \frac{D}{\theta} \times 206265'' \tag{3.83}$$

We need to understand how cosmological distances affect the angular measurement of an object and to which distance the small-angle approximation is valid. I follow the treatment given by Carroll and Ostlie (2017) (hereafter, C&O) to understand how distance measurement is made in cosmology and to which limit the small angle approximation is valid [33]. The Friedmann-Robertson-Walker (FRW) metric describes a geometrically-flat, homogeneous, and isotropic spacetime, expressed as

$$ds^2 = (cdt)^2 - R^2(t)\left[\left(\frac{d\varpi}{\sqrt{1-k\varpi^2}}\right)^2 + (\varpi d\theta)^2 + (\varpi \sin\theta d\phi)^2\right] \tag{3.84}$$

where $k : \{-1, 0, 1\}$. The dimensionless, time-dependent *scale factor* $R(t)$ is related to the *coordinate distance* $r(t)$ by the *comoving coordinate* ϖ via

$$r(t) = R(t)\varpi \tag{3.85}$$

3.4.1 Proper distance

We define the *proper distance* as the distance measured between two events $\mathscr{A}$ and $\mathscr{B}$ in a reference frame for which they occur simultaneously ($t_{\mathscr{A}} = t_{\mathscr{B}}$) and is written as

$$\Delta\mathscr{L} = \sqrt{-(\Delta\mathscr{S})^2} \tag{3.86}$$

where $\Delta\mathscr{S}$ is the spacetime interval between events $\mathscr{A}$ and $\mathscr{B}$ with spactime coordinates ($t_{\mathscr{A}}$, $x_{\mathscr{A}}$, $y_{\mathscr{A}}$, $z_{\mathscr{A}}$) and ($t_{\mathscr{B}}$, $x_{\mathscr{B}}$, $y_{\mathscr{B}}$, $z_{\mathscr{B}}$), respectively, measured by an observer in the inertial reference frame $\mathscr{S}$. The interval $\Delta\mathscr{S}$ as measured along a straight worldline between events $\mathscr{A}$ and $\mathscr{B}$ in flat spacetime is

$$(\Delta\mathscr{S})^2 = (\Delta t)^2 - (\Delta x)^2 - (\Delta y)^2 - (\Delta z)^2 \tag{3.87}$$

We want to find the proper distance to an object as a function of time. Consider the differential proper distance $d\mathscr{L}$ at $dt = 0$ given by

$$d\mathscr{L} = \sqrt{-ds^2} \tag{3.88}$$

The comoving coordinate of the object is given by ϖ, with Earth at $\varpi = 0$, which means the object sits along a radial line extending from the Earth with $d\theta = d\phi = 0$. We insert these conditions into the FRW metric and integrate to find the proper distance $d_p(t)$ to an object at time t

$$d_p(t) = R(t)\int_0^{\varpi} \frac{d\varpi'}{\sqrt{1-k\varpi'^2}} \tag{3.89}$$

If we consider a flat universe ($k = 0$), then

$$d_p(t) = R(t) \int_0^{\varpi} d\varpi' = R(t)\varpi \tag{3.90}$$

Assuming that the object we measure has a constant ϖ (i.e. zero peculiar velocity), then the proper distance at any time can be obtained from

$$d_p(t) = R(t) d_{p,o} \tag{3.91}$$

and, with $R(t_o) = 1$,

$$d_{p,o} = \varpi \tag{3.92}$$

In a flat universe, the present proper distance to an object is just its coordinate distance $d_{c,o} = \varpi$ via $r(t) = R(t)\varpi$. If the object has a redshift of z, then its proper distance at time t_e is

$$d_p(t_e) = d_{p,o} R(t_e) = \frac{d_{p,o}}{1+z} \tag{3.93}$$

3.4.2 Comoving coordinate approximation

We want to express the comoving coordinate as a function of redshift, $\varpi(z)$. We begin with an equivalent expression of the proper distance. Consider a photon being emitted at and moving in from a particular comoving coordinate ϖ_e. At each time interval dt, the photon travels a distance of cdt. Getting the proper distance is more than just simply adding these infinitesimal chunks up because of the expansion of the universe. Dividing the distance cdt by the scale factor $R(t)$ converts this small distance to what it would be at the present time t_o. We can integrate the resulting quantity from ϖ_e at t_e to $\varpi = 0$ at t_o to find the proper distance. Finally, we multiply the result by $R(t)$ to convert the proper distance to the distance at some other time. We can write this equivalent statement for the proper distance as

$$d_p(t) = R(t) \int_{t_e}^{t_o} \frac{cdt'}{R(t')} \tag{3.94}$$

By writing $dt = dR/(dR/dt)$, we can write the present proper distance as

$$d_{p,o} = \int_{R(t_e)}^{R(t_o)} \frac{c dR'}{R'(dR'/dt)} \tag{3.95}$$

and, by defining $R(t_o) = 1$, $R(t_e) = 1/(1+z) \implies dR = -R^2 dz$, and

$$H(t) = \frac{1}{R(t)} \frac{dR(t)}{dt} \tag{3.96}$$

we can define a dimensionless integral $I(z)$, a function of redshift, such that

$$I(z) \equiv \int_0^z \frac{dz'}{H(z')} \tag{3.97}$$

We use a definition of the Hubble parameter $H(z)$ from C&O Eq. 29.122, which relates $H(z)$ to observed cosmological parameters,

$$H(z) = H_o \left[\Omega_{m,o}(1+z)^2 + \Omega_{\mathrm{rel},o}(1+z)^4 + \Omega_{\Lambda,o} + (1-\Omega_o)(1+z)^2 \right]^{1/2} \tag{3.98}$$

and allows us to write $I(z)$ completely in terms of redshift and observed cosmological parameters

$$I(z) \equiv \int_0^z \frac{dz'}{\sqrt{\Omega_{m,o}(1+z')^2 + \Omega_{\mathrm{rel},o}(1+z')^4 + \Omega_{\Lambda,o} + (1-\Omega_o)(1+z')^2}} \tag{3.99}$$

thus presenting the present proper distance dependent on the redshift

$$d_{p,o}(z) = \frac{c}{H_o} I(z) \tag{3.100}$$

For a flat universe (i.e. $k = 0$), we recall that $d_{p,o} = \varpi$, so the present proper distance is nothing more than the comoving coordinate, and we have the comoving coordinate now as a function of redshift (for a flat universe),

$$\varpi(z) = \frac{c}{H_o} I(z) \tag{3.101}$$

which must be evaluated numerically. From C&O, we define these numerical expressions as

$$S(z) \equiv I(z) \quad (\Omega_o = 1) \tag{3.102}$$

$$S(z) \equiv \frac{1}{\sqrt{\Omega_o - 1}} \sin\left[I(z)\sqrt{\Omega_o - 1}\right] \quad (\Omega_o > 1) \tag{3.103}$$

$$S(z) \equiv \frac{1}{\sqrt{1 - \Omega_o}} \sinh\left[I(z)\sqrt{1 - \Omega_o}\right] \quad (\Omega_o < 1) \tag{3.104}$$

so that, for all three cases of Ω_o, we have

$$\varpi(z) = \frac{c}{H_o} S(z) \tag{3.105}$$

Because $\sin(x) = x - \frac{x^3}{3!} + \frac{x^5}{5!} - \cdots$ and $\sinh(x) = x + \frac{x^3}{3!} + \frac{x^5}{5!} + \cdots$, $S(z) \simeq I(z)$ to second-order, and

$$\varpi(z) \simeq \frac{c}{H_o} I(z) \quad (z << 1) \tag{3.106}$$

We aim to find an approximate expression for the dimensionless integral $I(z)$. Following C&O, we ignore the brief radiation era $\Omega_{\mathrm{rel},o} = 0$ so that the current observed value $\Omega_o = \Omega_{m,o} + \Omega_{\Lambda,o}$. Furthermore, we use C&O Eq. 29.124 to relate the deceleration parameter q to the observed values for Ω,

$$q(t) = \frac{1}{2}\Omega_m(t) + \Omega_{\mathrm{rel}}(t) - \Omega_\Lambda(t) \tag{3.107}$$

$$q_o = \frac{1}{2}\Omega_{m,o} - \Omega_{\Lambda,o} \tag{3.108}$$

The integrand within $I(z)$ can be expressed as a Taylor expansion around $z = 0$, incorporating the previous relationships for Ω, to get

$$I(z) = \int_0^z \left\{ 1 - (1+q_o)z' + \left[\frac{1}{2} + 2q_o + \frac{3}{2}q_o^2 + \frac{1}{2}(1-\Omega_o) \right] z'^{\,2} + \cdots \right\} dz' \tag{3.109}$$

and integrating, we cast $I(z)$ into a form that is readily approximated,

$$I(z) = z - \frac{1}{2}(1+q_o)z^2 + \left[\frac{1}{6} + \frac{2}{3}q_o + \frac{1}{2}q_o^2 + \frac{1}{6}(1-\Omega_o) \right] z^3 + \cdots \tag{3.110}$$

The first two terms involve only the current value of the deceleration parameter q_o, so they depend only on the dynamics of the expanding universe. The terms of third-order and higher involve both q_o and k, so they depend on dynamics and geometry [33]. Therein lies the advantage of approximating to second-order: we can ignore assumptions about the curvature and merely incorporate observed knowledge of the dynamics of the expanding universe. In other words,

$$\varpi(z) \simeq \frac{cz}{H_o}\left[1 - \frac{1}{2}(1+q_o)z \right] \quad (\text{for } z << 1) \tag{3.111}$$

is valid regardless of the flatness of the universe or a nonzero cosmological constant. For a flat universe, this expression is an equivalent approximation to the current proper distance to a given source $d_{p,o}(z) = \varpi(z)$ for $k = 0$. The first term is the Hubble Law. The second term is a linear departure from the Hubble law due to an accelerated expansion of the universe.

3.4.3 Luminosity distance

We aim to relate the present proper distance approximation to the luminosity distance and the angular diameter distance. These two distances are observable, allowing an astronomer to make the measurements necessary to determine (to within the limits of the approximation) the

present proper distance to an object.

The luminosity distance d_L is given by

$$d_L \equiv \sqrt{\frac{L}{4\pi F}} \tag{3.112}$$

where L is the total luminous power emitted by the star and F is the radiant bolometric flux. We must first relate this expression to the comoving coordinate ϖ and account for cosmological effects which further reduce the radiant flux observed. Consider a source of light located at the origin ($\varpi = 0$) of a comoving coordinate system. Photons from this source reach a spherical surface at $\varpi =$ constant > 0. From the FRW metric, the surface area of the sphere at the present time is $4\pi\varpi^2$. The radiant flux diminishes as $1/\varpi^2$ after traveling from the source to the spherical surface. Two additional cosmological factors reduce the radiant flux. One factor is *cosmological redshift*, which causes the energy of each photon $E = hc/\lambda$ to be reduced by a factor of $1+z$. Another factor is *cosmological time dilation*, which affects the average time interval between photons being emitted from the source. Consequently, the rate at which photons arrive at the sphere is less than the rate of emission by another factor of $1+z$. These effects add up to the expression of radiant flux at the sphere's surface,

$$F = \frac{L}{4\pi\varpi^2(1+z)^2} \tag{3.113}$$

By substituting Equation 3.113 into Equation 3.112, we get

$$d_L = \varpi(1+z) \tag{3.114}$$

where ϖ is evaluated numerically via Equations 99 and 101. The luminosity distance is given exactly by

$$d_L(z) = \frac{c}{H_o}(1+z)S(z) \tag{3.115}$$

and approximately by

$$\boxed{d_L(z) \simeq \frac{cz}{H_o}\left[1+\frac{1}{2}(1-q_o)z\right] \quad (z << 1)} \tag{3.116}$$

The angular diameter distance d_A is given by

$$d_A \equiv \frac{D}{\theta} \tag{3.117}$$

where D is the linear diameter and θ is the angular diameter. We can relate the linear diameter of an object (e.g. a galaxy) to its redshift by integrating the FRW metric across the galaxy in the plane of the sky with $dt = d\varpi = d\phi = 0$,

$$D = R(t_e)\varpi\theta = \frac{\varpi\theta}{1+z} \tag{3.118}$$

or, for the angular diameter distance,

$$d_A = \frac{\varpi}{1+z} \tag{3.119}$$

where ϖ can be calculated numerically or approximately as previously described. From $d_L = \varpi(1+z)$, we get the relationship between the angular diameter distance and luminosity distance,

$$\boxed{d_A = \frac{d_L}{(1+z)^2}} \tag{3.120}$$

Now we know the path that we must take when making measurements of a detected transient source offset from the center of its host. We will need to make a calculation of the galaxy's luminosity distance via measurements of its redshift, then relate that to the angular diameter distance. Once we have a calculated angular diameter distance, we can make a measurement of the angular diameter using image data, and thus calculate the linear diameter of the offset between the source and host.

CHAPTER IV

OBSERVATORIES

4.1 The Transient Robotic Observatory of the South

The Transient Robotic Observatory of the South (TOROS) is a network of astronomical observatories in the western hemisphere dedicated to following up LIGO alerts in the search for optical counterparts to GWs [22] [51]. TOROS formed in 2011 among institutions in North America, South America, and Europe. The primary goal is to produce high quality, resolution, and depth images to cover localization regions of gravitational wave events on the sky. On 6 June 2013 the LVC issued a worldwide call for multi-messenger observers to participate in EM follow-ups of GW events recorded by their detectors. TOROS signed a memorandum of understanding with the LVC April 2014. TOROS participated in the LVC first observing run (O1) from September 2015 to January 2016 [52] and the second observing run (O2) from November 2016 to August 2017 [18].

TOROS has deployed a wide-field optical reflector on the Cordon Macón mountain site of the Atacama Plateau in Salta province in Argentina. The site is at latitude 24:37:21.9 S and longitude 67:19:41.6 W and has an elevation of 4637 meters (15213 feet). The site has been measured as one of the best in the world for optical photometry and spectroscopy and was considered by ESO as a candidate site for its Extremely Large Telescope [101] [116].

The primary instrument is a PlaneWave 0.6-meter reflector with a four-element prime focus corrector (200 mm CaFl lens) giving it a FOV of 9.85 square degrees. The instrument is equipped with a STA 1600 LN 10560×10560-pixel camera with 9-μm pixels, providing an imaging area of 95.04×95.04 mm and a pixel scale of 1”/pixel. The optical system will have a bandwidth from 0.4 to 0.9 μm, covering the primary SDSS *griz* passbands [51] [49].

Figure 4.1: The location of the TOROS site at Cordon Macón is indicated by the red marker. The left line corresponds to the distance between Córdoba and Salta ($\sim$ 700 km). The right line corresponds to the distance between Buenos Aires and Salta ($\sim$ 1200 km). The city of Salta is $\sim$ 400 km from Cordon Macón. Credit: M. C. Díaz.

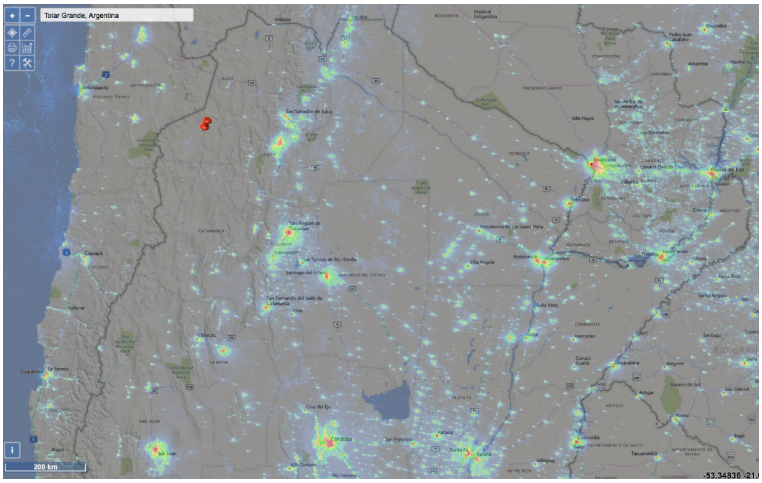

Figure 4.2: Light pollution at Cordon Macón. Credit: M. C. Díaz.

These specifications were chosen to satisfy the following problems: the relatively poor localization of gravitational waves when only one or two detectors are working optimally; the large uncertainty in the expected luminosity, duration, and rate of optical counterparts to BNS or NSBH mergers. The aim of the observatory is to be a fully robotic facility with a priority-based scheduler that runs constantly on four actions: GW trigger follow-ups; GRB follow-ups; baseline imaging of the entire surveyable area; searching for short-duration transients, variable sources, and moving objects [51].

The TOROS collaboration has access to several facilities, including the 1.54-meter telescope at Estacion Astrofisica Bosque Alegre (EABA), the 0.83-meter T80-South (T80S) telescope at the Cerro Tololo Inter-American Observatory (CTIO), the 0.43-meter telescope at the Dr. Cristina V. Torres Memorial Astronomical Observatory (CTMO), and the 2.1-meter telescope at Guillermo Haro Observatory (OAGH). TOROS typically has access to $\sim$ 5 hours of TOO time on the Gran Telescopio Canaria (GTC) segmented 10.4-meter telescope via the Mexican Time Allocation Committee.

4.2 CTMO

The Dr. Cristina Valeria Torres Memorial Astronomical Observatory (CTMO) is the astronomical observatory of the University of Texas Rio Grande Valley and the only observatory in South Texas dedicated to scientific and educational activities. The primary scientific objectives of CTMO relate to the field of time domain astronomy. The observatory follows up LIGO GW alerts to search for optical transients. Additionally, numerous student projects, ranging from exoplanet transit time series and variable star observations to asteroid tracking and rotation analysis, have been accomplished at CTMO.

4.2.1 History

The observatory was originally designated the Nompuewenu Observatory. “Nompuewenu” means “beyond the sky”, a word from the Mapuche people, who are indigenous to Argentina. Originally, the observatory was built near the Brownsville campus of UTRGV, behind the current

Recreation Center on University Boulevard. Light pollution from downtown Brownsville and the university forced the decision to relocate the observatory to a new location. UTRGV alum Antonio Galan found the new site — an area in Resaca de la Palma State Park, located near the main park building, which is where the observatory stands to this day [34]. The current foundation in Resaca de la Palma was completed in July 2016. First light was achieved in September 2016. Following this, Nompuewenu Observatory operated in scientific capacity from then until May 2018. The observatory was officially inaugurated as the Dr. Cristina Valeria Torres Memorial Astronomical Observatory (CTMO) on 5 May 2018. CTMO operated for nearly one year until April 2019, when it paused observations for replacement of the Meade 16" reflector with a PlaneWave 17" astrograph. In June 2019, the new optical system with a preliminary phase of CCD optics received first light. Observations with this preliminary phase configuration ran until October 2019, at which point the CCD system was swapped for a "next-generation" CCD and filter system.

4.2.2 Current specifications

CTMO is located in Resaca de la Palma State Park in Brownsville, Texas. The site is at latitude 25:59:44.8 N and longitude 97:34:08.2 W and has an elevation of 12 meters (39.4 feet). At the time of writing (January 2020), CTMO houses a PlaneWave Instruments 17" Corrected-Dall-Kirkham astrograph as its primary observing instrument. The astrograph optical tube assembly (OTA) is composed of a dual carbon-fiber truss upper cage: the upper cage houses the primary mirror and electronic focus assembly (EFA) and the lower cage houses the secondary mirror and is covered with a light shroud. The carbon-fiber truss design has an advantage over standard optical tube assemblies in that it minimizes focus shifts caused by thermal expansion of the tube assembly. Thermal equilibrium of the OTA is further achieved with three cooling fans acting as exhaust ports on the back of the OTA and four fans blowing across the surface of the primary mirror. These fans are controlled by the EFA.

The OTA is mounted on an L-500 altitude-azimuth direct drive mount and an equatorial wedge. The L-500 has a payload capacity of 90 kilograms. The direct drive mount offers several advantages: no backlash or periodic error and incorporation of high-precision axis encoders. The

Optical design	Corrected Dall-Kirkham astrograph
Aperture	432 mm
Focal length	2939 mm
Focal ratio	f/6.8
Central obstruction	23.7% by surface area
	48.6% of primary mirror diameter
Back focus from mounting surface	260 mm
Back focus from racked in focuser	184 mm
OTA weight	48 kg
OTA length	1067 mm
Optical performance	6.5 μm RMS at 21 mm off-axis
	9.6 μm RMS at 26 mm off-axis
Optimal FOV	70 mm image circle

Table 4.1: Optical system for PlaneWave Instruments CDK17 astrograph.

Optical diameter	432 mm
Outer diameter	445 mm
Shape	Prolate ellipsoid
Material	Precision annealed borosilicate
Coating	Enhanced aluminum - 96%

Table 4.2: Primary mirror specifications for PlaneWave Instruments CDK17 astrograph.

Diameter	190 mm
Shape	Spherical
Material	Precision annealed pyrex
Coating	Enhanced aluminum - 96%

Table 4.3: Secondary mirror specifications for PlaneWave Instruments CDK17 astrograph.

mount will counter nudges and wind gusts with feedback from the servomotors. The mount can achieve a slew rate up to 50 degrees per second, which means it can track high proper motion targets and reduces time to acquire targets. The EFA kits controls a Hedrick focuser with an imaging payload of nine kilograms and micron-scale position resolution. Attached to the focuser is a Finger Lakes Instrumentation ProLine 16803 CCD camera and CFW-5-7 filter wheel with SDSS Generation 2 *ugriz* and Johnson-Cousins *V* passband filters. Specifications for the OTA, primary mirror, and secondary mirror are presented in Tables 4.1, 4.2, and 4.3, respectively.

4.2.3 New optical system

A group for advancing instrumentation and automation was formed by members of the Time Domain Astronomy Group (TDAG) with the goal of completely automating CTMO. The author's work with the instrumentation group has focused primarily on the telescope and imaging systems employed at CTMO. When I began work with the TDAG in November 2016, the observatory housed a 16" reflecting telescope and a modest, unfiltered CCD imaging system. The final configuration of a fully-automated system would need to satisfy several criteria. The telescope and imaging system would need to have a larger field-of-view (FOV) than the initial FOV ($\sim 15.19' \times 11.44'$) to make pointing and searching for candidate sources easier. Additionally, the system would have to be capable of photometric multi-band imaging. While unfiltered exposures maximize the SNR for a given source, it is impossible to conduct relative photometry on a source of unknown physical nature without a series of passbands. The telescope and mount would need several improvements, including but not limited to pointing accuracy, tracking stabilization, reduction in startup time, and improving the capabilities of the focuser. The author envisions two "generations" of CTMO optics.

The initial operational phase of CTMO began in late 2016 with a Meade LX200 GPS 16" Schmidt-Cassegrain reflector as the primary instrument. The reflector was paired with an unfiltered SBIG STF-8300M CCD camera (see Table D.1 for specifications). In January 2017, we introduced an SBIG FW8-8300 filter wheel with Baader R, G, B, and luminance broadband filters; Baader Hα, SII, and OIII narrowband filters. The filter wheel accepts drop-in 36-mm round

filters and weighs 1.35 lbs.

Proceeding into Generation 2 involved introducing an entirely new telescope and CCD imaging system to the observatory. Motivation for a new telescope came from interest in a more effective ability to respond to transient events. Telescope pointing and tracking performance in the LX200 was a serious scientific impediment for conducting rapid and precise follow-ups to astrophysical transient events. The telescope chosen for ushering in Generation 2 CTMO is the PlaneWave Instruments Corrected Dall-Kirkham 17" astrograph. Work began in April 2019 with the removal of the Meade 16" reflector and the installation of a new pier. Following the installation of the new pier was the installation of an equatorial wedge, PlaneWave Instruments L-500 direct drive mount, and the 17" astrograph OTA. The Hedrick focuser and the EFA were mounted to the OTA. "Preliminary phase" optics involved an unfiltered Apogee Alta F16M CCD camera. Once the entire telescopic assembly was configured, PlaneWave engineers remotely tuned the mount to our weight distribution. We then balanced the right ascension and declination drives of the mount, completed a rough and fine focus, constructed a 20-source pointing model, and adjusted the equatorial wedge. First light of this system took place in June 2019. "Mature phase" optics saw the replacement of the Apogee camera with a Finger Lakes Instrumentation ProLine 16803 CCD camera and CFW-5-7 filter wheel with Sloan 2nd-generation *ugriz* and Johnson *V* passband filters. First light of this final system took place in October 2019.

Measurements for all three optical configurations of CTMO, including *in situ* measurements of gain, readout noise, and linearity, are presented in Appendix D.

CHAPTER V

RESULTS

I was once told by an astronomer in Flagstaff that, in observational astronomy, there are two fundamental laws that should never be broken, which are (1) Never touch the primary mirror and (2) Always copy your data. From personal experience, I add (3) Always bring snacks to share during observing sessions.

In Chapter 3, I described the tools needed for an optical observatory with a small FOV ($<$ 1 square degree) to follow-up GWs and search for optical counterparts. In this chapter, I describe the results following the TOROS network response to three GW event in O2 and O3. In 4.1, I present the follow-up data of GW170104 and GW170817. In 4.2, I present the follow-up data of S190814bv. Following the observational results, I describe the measurements of the only detected transient during this search, AT2017gfo. In 4.3, I describe the results of relative photometry on AT2017gfo and its light curve in three optical passbands. In 4.4, I measure the angular distance between AT2017gfo and the center of its host, NGC 4993, in order to calculate the physical distance of AT2017gfo from the galactic core.

5.1 LIGO O2 follow-up observations

During the LIGO O2 Science Run, the TOROS network responded to two GW candidate alerts. LIGO and Virgo detected the event trigger G268556 on 2017-01-04 at 10:11:49 UTC, which was subsequently classified as a BBH merger and promoted to the event GW170104 [5] [78]. LIGO and Virgo detected the event trigger G298048 on 2017-08-17 at 12:41:06 UTC, which was classified as a BNS merger and promoted to the event GW170817 [6] [79].

5.1.1 Observations of GW170104 targets

TOROS responded to the alert and observed galaxy targets assigned by the TOROS broker on the nights of 13-15 January 2017 using the EABA 1.54-m telescope and an unfiltered Apogee U19 camera at 1×1 binning. See Table 5.1 for a list of observed targets and Figure 5.1 for the GW localization probability. The localization probability was obtained from the TOROS broker system, which parsed and distributed information originally sent by the LSC. We observed reference fields on the nights of 16, 18, and 19 November 2017 using the 1.54-m telescope and an unfiltered Apogee F16M camera at 2×2 binning.

Name	RA	Dec	Distance [Mpc]	Localization Probability
ESO 202-009	04:21:03.62	-48:18:14	62.13	1.008e-06
ESO 242-018	00:37:06.17	-46:38:38	49.22	4.854e-07
ESO 364-014	05:55:01.29	-36:56:49	73.65	9.760e-07
ESO 425-010	06:08:57.45	-27:48:06	57.06	9.738e-07
ESO 487-003	05:21:50.70	-23:57:04	56.60	1.017e-06
ESO 555-005	05:51:39.84	-18:01:21	42.15	1.002e-06
ESO 555-022	06:01:07.98	-21:44:19	27.88	7.158e-07
IC 2143	05:46:52.61	-18:43:34	45.77	1.002e-06
NGC 1341	03:27:58.43	-37:08:59	30.62	8.526e-07
NGC 1567	04:21:08.73	-48:15:17	67.19	1.008e-06
NGC 1808	05:07:42.34	-37:30:46	16.89	9.562e-07
PGC 073926	01:20:36.55	-36:05:34	243.16	3.426e-07
PGC 147285	05:16:47.96	-36:04:07	150.98	8.591e-07
PGC 3080859	05:19:35.87	-36:49:02	87.86	8.723e-07

Table 5.1: TOROS broker targets observed by EABA for GW170104.

I inspected the calibration and raw object frames by eye and rejected bad exposures or low SNR caused by clouds. With each object came a set of bias, dark, and flat frames at various integration times. I scaled the darks using the bias frames — since CAL assumes that an observer has taken sets of dark frames per exposure on a given night, I chose to conduct the steps of dark-scaling, image combination, and flatfield normalization using the Image Reduction and Analysis Facility (IRAF) [115]. I employed CAL to handle the remaining reduction steps of dark subtraction, flatfielding, background subtraction, plate solving, and alignment. I applied a masked array at a strict 2σ threshold and minimum number of five connected pixels. The dilation size

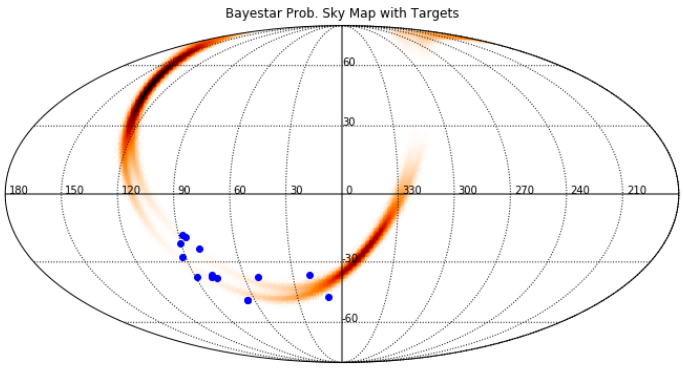

Figure 5.1: Localization skymap for GW170104 with TOROS broker assigned targets highlighted in blue. Figure from Díaz et al (2017).

of the masked sources was a 31×31-pixel box. I passed the mask to the Source Extraction and Photometry (SEP) package [19], which calculated and subtracted a spatially-varying mesh of 64×64-pixel boxes, evaluated at the median, from the reduced frames. I did not make a search for transient artifacts (such as cosmic rays) since the process could potentially remove interesting, faint transients that warrant further inspection. Furthermore, by median-stacking a sequence of frames, single-frame transient artifacts are effectively removed. I plate solved the reduced frames using a local instance of Astrometry.net [73] and aligned the solved frames using the Astropy `Reproject` package [102]. I median-combined the aligned frames into master stacks using the IRAF `imcombine` method for memory considerations. The stacking revealed linear and residual effects on several of the CCD frames, likely associated with poor observing conditions and that scaled darks were used. These effects impact the signal from several stars and, in some cases, even the target galaxies themselves.

I calculated the air mass using the interpolative formula developed by Kasten and Young (1989) [71] at an altitude corresponding to the middle time of the observing sequence. I measured the seeing by using the aperture profile functionality of AstroImageJ [39] and the average of 10 test stars near the center of the field. I used the SAOImage DS9 [70] regions tool to calculate the aperture growth curves for source extraction. The EABA target curves gave 25-px optimal radii; the reference curves gave 15-px optimal radii. The CCD growth curves for test stars in the target and reference frames are provided in Appendix C.

I used a local instance of SExtractor [27] to perform source extraction and set the detection threshold at 4σ to extract catalogs of the instrumental magnitudes of all sources. I used the SAOImage DS9 catalog tool to cross-match these source-extracted catalogs with the GSC 2.3 catalog [74] overlapping the FOV and convert the unfiltered magnitudes to the POSS-II red F-band. I plotted the magnitude difference between the unfiltered instrumental magnitudes and the apparent F magnitude versus POSS-II color ($j - N$) and fitted a weighted, second-order polynomial to the points to calculate color terms and the zeropoint. From these terms, I calculated the effective zeropoint in the POSS-II F-band and determined the limiting F magnitude (depth). Observational parameters for the target and reference frames are reported in Table 5.2 and Table 5.3, respectively. Example stacks for the EABA targets and references are presented in Appendix A.

Date	Object	Stack	Alt [deg]	Seeing ["]	Air mass	Sample	Depth
01-13	ESO 364-014	6×60	53.7	2.6	1.24	115/118	23.43 ± 0.06
	ESO 364-014	87×30	47.7	2.9	1.35	157/160	19.9 ± 0.2
	ESO 487-003	6×60	48.3	3.0	1.34	81/84	17.88 ± 0.07
	NGC 1341	51×60	46.2	2.7	1.38	89/122	18.15 ± 0.07
	NGC 1808	67×60	60.3	2.8	1.15	142/181	19.16 ± 0.07
	PGC 073926	41×60	47.5	2.9	1.36	69/69	17.3 ± 0.1
01-14	ESO 202-009	5×30	72.6	2.6	1.05	56/62	17.18 ± 0.08
	ESO 202-009	9×40	72.3	2.7	1.05	71/73	18.71 ± 0.07
	ESO 202-009	17×35	71.4	2.7	1.05	76/78	19.9 ± 0.2
	ESO 202-009	29×60	69.2	2.4	1.07	105/110	19.1 ± 0.1
	NGC 1341	5×60	77.2	2.2	1.03	61/63	18.9 ± 0.1
	PGC 147285	22×60	56.2	2.9	1.20	99/101	18.15 ± 0.07
01-15	ESO 242-018	50×60	46.1	2.5	1.39	89/90	15.69 ± 0.07
	ESO 425-010	44×60	38.7	3.5	1.60	260/270	20.4 ± 0.1
	ESO 555-005	29×90	53.5	2.6	1.24	303/333	17.62 ± 0.03
	ESO 555-022	16×150	46.8	3.0	1.37	319/335	19.85 ± 0.05
	IC 2143	45×60	64.0	2.4	1.11	288/296	22.26 ± 0.08
	NGC 1567	8×180	70.9	2.8	1.06	126/137	20.64 ± 0.05
	NGC 1567	13×120	68.2	2.5	1.08	129/145	20.02 ± 0.06
	PGC 3080859	46×60	74.9	2.5	1.04	198/204	19.00 ± 0.05

Table 5.2: EABA target stacks for GW170104. *Stack* is defined as the number of frames per stack times their integration time. *Sample* is defined as sources cross-matched per total sources detected.

Following our reduction method and 4-σ source search, we did not detect any optical tran-

Date	Name	Stack	Alt [deg]	Seeing [”]	Air mass	Sample	Depth
11-16	ESO 202-009	40×40	73.2	2.9	1.04	285/292	18.80 ± 0.07
	ESO 364-014	21×30	84.0	2.6	1.01	473/478	19.18 ± 0.09
	ESO 555-022	20×30	73.0	2.9	1.05	642/649	19.86 ± 0.09
	NGC 1341	20×30	81.0	3.1	1.01	175/213	18.20 ± 0.09
	NGC 1567	40×30	71.2	3.0	1.06	256/259	19.04 ± 0.08
	PGC 073926	20×30	85.4	4.0	1.00	132/133	17.1 ± 0.1
	PGC 147285	20×30	84.5	2.9	1.00	318/321	20.1 ± 0.2
11-18	ESO 202-009	10×60	64.3	3.3	1.11	213/215	18.75 ± 0.07
	ESO 202-009	20×30	62.7	4.0	1.13	162/163	18.96 ± 0.09
	ESO 242-018	20×30	71.3	4.2	1.06	127/127	15.48 ± 0.07
	ESO 364-014	21×30	70.5	2.9	1.06	456/467	19.17 ± 0.09
	ESO 487-003	29×30	67.4	3.6	1.08	371/376	19.03 ± 0.09
	NGC 1341	20×30	70.8	4.1	1.06	141/142	17.4 ± 0.1
	NGC 1808	20×30	64.9	3.1	1.10	261/270	19.0 ± 0.1
	PGC 073926	10×60	81.6	3.4	1.01	136/136	17.39 ± 0.08
	PGC 147285	20×30	73.8	3.2	1.04	297/300	18.97 ± 0.08
	PGC 3080859	20×30	73.1	2.08	1.05	331/342	20.2 ± 0.1
11-19	ESO 242-018	20×30	73.5	2.5	1.04	188/250	16.1 ± 0.1
	ESO 425-010	21×30	85.0	2.9	1.00	597/718	19.9 ± 0.1
	ESO 555-005	6×60	71.9	3.2	1.05	307/309	19.0 ± 0.1
	ESO 555-005	6×120	70.7	3.4	1.06	307/310	19.21 ± 0.09
	ESO 555-022	21×30	78.4	3.1	1.02	527/574	19.95 ± 0.09
	IC 2143	20×30	67.6	3.1	1.08	514/522	20.46 ± 0.09
	NGC 1341	20×30	66.9	3.2	1.09	160/164	18.56 ± 0.09
	PGC 073926	20×30	83.8	3.7	1.01	155/273	16.77 ± 0.09

Table 5.3: EABA reference stacks for GW170104.

sients that could be plausibly linked to the GW event. We did not expect to find any optical counterparts to GW170104, since the most likely explanation for that event is the merger of two black holes, neither of which are expected to emit EM radiation.

5.1.2 Observations of GW170817 targets and candidates

The TOROS collaboration used the T80S 0.83-meter reflector at CTIO to observe galaxy targets assigned by the TOROS broker on the night of 17 August 2017 (see Table 5.4 and Figure 5.2) [54] [55]. During the EM follow-up of GW170817, the One-Meter Two-Hemisphere (1M2H) collaboration detected a transient source at $\sim$11 hours after the GW trigger in the vicinity ($\sim$ 10" offset) of NGC 4993, an S0 galaxy at a distance of $\sim$40 Mpc [24] [44]. The optical transient was initially designated "SSS17a" by the discovery team (the Swope Supernova Survey); later "Astronomical Transient 2017gfo" (AT2017gfo) by the International Astronomical Union. We ceased our assigned target follow-up strategy and focused our resources on following up AT2017gfo at $\sim$35 hours post-trigger. We obtained 16, 15, and 15 one-minute exposures of NGC 4993 in SDSS *g*, *r*, and *i* passbands, respectively, at 1×1 binning using the T80S 0.83-meter reflector and an E2V CCD290-99 detector. EABA observed reference fields of NGC 4993 on 4 and 5 September 2017 using a 1.54-meter reflector and an Apogee Alta F16M camera. CTMO observed additional references on 1 and 2 July 2019 using a PlaneWave CDK17 astrograph and Apogee Alta F16M camera. Both sets of references are unfiltered and exposed with 2×2 binning.

The T80S reduction pipeline debiased and flatfielded the raw frames using the IRAF `CCDPROC` package. No dark frames were provided for further reduction. I followed the same considerations for background subtraction as detailed in Chapter 4.1.1. Since the T80S data were already plate-solved, I proceeded to align the frames using `Reproject` and median-combine them using IRAF's `imcombine` into 16×60-, 15×60-, and 15×60-second stacks in the *g*-, *r*-, and *i*-bands, respectively.

I calculated the air mass using the Kasten and Young formula at an altitude corresponding to each of the 46 frames in the entire time series. I read the seeing directly from the FITS

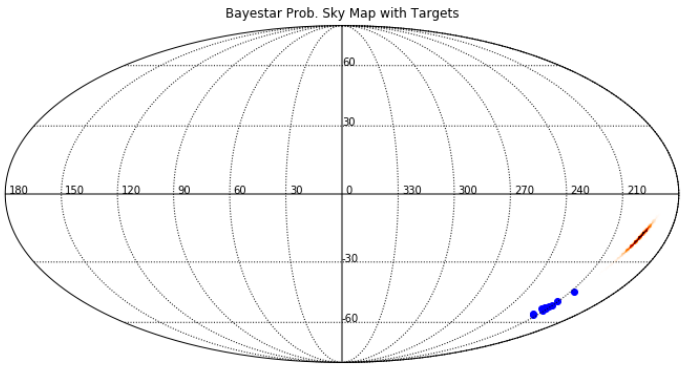

Figure 5.2: Localization skymap for GW170817 with TOROS broker assigned targets highlighted in blue. Figure from Díaz et al (2017).

header of each T80S frame. The process I used to calculate the growth curves is identical to that in Chapter 4.1.1. The growth curves of the data with the transient are further discussed in Chapter 4.3. The optimal aperture size for the EABA September 2017 stacks is a 15-pixel radius. The optimal aperture size for the CTMO July 2019 stacks is a 6-pixel radius. CCD growth curves for the target and reference frames are presented in Appendix C.

Source extraction for the T80S data is discussed further in Chapter 4.3. For the reference frames, I followed an identical procedure for source extraction and limiting magnitude estimation as described in Chapter 4.1.1. Observational parameters for the target and reference frames are reported in Tables 5.4 and 5.5, respectively. Example stacks for the targets and references are presented in Appendix A.

Filter	Stack	Alt [deg]	Seeing ["]	Air mass	Sample	Depth
g	16×60	50.2	1.9	1.58	1702/11889	22.0 ± 0.1
r	15×60	38.2	1.9	1.64	2410/17224	21.7 ± 0.1
i	15×60	37.1	1.8	1.68	2827/20509	21.6 ± 0.2

Table 5.4: CTIO T80S target stacks for GW170817.

5.2 Relative time-series photometry of AT2017gfo

I performed relative time series aperture photometry on the optical source AT2017gfo. The data from T80S observations on 18 August 2017 ∼35 hours post-trigger provide a total of 46 measurements in SDSS *gri* passbands. Reduction of these data follows the steps described in

Date	Object	Stack	Alt [deg]	Seeing ["]	Air mass	Sample	Depth
17-09-04	NGC 4993	22×60	25.5	4.6	2.31	224/239	15.2 ± 0.1
17-09-05	NGC 4993	80×30	28.5	4.2	2.09	243/259	16.4 ± 0.1
19-07-01	NGC 4993	11×120	17.2	4.5	3.35	1538/1626	19.3 ± 0.2
19-07-02	NGC 4993	20×120	33.4	3.8	1.81	2151/2542	20.1 ± 0.2

Table 5.5: EABA and CTMO reference stacks for GW170817.

Section 4.1.2. To perform a suitable calibrated photometry, it is imperative that the signal from the source is measured (1) entirely and (2) independently from the interfering signal of the host galaxy. The transient AT2017gfo has a small angular displacement from the core of NGC 4993 (see Chapter 4.4) and, therefore, the signal from NGC 4993 must be removed before measuring the transient.

For removing the signal of NGC 4993, I used the Python Photutils `isophote` package, which allows one to fit elliptical isophotes to the image of an extended body. The isophotes are measured iteratively using the method described in Jedrzejewski (1987) [69]. I calculated independent models for all 46 images plus for an additional three stacks. The centers of each galaxy are the peak pixel values which I measured using SAOImage DS9 regions. Some models failed to reach convergence depending on the particular ellipse parameters chosen at the beginning of the iterative process (e.g. sigma-clipping, semi-major axis, ellipticity, and position angle — see Chapter 5). After attempting a combination of three sigma-clip value with a distribution of values for the ellipse parameters, I selected the initial parameters for each of the 46 images as detailed in Table 5.6. A false color *gri*-to-*rgb* stack and an example of the residual (after galaxy subtraction) is shown in Figure 5.5.

	g-band	*r*-band	*i*-band
Ellipticity	0	0	0
Position angle [deg]	0	0	0
Semi-major axis [px]	15	15	10 (15 for stack)

Table 5.6: Initial ellipse model parameters for the `Isophote` package. Motivations for these particular values are discussed in Chapter 5.

I calculated the optimal aperture for photometry using CCD growth curves on AT2017gfo

in each residual image. I determined an optimal radius of six pixels to be sufficient in capturing the total flux of the source. Growth curves in each band are reported in Figure 5.3.

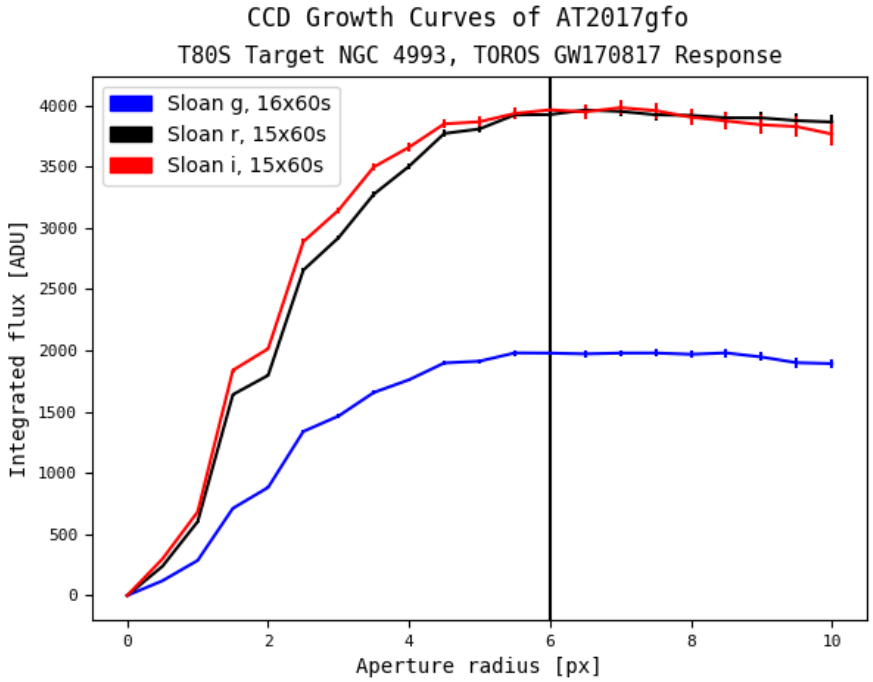

Figure 5.3: CCD growth curves of optical transient AT2017gfo in SDSS *g*-, *r*-, and *i*-passbands. Optimal aperture (6 px) is indicated by the vertical line. Flux is background- and galaxy-subtracted. Color scheme adapted from Díaz et al (2017).

I performed a 4-σ source extraction on each stack using SExtractor. I used SAOImage DS9 to cross-match the 4σ source-extracted catalog with the SDSS DR9 survey overlap in the image FOV. The magnitude difference versus SDSS color plot revealed a range of colors from $-0.6 < g - i < 3.2$, after filtering for extreme outliers due to image artifacts. I applied an iterative 3σ-clipping to the remaining values and then fit a weighted, second-order polynomial to derive color terms and the zeropoint. I report the color terms and zeropoint results in Table 5.7. With these color terms and zeropoint, I calculate an effective zeropoint for each band and calibrate the instrumental magnitudes of AT2017gfo using SDSS DR9 colors.

I performed time-series photometry on AT2017gfo across the three observed passbands using the calculated instrumental magnitudes and color information. The time series flux measurements are calibrated using the SDSS DR9 colors and placed on an apparent magnitude scale

Band	A	B	C
g	-0.0604	0.0048	-27.1535
r	0.1132	-0.0496	-27.2567
i	-0.2874	0.0793	-26.7729

Table 5.7: Color information of GW170817 stacks. A and B are first- and second-order color terms, respectively. C is the zeropoint for sources with $g - i = 0$.

as described previously. The light curves are reported in Figure 5.4.

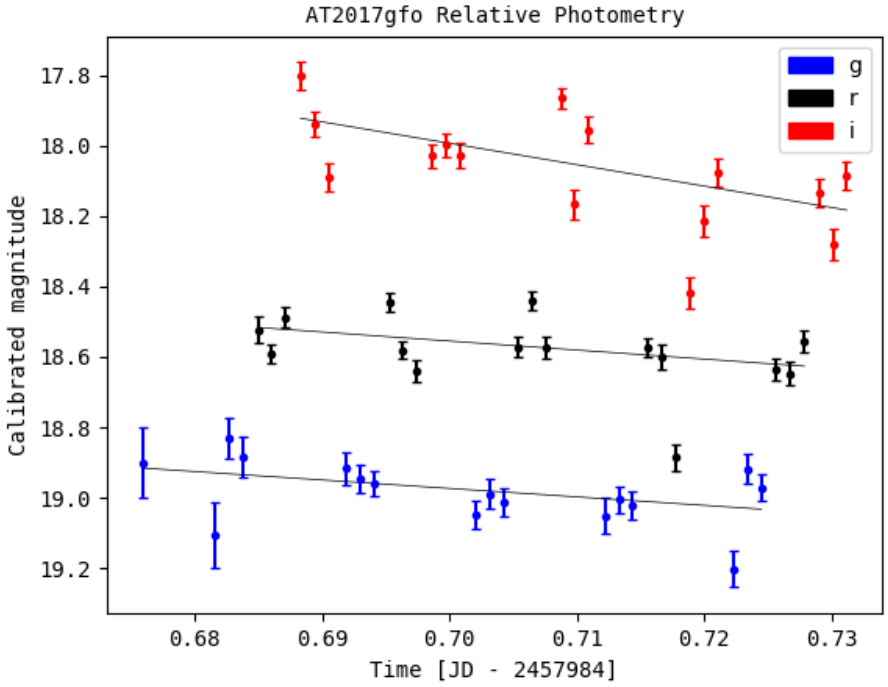

Figure 5.4: Relative photometry of optical transient AT2017gfo. From top to bottom is i-, r-, and g-bands in color scheme of Díaz et al (2017). The r-band light curve is offset $+0.3$ magnitudes (downward in graph) to distinguish from the i-band curve.

5.3 Angular diameter measurements

I measured the angular separation between AT2017gfo and the center of NGC 4993. For each stack, I determined the center pixel of both the source and NGC 4993 (both with and without subtracting the galaxy) using the ruler tool in DS9. The angular diameter θ is roughly 10.4 arcseconds from averaging the measurements from each stack (two per stack, with and without the galaxy). The results of angular diameter measurements are in Table 5.8.

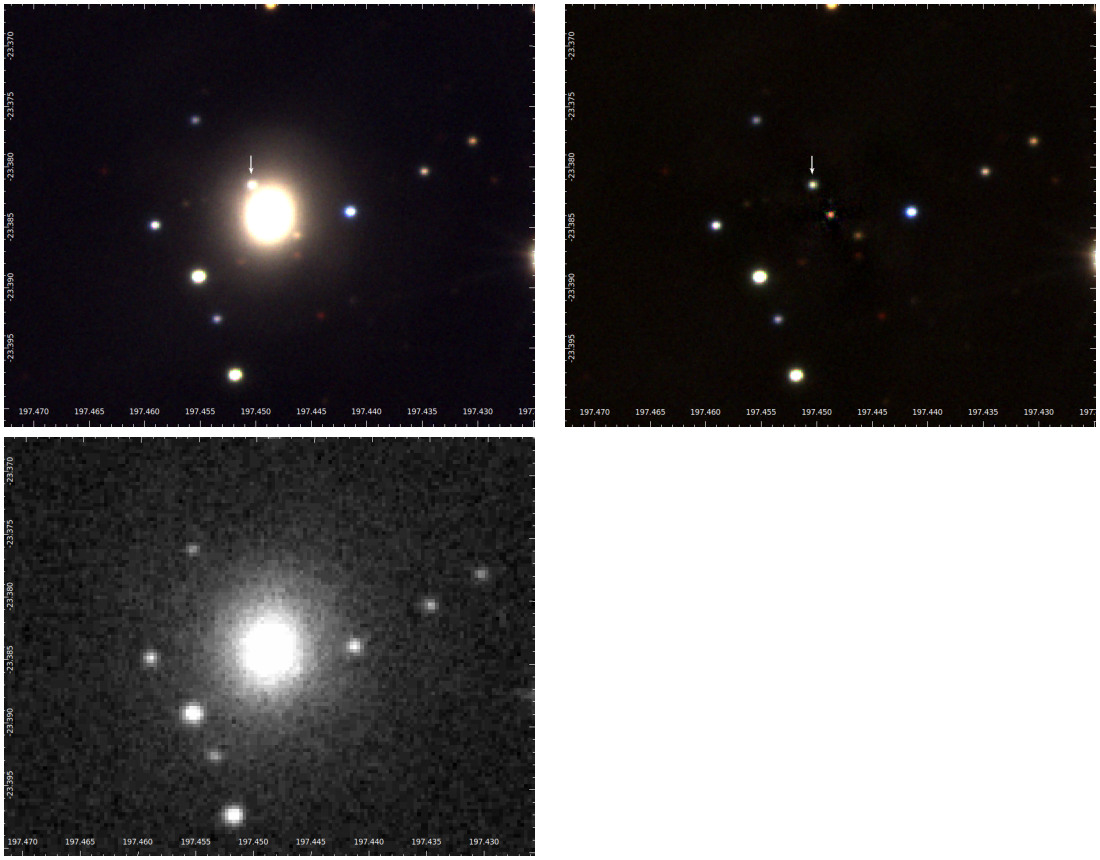

Figure 5.5: False color image produced from combined *gri* stack and residual image after isophote model subtraction. The optical transient AT2017gfo is indicated to the top left limb of the galactic core. The bottom image is a POSS-II *R*-band reference from the Digital Sky Survey archive.

Band	Angular diameter [”]	Image diameter [px]
SDSS *g*	10.52 (10.48)	21.04 (20.97)
SDSS *r*	10.22 (10.47)	20.44 (20.95)
SDSS *i*	10.42 (10.19)	20.84 (20.37)
Mean *gri*	10.39 (10.38)	20.78 (20.76)

Table 5.8: Angular measurements of the offset between AT2017gfo and NGC 4993. Measurements in parentheses indicate those taken with NGC 4993 having been first subtracted.

5.4 LIGO O3 follow-up observations

During the LIGO O3 Science Run, the TOROS network responded to the GW candidate alert S190814bv. LIGO and Virgo detected the signal of a compact binary merger on 2019-08-14 at 21:10:39 UTC. LIGO and Virgo initially estimated a >99% calculated likelihood of S190814bv having at least one component mass being within the purported "mass gap" of compact objects (i.e. between 3-5$M_{\odot}$). Further refined analyses determined the most likely explanation of the GW event to be composed of a neutron star and a black hole — the first (plausible) detection of a NSBH system [80] [81].

5.4.1 Observations of S190814bv targets and candidates

CTMO responded to S190814bv on 2019-08-15 UTC and collected image data of 10 galaxies assigned by the TOROS broker with the highest probabilities of hosting a transient (see Table 5.9 and Figure 5.6) [56]. The CTMO 17" astrograph exposed five frames per target using an Apogee Alta F16M CCD camera. The target frames are unfiltered exposures taken at 60 seconds of integration and at 2×2 binning. The frames are contaminated by high extinction due to the low altitude of the targets and interfering light caused by the $\sim$ 99% full Moon being less than 50 degrees from the targets during the observation session. Visual inspection of the frames for ESO 474-035 revealed extinction levels sufficient to warrant the removal of these data from the analysis.

In addition to following up S190814bv, CTMO responded to three optical candidates detected by the Dark Energy Survey Gravitational Wave (DESGW) and Canada-France-Hawaii-Telescope (CFHT) collaborations, both of whom responded to the trigger. The DESGW collaboration detected optical transient candidates designated desgw-190814j (AT2019nxe) and desgw-190814q (AT2019obc) and the CFHT collaboration detected an optical candidate near galaxy 2MASX J00472894-2526263, which we designate CFHT-1 [103] [108] [109]. CTMO conducted follow-up observations of these transient candidates on 2019-08-21 UTC and produced five unfiltered exposures per target, taken at 200 seconds of integration and at 2×2 binning. The DESGW

and CFHT candidates are detailed in Table 5.10.

Object	RA [J2000]	Dec [J2000]	Distance [Mpc]	Localization Probability
HL 787700	00:51:29.86	-24:38:32	274.46	6.904e-07
HL 3235460	00:53:24.79	-25:09:28	277.15	5.683e-07
HL 3235474	00:53:03.69	-25:10:42	260.39	5.479e-07
HL 3235463	00:53:17.71	-25:11:08	258.93	5.316e-07
HL 777629	00:51:17.78	-25:33:13	271.72	5.284e-07
HL 788830	00:53:57.73	-24:32:35	296.32	4.615e-07
ESO 474-035	00:52:41.58	-25:44:01	271.35	4.603e-07
HL 3235467	00:53:18.04	-25:39:13	269.46	4.598e-07
HL 3235506	00:50:21.86	-25:03:23	328.10	4.276e-07
HL 786999	00:53:04.62	-24:42:15	234.47	4.183e-07

Table 5.9: TOROS broker targets observed by CTMO on 2019-08-15 UTC for S190814bv.

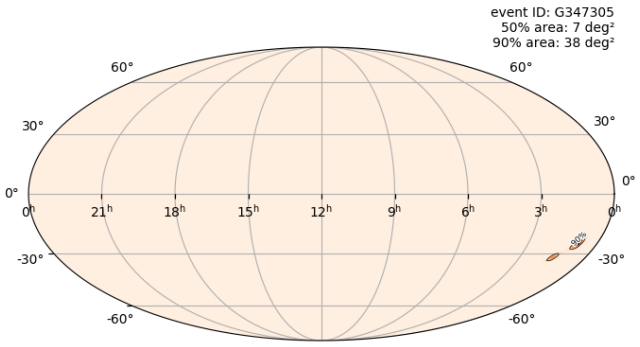

Figure 5.6: Bayestar localization skymap for S190814bv.

Object	RA [J2000]	Dec [J2000]	GCN
AT2019nxe	00:46:16.81	-24:22:21.19	25425
AT2019obe	00:58:16.02	-24:08:23.18	25438
CFHT-1	00:47:28.03	-25:26:14.15	25443

Table 5.10: Optical transient candidates to S190814bv detected by the DESGW and CFHT teams and observed by CTMO on 2019-08-21 UTC.

The steps for reduction are identical to those detailed in Chapter 4.1.1. I calculated the air

mass and seeing, as well as the catalog cross-matching to the POSS-II F-band, following an identical procedure as in Chapter 4.1.1. I measured an optimal aperture radius using growth curves to be 6-pixels. The growth curves are featured in Appendix C. All observed field parameters are presented in Table 5.11. Example stacks for the transient candidates are presented in Appendix A. The observed targets assigned by the TOROS broker featured heavy extinction (see last column of Table 5.11 and, therefore, are not included in the appendix examples.

Date	Object	Stack	Alt [deg]	Seeing ["]	Air mass	Sample	Depth
08-15	777629	5×60	31.2	3.9	1.93	258/402	17.6 ± 0.1
08-15	786999	5×60	36.4	3.7	1.68	121/201	18.56 ± 0.09
08-15	787700	5×60	26.4	3.8	2.24	221/391	18.5 ± 0.1
08-15	788830	5×60	32.8	3.6	1.84	230/394	18.3 ± 0.1
08-15	3235460	5×60	27.1	3.8	2.19	231/418	18.6 ± 0.5
08-15	3235463	5×60	30.2	3.9	1.98	275/425	18.3 ± 0.1
08-15	3235467	5×60	33.8	3.6	1.79	159/255	16.71 ± 0.07
08-15	3235474	5×60	28.6	3.7	2.08	269/430	18.4 ± 0.1
08-15	3235506	5×60	35.5	3.7	1.72	111/197	15.6 ± 0.1
08-21	AT2019nxe	5×200	34.9	4.0	1.75	465/555	18.4 ± 0.1
08-21	AT2019obe	5×200	27.1	4.0	2.19	463/544	18.7 ± 0.1
08-21	CFHT-1	5×200	38.4	3.9	1.61	582/751	19.4 ± 0.1

Table 5.11: CTMO target stacks for S190814bv.

Following our reduction method and 4-σ source search, we did not detect any optical transients that could be plausibly linked to the GW event. The atmospheric conditions of both observational epochs during this follow-up were severely sub-optimal and limited the depth of our search. Hence, we are not surprised to find zero plausible optical transients associated with S190814bv, although the fact that one merger component is deduced to be a neutron star does not rule out EM radiation having been emitted during the GW event.

CHAPTER VI

DISCUSSION AND CONCLUSION

The transient AT2017gfo exhibits significant dimming across all three bands during the 1.5 hours of time-series observations. I calculated the average of the first three points per curve (excluding the first g point, in which case I used the next three points) and the last three. By taking the difference between the average last and first measurements and dividing them by the intervening time interval, I estimate the measured dimming to be $\Delta g = (2.1 \pm 0.1)$ mag/day, $\Delta r = (1.96 \pm 0.08)$ mag/day, and $\Delta i = (5.5 \pm 0.1)$ mag/day. My measurements are valid assuming that the light curves remain linear over a day, which is not necessarily correct as we expect kilonovae to exhibit color evolution over the course of mere hours [92] [94]. Given that the total observing sequence was only 1.5 hours, a longer time coverage of AT2017gfo would have better determined the day-to-week-long color evolution. The g-band declines slightly more rapidly than the r-band, which is technically consistent with the overall qualitative predictions of kilonovae, which posit a more rapid decline in bluer bands relative to redder ones. However, the i-band exhibits a much larger decline relative to the other two bands, which is suspicious and inconsistent with the broader agreement indicating AT2017gfo having been a kilonova with a blue, rapidly-evolving lanthanide-free component and a red, slowly-evolving lanthanide-rich component [123]. Furthermore, my findings are in general disagreement with those of Díaz et al. (2017) (hereafter D17), who provided an estimated dimming of $\Delta g = (3.0 \pm 0.6)$ mag/day, $\Delta r = (2.5 \pm 0.4)$ mag/day, and $\Delta i = (1.9 \pm 0.5)$ mag/day. My values for Δg, Δr, and Δi are 3σ, 2σ, and $>5\sigma$, respectively, from their reported values. My estimated g- and r-band dimming are both lower than those found by D17 and the relative difference I found between the two rates is much smaller. My estimated i-band dimming is not only much higher than that found by D17, but also

is steeper relative to the other bands, which is additionally inconsistent with D17. At the observation time-series midpoint, the calibrated apparent magnitudes of AT2017gfo are $g = 19.02 \pm 0.06$, $r = 18.23 \pm 0.05$, and $i = 18.00 \pm 0.06$. The corresponding colors at time-series midpoint are $g - r = 0.79 \pm 0.08$, $r - i = 0.23 \pm 0.08$, and $g - i = 1.02 \pm 0.08$. D17 report apparent magnitudes at the time-series midpoint to be $g = 18.60 \pm 0.02$, $r = 17.99 \pm 0.02$, and $i = 17.80 \pm 0.02$. My measurements are 7σ, 5σ, and 3σ, respectively, from the upper limits of values reported in D17. Furthermore, the reported colors in D17 are $g - r = 0.61 \pm 0.03$, $r - i = 0.19 \pm 0.03$, and $g - i = 0.80 \pm 0.03$. My estimated colors are 2σ, 1σ, and 3σ, respectively, from the upper limits of the estimates in D17. Overall, the relative colors at time-series midpoint are close to, but not quite the same as, those found by D17. The apparent magnitudes at observation midpoint are dimmer than the values of D17. The time-dependence is inconsistent across all three bands. For the *g*- and *r*-bands, the slopes are less steep than those found by D17, and the *i*-band slope is much steeper than the D17 *i*-band curve.

From the apparent magnitudes of AT2017gfo, one can calculate the corresponding absolute magnitudes given the distance to NGC 4993. The absolute magnitude is calculated from the distance modulus equation

$$m_\lambda - M_\lambda = 5 \log d - 5 + A_\lambda \tag{6.1}$$

where m_λ is the apparent magnitude (observed at wavelength λ), M_λ is the corresponding absolute magnitude, d is the distance to the source [parsecs], and A_λ is the extinction term at wavelength λ. In order to measure the magnitude of an extra-galactic source, one must account for extinction caused by material within the intervening Milky Way in our line of sight. I use extinction coefficients $A_g = 0.407$, $A_r = 0.282$, and $A_i = 0.209$ for SDSS *g*-, *r*-, and *i*-bands, respectively, from Schlafly & Finkbeiner (2011) [106]. The calculated absolute magnitudes at ~ 35 hours post-merger are $M_g = -14.46 \pm 0.02$, $M_r = -15.08 \pm 0.02$, and $M_i = -15.27 \pm 0.02$. It is interesting that the prediction of the peak *V*-band absolute magnitude at ~ 1 day is $M_V \approx -15$ as predicted by Metzger et al. (2010) [94].

One can estimate the physical offset of AT2017gfo from the galactic core of NGC 4993, assuming that the event took place within the galaxy. NGC 4993 has a measured redshift of $z = 0.00973 \pm 0.00005$ [48], corresponding to an angular diameter distance of $d_A \sim 40.6$ Mpc as calculated via the procedure in Chapter 3.4. Using measurements of the angular diameter as detailed in Chapter 4.4 and Table 5.8, I calculated the corresponding linear diameters, which are shown in Table 6.1. Using d_A and an average angular distance $\theta \sim 10.4$ arcseconds, the corresponding (average) linear diameter is $D \sim 2040$ pc. The estimated linear diameter between AT2017gfo and the center of NGC 4993 is consistent with the measurements of Coulter et al. (2017), who give a reported linear diameter estimated of $D \sim 2$ kpc [44]. We are in a unique position to estimate what these types of events look like at various cosmological distances. If we fix $D = 2$ kpc and vary the angular diameter as a function of redshift (since we have previously derived the comoving coordinate as a function of redshift, see Chapter 3.4), we can plot the expected angular diameter of "AT2017gfo-like" events observed by an optical telescope at various distances. Even though the derivation of the comoving coordinate is an approximation, the predictions are valid out to $z \approx 0.1$ [33], which incorporates all but the expected NSBH horizon distance in the LVC O4 Science Run [8]. The plot that shows the expected angular diameter as a function of redshift is displayed in Figure 6.1. Transient hunters can use this information to select the optimal telescope/camera system that provides the proper plate scale to resolve a transient separately from its host galaxy (assuming the transient is similar to AT2017gfo).

Band	Linear diameter [pc]
SDSS *g*	2071 (2063)
SDSS *r*	2012 (2061)
SDSS *i*	2051 (2006)
Mean *gri*	2045 (2043)

Table 6.1: The linear diameter between AT2017gfo and the core of NGC 4993 as measured in the three SDSS *gri*-bands. Measurements in parentheses indicate those taken with NGC 4993 having been first subtracted with an isophote model.

I did not detect any plausible optical transients associated with GW170104 or S190814bv. Many reference frames were worse than the target frames in terms of limiting magnitude. In

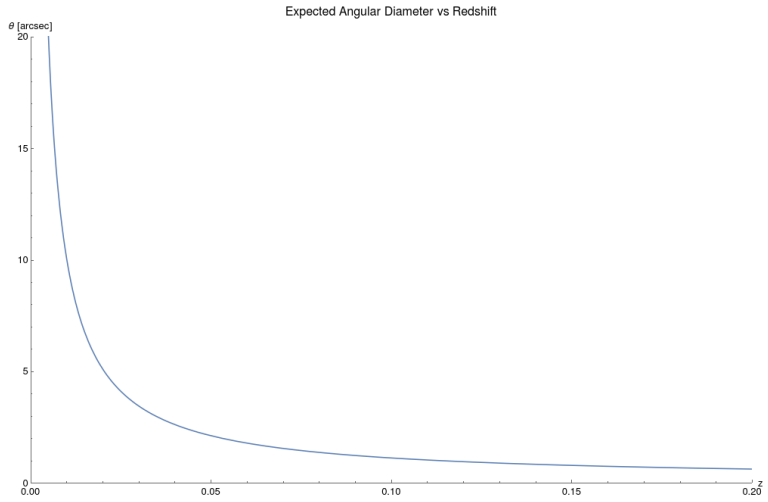

Figure 6.1: Expected angular separation as a function of redshift for AT2017gfo-like events

practice, references should be of higher quality than the target frames, particularly for conducting proper image subtraction [25]. For S190814bv, the fields were simply not deep enough in magnitude to detect anything claimed by other teams in the EM follow-up community. Low altitude ($<$ 30 degrees), extinction from a nearby ($<$ 50 degrees angular distance) full Moon, and high/variable cloud coverage all caused the fields of S190814bv to lack sufficient depth. Deeper exposures will be needed for future transient searches, particularly once the current GW detector network reaches full design sensitivity and, hence, maximum horizon distance for BNS/NSBH mergers. For a telescope with a small FOV, one needs both longer exposure times and a larger stack sequence (although exposure time seems to be more important to maximize SNR than the stack size). Additionally, I need to incorporate tests of confidence in my ability to extract sources. Typically, this is done by introducing a population of "false transients" into the real data, and then seeing how many the source extraction method retrieves (i.e. the more, the better) [18]. My pipeline does not incorporate injections test, which is crucial for any source extraction, and will be added in future studies.

Galaxy modeling is a new feature of the pipeline and needs to be better understood for incorporation into an automated routine. Initial attempts to construct and subtract isophote models resulted in spurious sources, significant background dips near the transient, and evident ring/halo

distortion near the galaxy core. The subtraction quality is improved and the spurious results are minimized with the introduction of sigma-clipping and higher ellipse harmonics while constructing an isophote model. Better yet would be to mask sources within the region of the galaxy before constructing the model. During analysis of AT2017gfo, some frames failed to reach convergence on a particular isophote model. Failure seems to be based on a number of factors, including sigma-clipping and the initial model parameter guesses. Sigma-clipping appears to play a role in the failure — on multiple occasions during analysis, the same frame would converge to a model at a given level of sigma-clipping (e.g. 2σ), but would fail to converge at another level (e.g. 2.5σ) even while keeping all other parameter choices fixed. I attempted to make three models per image with varying levels of sigma-clipping. If more than one succeeded to converge, I chose one based on the levels of morphological distortion visually evident on the residual image. Another reason for the models to fail convergence is likely the imperfect nature of the initial guess aperture. I took advantage of the fact that NGC 4993 is an elliptical galaxy — while not entirely symmetrical, the case of fitting ellipses to an elliptical galaxy is much more straightforward than that of modeling a spiral or irregular galaxy (although the pipeline should answer the case of different galaxy types in future versions). Although the isophote model makes several iterations and converges to a more accurate solution, the initial guess is crucial for deciding on the outcome of successfully building a model. I set the initial ellipticity and position angle of the galaxy both to zero. NGC 4993 has a reported ellipticity of ~ 0.15, so a circular aperture is not nearly ideal. However, when initializing with an ellipticity of 0.15, the convergence fails. Position angle gave similar results — realistically (and more probably) failure to converge is due to a poor choice of initial values for both ellipticity and position angle. I chose an initial semi-major axis that roughly captured the majority of core signal in each image. A radius of 15-pixels seemed to fit across all bands and images, however the *i* time-series would only accept a 10-pixel aperture radius (except for the stack, which converged using a 15-pixel radius). The large discrepancy between the *i*-band and the other two bands is probably caused by this unresolved limitation. The initial aperture guess was sufficient for the model-building process to produce at least one

successful convergence per triplet of sigma-clipped models. The time-series was not consistently sigma-clipped, which could be a cause for the spread in points (particularly for the *i*-band curve). Galaxy modeling, particularly involving fitting elliptical isophotes, is in its infancy being incorporated into the pipeline. I intend to investigate why convergence fails and why the *i*-band light curve behaves drastically different than the other two curves. Perhaps galaxy modeling is only best achieved "by hand" and, thus, not appropriate for an automatic routine (unless perhaps it is used more as a transient "detection" system, with refined "characterization" necessitating a more finely-tuned fit). In D17, the approach to remove the galaxy is by fitting a Sérsic profile, which is an analytical approach, and only best done by hand for any reasonable accuracy to be achieved with photometry [50].

The problem addressed in this thesis is — *How can small observatories follow-up and observe astrophysical transients?* In particular, this thesis aimed to demonstrate (1) how an astronomical observatory should respond to a GW event, (2) how one should process the imaging data obtained during an optical follow-up response, and (3) how one measures such a transient upon discovery.

- The TOROS collaboration responded to three events during the LIGO-Virgo O2 and O3 campaigns: GW170104, a BBH merger; GW170817, BNS merger; S190814bv a NSBH merger. Visual inspection and catalog cross-matching were conducted on the optical response data. No counterparts were detected for GW170104 nor S190814bv. An optical counterpart to GW170817, AT2017gfo, was observed with instruments in the TOROS network.

- Relative time-series photometry was performed on AT2017gfo in SDSS *gri* passbands. The light curve reveals a rapidly fading transient source. Elliptical isophote modeling and subtraction of the host galaxy reveal an isolated optical transient not associated with previous archival data.

- Angular measurements of the separation of AT2017gfo from the core of NGC 4993 reveal

a $\sim$ 10.4 arcsecond offset, corresponding to a linear diameter of $\sim$ 2 kpc at a luminosity distance of $\sim$ 40 Mpc.

- Small FOV telescopes should follow a target selection strategy when during transient GW counterpart searches. The optical system of such a telescope should have the necessary magnitude depth to confidently detect sources and plate scale to resolve an offset source from its potential host galaxy. The system should incorporate at least three photometric filters covering the optical/NIR bandwidth to derive color information from a fading transient — crucial for comparing to kilonova models and constraining the physical properties of the progenitor and post-merger product.

- A reduction and analysis pipeline has been designed and is in its infancy. The response to a GW trigger must be quick, from target selection and observation of targets to reduction and analysis. The CTMO Analysis Pipeline (CAL) handles the bulk of this analysis by following a number of strategies, including catalog cross-matching and galaxy subtraction. Automation and integration of features such as DIA is planned.

BIBLIOGRAPHY

[1] M. G. Aartsen and et al. Multimessenger Observations of a Flaring Blazar Coincident with High-Energy Neutrino IceCube-170922A. *Science*, 361(6398):70, 2018.

[2] J. Aasi and et al. Advanced LIGO. *Classical and Quantum Gravity*, 32(7):1–42, 2014.

[3] B. P. Abbott and et al. Observation of Gravitational Waves from a Binary Black Hole Merger. *Physical Review Letters*, 116(061102):1–16, 2016.

[4] B. P. Abbott and et al. Astrophysical Implications of the Binary Black Hole Merger GW150914. *The Astrophysical Journal Letters*, 818(L22):15, 2016.

[5] B. P. Abbott and et al. GW170104: Observation of a 50-Solar-Mass Binary Black Hole Coalescence at Redshift 0.2. *Physical Review Letters*, 118(221101), 2017.

[6] B. P. Abbott and et al. GW170817: Observation of Gravitational Waves from a Binary Neutron Star Inspiral. *Physical Review Letters*, 119(161101):1–18, 2017.

[7] B. P. Abbott and et al. Gravitational Waves and Gamma-Rays from a Binary Neutron Star Merger: GW170817 and GRB 170817A. *The Astrophysical Journal Letters*, 848 (L13):27, 2017.

[8] B. P. Abbott and et al. Prospects for Observing and Localizing Gravitational-Wave Transients with Advanced LIGO, Advanced Virgo and KAGRA. *Living Reviews in Relativity*, 21(1):57, 2018.

[9] B. P. Abbott and et al. GWTC-1: A Gravitational-Wave Transient Catalog of Compact Binary Mergers Observed by LIGO and Virgo During the First and Second Observing Runs. *Physical Review X*, 9(031040):1–49, 2019.

[10] A. Abramovici, W. E. Althouse, R. W. P. Drever, Y. Gursel, S. Kawamura, F. J. Raab, D. Shoemaker, L. Sievers, R. E. Spero, K. S. Thorne, R. E. Vogt, R. Weiss, S. E. Whitcomb, and M. E. Zucker. LIGO: The Laser Interferometer Gravitational-Wave Observatory. *Science*, 256(5055):325–333, 1992.

[11] T. Accadia and et al. Virgo: A Laser Interferometer to Detect Gravitational Waves. *Journal of Instrumentation*, 7(3):3012, 2012.

[12] F. Acernese and et al. Advanced Virgo: A Second-Generation Interferometric Gravitational Wave Detector. *Classical and Quantum Gravity*, 32(2), 2015.

[13] S. M. Adams, M. M. Kasliwal, and N. Blagorodnova. LIGO/Virgo G298048: Precise Position of SSS17a Based on HST and Gaia. NASA GCN Circular 21816, 2017.

[14] C. Alard and R. H. Lupton. A Method for Optimal Image Subtraction. *The Astrophysical Journal*, 503(1):325–331, 1998.

[15] S. Allam, J. Annis, E. Berger, D. J. Brout, D. Brown, R. E. Butler, H.-Y. Chen, R. Chornock, E. Cook, P. Cowperthwaite, H. T. Diehl, A. Drlica-Wagner, M. R. Drout, R. J. Foley, W. Fong, D. Fox, J. Frieman, R. Gruendl, K. Herner, D. Holz, R. Kessler, R. Margutti, J. Marshall, E. Neilsen, M. Nicholl, F. Paz-Chincon, A. Rest, M. Sako, D. Scolnic, N. Smith, M. Soares-Santos, D. Tucker, V. A. Villar, P. K. G. Williams, and B. Yanny. LIGO/Virgo G298048: DECam Optical Candidate. NASA GCN Circular 21530, 2017.

[16] I. Arcavi, G. Hosseinzadeh, D. A. Howell, C. McCully, D. Poznanski, D. Kasen, J. Barnes, M. Zaltzman, S. Vasylyev, D. Maoz, and S. Valenti. Optical Emission from a Kilonova Following a Gravitational-Wave-Detected Neutron-Star Merger. *Nature*, 551: 64–66, 2017.

[17] W. D. Arnett, J. N. Bahcall, R. P. Kirshner, and S. E. Woosley. Supernova 1987A. *Annual Review of Astronomy and Astrophysics*, 27:629–700, 1989.

[18] R. Artola, M. Beroiz, J. Cabral, R. Camuccio, M. Castillo, V. Chavushyan, C. Colazo, H. Cuevas Larenas, D. L. DePoy, M. C. Díaz, M. Domínguez, D. Dultzin, D. Fernández, A. C. Ferreyra, A. Fonrouge, J. Franco, D. Grana, C. Girardini, S. Gurovich, A. Kanaan, D. Garcia Lambas, M. Lares, A. F. Hinojosa, A. Hinojosa, A. F. Hinojosa, O. López-Cruz, L. M. Macri, J. L. Marshall, R. Melia, W. Mendoza, J. L. Nilo Castellón, N. Padilla, V. Perez, T. Penuela, W. Rattray, V. Renzi, E. Ríos-López, A. Ramírez Rivera, T. Ribeiro, H. Rodriguez, B. Sánchez, M. Schneiter, W. Schoenell, M. Starck, R. Vrech, C. Quinones, L. Tapia, M. Tornatore, S. Torres-Flores, E. Vilchis, and A. Zadrożny. TOROS Optical Follow-Up of the Advanced LIGO-Virgo O2 Second Observational Campaign. *Monthly Notices of the Royal Astronomical Society (accepted)*, 2020.

[19] K. Barbary. SEP: Source Extractor as a Library. *Journal of Open Source Software*, 1(6): 1–58, 2016.

[20] I. Bartos, S. Countryman, C. Finley, E. Blaufuss, R. Corley, Z. Marka, and S. Marka. LIGO/Virgo G298048: COINCIDENT IceCube Neutrino Candidate with Fermi GBM Trigger 524666471/170817529. NASA GCN Circular 21511, 2017.

[21] I. Bartos, S. Countryman, C. Finley, E. Blaufuss, R. Corley, Z. Marka, and S. Marka. LIGO/Virgo G298048: UPDATE on IceCube Neutrino Candidates — No Coincidence with Newest GW Skymap. NASA GCN Circular 21568, 2017.

[22] M. Benacquista, C. Belczynski, M. Branchesi, M. Beroiz, C. Colazo, M. C. Díaz, M. Dominguez, D. Garcia Lambas, S. Liang, L. Macri, T. Penuela, B. Sanchez, M. Schneiter, and C. V. Torres. A Program for Optical Observations of Advanced LIGO Early Triggers in the Southern Hemisphere. *EAS Publications Series*, 67-68: 357–358, 2014.

[23] E. Berger, W. Fong, and R. Chornock. An r-Process Kilonova Associated with the Short-Hard GRB 130603B. *The Astrophysical Journal Letters*, 774(L23):4, 2013.

[24] E. Berger, D. A. Coulter, C. D. Kilpatrick, M. R. Siebert, R. J. Foley, B. J. Shappee, M. R. Drout, J. S. Simon, A. L. Piro, and A. Rest. LIGO/Virgo G298048: Potential Optical Counterpart Discovered by Swope Telescope. NASA GCN Circular 21529, 2017.

[25] M. Beroiz. *Optical Counterparts to Gravitational Waves*. PhD thesis, University of Texas at San Antonio, 2017.

[26] M. Beroiz, J. B. Cabral, and B. Sanchez. Astroalign: A Python Module for Astronomical Image Registration. *arXiv preprint arXiv:1909.02946*, 2019.

[27] E. Bertin and S. Arnouts. SExtractor: Software for Source Extraction. *Astronomy and Astrophysics Supplement*, 117:393–404, 1996.

[28] M. Bolte. Signal-to-Noise in Optical Astronomy. AY 257: Modern Observational Techniques, 2006.

[29] P. Bouchet, R. Stanga, T. Le Bertre, N. Epchtein, W. R. Hamann, and D. Lorenzetti. Infrared Photometry of SN 1987A. *Astronomy and Astrophysics*, 177:L9–L12, 1987.

[30] P. Bouchet, R. Stanga, A. Moneti, T. Le Bertre, J. Manfroid, G. Silvestro, and E. Slezak. Infrared Photometry of Supernova 1987A - the First Four Months. *Proceedings of the ESO Workshop on the SN 1987 A*, 26:79–87, 1987.

[31] D. M. Bramich. A New Algorithm for Difference Image Analysis. *Monthly Notices of the Royal Astronomical Society: Letters*, 386(1):L77–L81, 2008.

[32] M. R. Calabretta and E. W. Greisen. Representations of Celestial Coordinates in FITS. *Astronomy and Astrophysics*, 395:1077–1122, 2002.

[33] B. W. Carroll and D. A. Ostlie. *An Introduction to Modern Astrophysics*. Cambridge University Press, 2nd edition, 2017.

[34] M. Castillo. Pipeline for Variable Star Detection and Eclipsing Binary Characterization. Master's thesis, University of Texas Rio Grande Valley, 2019.

[35] A. J. Castro-Tirado, R. Sánchez-Ramírez, J. Gorosabel, F. J. Aceituno, E. Sonbas, Tüver, H. Kirbiyik, and D. García-Alvárez. GRB 130603B: Optical Follow-Up and Independent GTC Redshift. NASA GCN Circular 14747, 2013.

[36] R. M. Catchpole, J. W. Menzies, A. S. Monk, W. F. Wargau, D. Pollaco, B. S. Carter, P. A. Whitelock, F. Marang, C. D. Laney, L. A. Balona, M. W. Feast, T. H. H. Lloyd Evans, K. Sekiguchi, J. D. Laing, D. M. Kilkenny, J. Spencer Jones, G. Roberts, A. W. J. Cousins, G. van Vuuren, and H. Winkler. Spectroscopic and Photometric Observations of SN 1987A - II. Days 51 to 134. *Monthly Notices of the Royal Astronomical Society*, 229:15P–25P, 1987.

[37] J. Cervantes-Cota, S. Galindo-Uribarri, and G. Smoot. A Brief History of Gravitational Waves. *Universe*, 2(3):22, 2016.

[38] R. Chornock, R. J. Foley, W. Fong, E. Berger, and S. Jha. GRB 130603B: Magellan Redshift Confirmation. NASA GCN Circular 14745, 2013.

[39] K. A. Collins, J. F. Kielkopf, K. G. Stassun, and F. V. Hessman. AstroImageJ: Image Processing and Photometric Extraction for Ultra-Precise Astronomical Light Curves. *The Astronomical Journal*, 153(77):1–13, 2017.

[40] V. Connaughton, L. Blackburn, M. S. Briggs, J. Broida, E. Burns, J. Camp, T. Dal Canton, N. Christensen, A. Goldstein, R. Hamburg, C. M. Hui, P. Jenke, D. Kocevski, N. Leroy, T. Littenberg, J. McEnery, R. Preece, J. Racusin, P. Shawhan, K. Siellez, L. Singer, J. Veitch, P. Veres, and C. Wilson-Hodge. LIGO/Virgo G298048: Fermi GBM Trigger 170817.529 and LIGO Single IFO Trigger. NASA GCN Circular 21506, 2017.

[41] A. Corsi, G. Hallinan, K. Mooley, D. A. Frail, M. M. Kasliwal, and N. T. Palliyaguru. LIGO/Virgo G298048: Radio Detection of SSS17a at 6 GHz with the VLA. NASA GCN Circular 21815, 2017.

[42] E. Costa, M. Feroci, F. Frontera, G. Zavattini, L. Nicastro, E. Palazzi, G. Spoliti, L. Di Ciolo, A. Coletta, G. D'Andreta, J. M. Muller, R. Jager, J. Heise, and J in't Zand. GRB 970228. Central Bureau for Astronomical Telegrams, International Astronomical Union, Circular No. 6752, 1997.

[43] E. Costa, F. Frontera, J. Heise, M. Feroci, J. in't Zand, F. Fiore, M. N. Cinti, D. Dal Fiume, L. Nicastro, M. Orlandini, E. Palazzi, M. Rapisarda, G. Zavattini, R. Jager, A. Parmar, A. Owens, S. Molendi, G. Cusumano, M. C. Maccarone, S. Giarrusso, A. Coletta, L. A. Antonelli, P. Giommi, J. M. Muller, L. Piro, and R. C. Butler. Discovery of an X-Ray Afterglow Associated with the Gamma-Ray Burst of 28 February 1997. *Nature*, 387(6635):783–785, 1997.

[44] D. A. Coulter, R. J. Foley, C. D. Kilpatrick, M. R. Drout, A. L. Piro, B. J. Shappee, M. R. Siebert, J. D. Simon, N. Ulloa, D. Kasen, B. F. Madore, A. Murgula-Berthier, Y.-C. Pan, J. X. Prochaska, E. Ramirez-Ruiz, A. Rest, and C. Rojas-Bravo. Swope Supernova Survey 2017a (SSS17a), the Optical Counterpart to a Gravitational Wave Source. *Science*, 358:1556–1558, 2017.

[45] A. Cucchiara, D. Perley, and S. B. Cenko. GRB 130603B: Gemini Observations. NASA GCN Circular 14748, 2013.

[46] G. Dálya, G. Galgóczi, L. Dobos, Z. Frei, I. S. Heng, R. Macas, C. Messenger, P. Raffai, and R. S. de Souza. GLADE: A Galaxy Catalogue for Multimessenger Searches in the Advanced Gravitational-Wave Detector Era. *Monthly Notices of the Royal Astronomical Society*, 479(2):2374–2381, 2018.

[47] A. de Ugarte Postigo, D. Malesani, D. Xu, P. Jakobsson, J. Datson, R. Salinas, T. Au-

gusteijn, and Y. Martinez-Osorio. GRB 130603B: Afterglow Detection from NOT. NASA GCN Circular 14743, 2013.

[48] G. de Vaucouleurs, A. de Vaucouleurs, Jr. H. G. Corwin, R. J. Buta, G. Paturel, and P. Fouque. *Third Reference Catalogue of Bright Galaxies*. Springer, New York, NY (USA), 1991.

[49] M. C. Díaz. TOROS, the Present and the Future: A Project Status Report. UTRGV Department of Physics and Astronomy Colloquium, 2019.

[50] M. C. Díaz and et al. Observations of the First Electromagnetic Counterpart to a Gravitational-wave Source by the TOROS Collaboration. *The Astrophysical Journal Letters*, 848(29):5, 2017.

[51] M. C. Díaz, M. Benacquista, K. Belczyński, M. Branchesi, E. Brocato, D. L. DePoy, M. Dominguez, D. Garcia Lambas, L. M. Macri, J. L. Marshall, R. J. Oelkers, and C. V. Torres. The TOROS Project. *Proceedings of the Third Hot-Wiring the Transient Universe Workshop*, 2013.

[52] M. C. Díaz, M. Beroiz, T. Penuela, L. M. Macri, R. J. Oelkers, W. Yuan, D. G. Lambas, J. Cabral, C. Colazo, M. Domíngeuz, B. Sánchez, S. Gurovich, M. Lares, M. Schneiter, D. Grana, V. Renzi, H. Rodriguez, M. Starck, R. Vrech, R. Artola, A. C. Ferreyra, C. Girardini, C. Quinones, L. Tapia, M. Tornatore, J. L. Marshall, D. L. DePoy, M. Branchesi, E. Brocato, N. Padilla, N. A. Pereyra, S. Mukherjee, M. Benacquista, and J. Key. GW150914: First Search for the Electromagnetic Counterpart of a Gravitational-Wave Event by the TOROS Collaboration, 2016.

[53] M. C. Díaz, M. Castillo, and A. Hinojosa. Measuring the Zero Point and the Limiting Magnitude in White-Light Images. PHYS 5287: Astronomical Photometry, 2016.

[54] M. C. Díaz, D. Garcia Lambas, L. Macri, and J. L. Nilo Castellon. LIGO/Virgo G298048: TOROS Optical Counterpart Search. NASA GCN Circular 21619, 2017.

[55] M. C. Díaz, L. Macri, J. L. Nilo Castllon, B. Sanchez, C. Mendes, C. Colazo, M. Schneitter, C. Girardini, D. Garcai Lambas, M. Beroiz, A. Zadrożny, R. Camuccio, M. Castillo, and J. Garcia. LIGO/Virgo G298048: TOROS Photometry of SSS17a. NASA GCN Circular 21985, 2017.

[56] M. C. Díaz, D. Garcia Lambas, L. Macri, J. L. Nilo Castellon, O. Lopez-Cruz, R. Camuccio, E. Caputa, and W. Mendoza. LIGO/Virgo S190814bv: No Counterpart Candidates in TOROS Observations. NASA GCN 25349, 2019.

[57] S. A. Eddington. The Propagation of Gravitational Waves. *Proceedings of the Royal Society A*, 102:268–282, 1922.

[58] D. Eichler, M. Livio, T. Piran, and D. N. Schramm. Nucleosynthesis, Neutrino Bursts and Gamma-rays from Coalescing Neutron Stars. *Letters to Nature*, 340:126–128, 1989.

[59] A. Einstein. Näherungsweise Integration der Feldgleichungen der Gravitation. *Sitzungsberichte der Preußische Akademie der Wissenschaften*, 1:688–696, 1916.

[60] A. Einstein and N. Rosen. On Gravitational Waves. *Journal of the Franklin Institute*, 223: 43–54, 1937.

[61] W. Fong, R. Margutti, and D. Haggard. LIGO/Virgo G298048: Continued X-ray Monitoring and X-ray Detection of GW170817 [erratum]. NASA GCN Circular 21786, 2017.

[62] D. Frederiks, S. Golenetskii, R. Aptekar, E. Mazets, V. Pal'shin, P. Oleynik, M. Ulanov, D. Svinkin, and T. Cline. Konus-Wind Observation of GRB 130603B. NASA GCN Circular 14771, 2013.

[63] C. Freiburghaus, S. Rosswog, and F.-K. Thielemann. r-Process in Neutron Star Mergers. *The Astrophysical Journal*, 525:L121–L124, 1999.

[64] E. W. Greisen and M. R. Calabretta. Representations of World Coordinates in FITS. *Astronomy and Astrophysics*, 395:1061–1075, 2002.

[65] C. Hanna, I. Mandel, and W. Vousden. Utility of Galaxy Catalogs for Following Up Gravitational Waves from Binary Neutron Star Mergers with Wide-Field Telescopes. *The Astrophysical Journal*, 784(8):1–7, 2014.

[66] S. B. Howell. CCD Growth Curves: Application to Faint and Crowded Point Sources. *CCDs in Astronomy; Proceedings of the Conference*, A91-45976(19-33):312–318, 1990.

[67] S. B. Howell and W. J. Merline. Applications of a Realistic Model for CCD Imaging. *IAU Symposium No. 167, New Developments in Array Technology and Applications*, pages 371–372, 1995.

[68] R. A. Hulse and J. H. Taylor. Discovery of a Pulsar in a Binary System. *The Astrophysical Journal*, 195:L51–L53, 1975.

[69] R. I. Jedrzejewski. CCD Surface Photometry of Elliptical Galaxies - I. Observations, Reduction and Results. *Monthly Notices of the Royal Astronomical Society*, 226:747–768, 1987.

[70] W. A. Joye and E. Mandel. New Features of SAOImage DS9. *Astronomical Data Analysis Software and Systems XII ASP Conference Series*, 295:489–492, 2003.

[71] F. Kasten and A. T. Young. Revised Optical Air Mass Tables and Approximation Formula. *Applied Optics*, 28(22):4735–4738, 1989.

[72] I. R. King. The Profile of a Star Image. *Publications of the Astronomical Society of the Pacific*, 83(492):199–201, 1971.

[73] D. Lang, D. W. Hogg, K. Mierle, M. Blanton, and S. Rowels. Astrometry.net: Blind Astrometric Calibration of Arbitrary Astronomical Images. *The Astronomical Journal*, 139 (5):1782–1800, 2010.

[74] B. M. Lasker and et al. The Second-Generation Guide Star Catalog: Description and Properties. *The Astronomical Journal*, 136(2):735–766, 2008.

[75] J. M. Lattimer and D. N. Schramm. Black-Hole-Neutron-Star Collisions. *The Astrophysical Journal*, 192(2):L145–L147, 1974.

[76] A. J. Levan, N. R. Tanvir, K. Wiersema, O. Hartoog, K. Kolle, J. Mendez, and T. Kupfer. GRB 130603B: WHT Optical Afterglow Candidate. NASA GCN Circular 14742, 2013.

[77] L.-X. Li and B. Paczyński. Transient Events from Neutron Star Mergers. *The Astrophysical Journal*, 507(1):L59–L62, 1998.

[78] LVC. LIGO/Virgo G268556: Identification of a GW CBC Candidate. NASA GCN Circular 20364, 2017.

[79] LVC. LIGO/Virgo G298048: Fermi GBM Trigger 524666471/170817529: LIGO/Virgo Identification of a Possible Gravitational-Wave Counterpart. NASA GCN Circular 21505, 2017.

[80] LVC. LIGO/Virgo S190814bv: Identification of a GW Compact Binary Merger Candidate. NASA GCN 25324, 2019.

[81] LVC. LIGO/Virgo S190814bv: Update on Sky-Localization and Source-Classification. NASA GCN 25333, 2019.

[82] L. Macri. Private communication. 2019.

[83] B. G. Marsden. Supernova 1987A in the Large Magellanic Cloud. Central Bureau for Astronomical Telegrams, International Astronomical Union, Circular No. 4316, 1987.

[84] J. L. Marshall and D. L. DePoy. Flattening Scientific Imaging Data with a Dome Flat-Field System. *Publications of the Astronomical Society of the Pacific*, 125:1277–1284, 2013.

[85] F. Masci. Flux-Uncertainty from Aperture Photometry.

[86] F. Masci. Private communication. 2019.

[87] C. McCully, S. Crawford, G. Kovacs, E. Tollerud, E. Betts, L. Bradly, M. Craig, J. Turner, O. Streicher, B. Sipocz, T. Robitaille, and C. Deil. astropy/astroscrappy: v1.0.5 Zenodo Release. Zenodo, 2018.

[88] A. Melandri, W. H. Baumgartner, D. N. Burrows, J. R. Cummings, N. Gehrels, C. Gronwall, K. L. Page, D. M. Palmer, R. L. C. Starling, and T. N. Ukwatta. GRB 130603B: Swift Detection of a Bright Short Burst. NASA GCN Circular 14735, 2013.

[89] A. Melandri, S. Campana, S. Covino, P. D'Avanzo, G. Greco, M. Branchesi, L. Amati D. Fugazza, L. A. Antonelli, S. Ascenzi, S. Benetti, M.T. Botticella, E. Cappellaro, V. D'Elia, F. Getman, A. Grado, L. Limatola, M. Lisi, L. Nicastro, E. Palazzi, E. Pian, S. Piranomonte, L. Pulone, A. Rossi, G. Stratta, G. Tagliaferri, V. Testa, L . Tomasella, S. Yang, and E. Brocato. LIGO/Virgo G298048: REM Optical/NIR Observations of Candidate in NGC 4993. NASA GCN Circular 21532, 2017.

[90] J. W. Menzies, R. M. Catchpole, G. van Vauuren, H. Winkler, C. D. Laney, P. A. Whitelock, A. W. J. Cousins, B. S. Carter, F. Marang, T. H. H. Lloyd Evans, G. Roberts, D. Kilkenny, J. Spencer Jones, K. Sekiguchi, A. P. Fairall, and R. D. Wolstencroft. Spectroscopic and Photometric Observations of SN 1987A: the First 50 Days. *Monthly Notices of the Royal Astronomical Society*, 227:39P–49P, 1987.

[91] W. J. Merline and S. B. Howell. A Realistic Model for Point-Sources Imaged on Array Detectors: The Model and Initial Results. *Experimental Astronomy*, 6(1):163–210, 1995.

[92] B. D. Metzger. Kilonovae. *Living Reviews in Relativity*, 23(1):1–95, 2019.

[93] B. D. Metzger and E. Berger. What is the Most Promising Electromagnetic Counterpart of a Neutron Star Binary Merger? *The Astrophysical Journal*, 746(48):1–15, 2012.

[94] B. D. Metzger, G. Martínez-Pinedo, S. Darbha, E. Quataert, A. Arcones, D. Kasen, R. Thomas, P. Nugent, I. V. Panov, and N. T. Zinner. Electromagnetic Counterparts of Compact Object Mergers Powered by the Radioactive Decay of r-Process Nuclei. *Monthly Notices of the Royal Astronomical Society*, 406(4):2650–2662, 2010.

[95] K. P. Mooley, G. Hallinan, and A. Corsi. LIGO/Virgo G298048: Radio Detection of SSS17a at 3GHz with the VLA/JAGWAR. NASA GCN Circular 21814, 2017.

[96] E. Nakar and T. Piran. Detectable Radio Flares Following Gravitational Waves from Mergers of Binary Neutron Stars. *Nature*, 478(7367):82–84, 2011.

[97] R. Narayan, B. Paczyński, and T. Piran. Gamma-Ray Bursts as the Death Throes of Massive Binary Stars. *The Astrophysical Journal*, 395:L83–L86, 1992.

[98] M. V. Newberry. Signal-to-Noise Considerations for Sky-Subtracted CCD Data. *Publications of the Astronomical Society of the Pacific*, 103:122–130, 1991.

[99] F. A. E. Pirani. On the Physical Significance of the Riemann Tensor. *Acta Physica Polonica*, 15:389–405, 1956.

[100] V. Quetschke. Advanced LIGO's Third Observing Run Has Begun. UTRGV Department of Physics and Astronomy Colloquium, 2019.

[101] V. Renzi, R. Vrech, D. Ferreiro, D. García Lambas, M. Solinas, H. Muriel, J. Viramonte, M. Sarazin, and P. Recabarren. Caracterización astronómica del sitio Cordón Macón en la provincia de Salta. *Boletín de la Asociación Argentina de Astronomía*, 52:285–288, 2009.

[102] T. P. Robitaille, E. J. Tollerud, P. Greenfield, M. Droettboom, E. Bray, T. Aldcroft, M. Davis, A. Ginsburg, A. M. Price-Whelan, W. E. Kerzendorf, A. Conley, N. Crighton, K. Barbary, D. Muna, H. Ferguson, F. Grollier, M. M. Parikh, P. H. Nair, H. M. Unther, C. Dell, J. Woillez, S. Consell, R. Kramer, J. E. H. Turner, L. Singer, R. Fox, B. A. Weaver, V. Zabalza, Z. I. Edwards, K. Azalee Bostroem, D. J. Burke, A. R. Casey, S. M. Crawford, N. Dencheva, J. Ely, T. Jenness, K. Labrie, P. L. Lim, F. Pierfederici, A. Pontzen, A. Ptak, B. Refsdal, M. Servillat, and O. Streicher. Astropy: A Community Python Package for Astronomy. *Astronomy and Astrophysics*, 558(A33):1–9, 2013.

[103] J. Ruan, N. Vieira, D. Haggard, M. R. Drout, N. Asfari, R. Carlberg, R. Doyon, R. Fernandez, B. Gaensler, V. Kaspi, D. Lafreniere, C. Matzner, D-S. Moon, C. Ni, M. Nynka, A. L. Piro, S. Safi-Harb, and K. Spekkens. LIGO/Virgo S190814bv: A Potential Faint Optical Counterpart in CFHT Imaging. NASA GCN 25443, 2019.

[104] B. Sánchez, M. J. Domínguez R., M. Lares, M. Beroiz, J. B. Cabral, S. Gurovich, C. Quinones, R. Artola, C. Colazo, M. Schneiter, C. Girardini, M. Tornatore, J. L. Nilo Castellón, D. García Lambas, and M. C. Díaz. Machine Learning on Difference Image Analysis: A Comparison of Methods for Transient Detection. *Astronomy and Computing*, 28(100284):1–17, 2019.

[105] V. Savchenko, S. Mereghetti, C. Ferrigno, E. Kuulkers, A. Bazzano, E. Bozzo, T. J.-L. Courvoisier, S. Brandt, R. Diehl, L. Hanlon, P. Laurent, A. Lutovinov, J.P. Roques, R. Sunyaev, and P. Ubertini. LIGO/Virgo G298048: INTEGRAL Detection of a Prompt Gamma-Ray Counterpart. NASA GCN Circular 21507, 2017.

[106] E. F. Schlafly and D. P. Finkbeiner. Measuring Reddening with Sloan Digital Sky Survey Stellar Spectra and Recalibrating SFD. *The Astrophysical Journal*, 737(103):1–13, 2011.

[107] L. P. Singer and L. R. Price. Rapid Bayesian Position Reconstruction for Gravitational-Wave Transients. *Physical Review D*, 93(2):1–24, 2016.

[108] M. Soares-Santos, J. Annis, A. Garcia, K. Herner, A. Palmese, D. Tucker, S. Allam, R. Morgan, T. Bachmann, N. Sherman, C. Martinez, and T. Davis. LIGO/Virgo S190814bv: Further Candidates from DESGW. NASA GCN 25425, 2019.

[109] M. Soares-Santos, J. Annis, A. Garcia, K. Herner, A. Palmese, D. Tucker, S. Allam, R. Morgan, T. Bachmann, N. Sherman, C. Martinez, T. Davis, and M. Butner. LIGO/Virgo S190814bv: New Candidate from DESGW. NASA GCN 25438, 2019.

[110] E. Symbalisty and D. N. Schramm. Neutron Star Collisions and the r-Process. *Astrophysical Letters*, 22(4):143–145, 1982.

[111] N. R. Tanvir, A. J. Levan, A. S. Fruchter, J. Hjorth, R. A. Hounsell, K. Wiersema, and R. L. Tunnicliffe. A 'Kilonova' Associated with the Short-Duration Gamma-Ray Burst GRB 130603B. *Nature*, 500(7464):547–549, 2013.

[112] N. R. Tanvir, A. J. Levan, C. González-Fernández, O. Korobkin, I. Mandel, S. Rosswog, J. Hjorth, P. D'Avanzo, A. S. Fruchter, C. L. Fryer, T. Kangas, B. Milvang-Jensen, S. Rosetti, D. Steeghs, R. T. Wollaeger, Z. Cano, C. M. Copperwheat, S. Covino, V. D'Elia, A. de Ugarte Postigo, P. A. Evans, W. P. Even, S. Fairhurst, R. Figuerra Jaimes, C. J. Fontes, Y. I. Fujii, J. P. U. Fynbo, B. P. Gompertz, J. Greiner, G. Hodosan, M. J. Irwin, P. Jakobsson, U. G. Jørgensen, D. A. Kann, J. D. Lyman, D. Malesani, R. G. McMahon, A. Melandri, P. T. O'Brien, J. P. Osborne, E. Palazzi, D. A. Perley, E. Pian, S. Piranomonte, M. Rabus, E. Roi, A. Rowlinson, S. Schulze, P. Sutton, C. C. Thöne, K. Ulaczyk, D. Watson, K. Wiersema, and R. A. M. J. Wijers. The Emergence of a Lanthanide-Rich Kilonova Following the Merger of Two Neutron Stars. *The Astrophysical Journal Letters*, 848(L27):1–13, 2017.

[113] J. H. Taylor, L. A. Fowler, and P. M. McCulloch. Measurements of General Relativistic Effects in the Binary Pulsar PSR1913+16. *Nature*, 277(5696):437–440, 1979.

[114] D. M. Terndrup, J. H. Elias, B. Gregory, S. R. Heatcote, M. M. Philips, N. B. Suntzeff, and R. E. Williams. Optical and Infrared Observations of SN 1987A from Cerro Tololo. *Proceedings of the Astronomical Society of Australia*, 7:412–423, 1988.

[115] D. Tody. The IRAF Data Reduction and Analysis System. *Proceedings of the Society of Photo-Optical Instrumentation Engineers, Instrumentation in Astronomy VI*, 0627, 1986.

[116] P. Tremblin, N. Schneider, V. Minier, G. Al. Durand, and J. Urban. A Worldwide Comparison of the Best Sites for Submillimetre Astronomy. *Astrophysics from Antarctica, Proceedings of the International Astronomical Union, IAU Symposium*, 288:29–33, 2013.

[117] E. Troja, L. Piro, T. Sakamoto, S. B. Cenko, and A. Lien. LIGO/Virgo G298048: Discovery of X-ray Emission from SSS17a in NGC4993. NASA GCN Circular 21765, 2017.

[118] S. Valenti, D. J. Sand, S. Yang, E. Cappellaro, L. Tartaglia, A. Corsi, S. W. Jha, D. E. Reichart, J. Haislip, and V. Kouprianov. The Discovery of the Electromagnetic Counterpart of GW170817: Kilonova AT 2017gfo/DLT17ck. *The Astrophysical Journal Letters*, 848(L24):1–6, 2017.

[119] S. Valenti, S. Yang, D. Sand, L. Tartaglia, E. Cappellaro, D. Reichart, J. Haislip, and V. Kouprianov. LIGO/Virgo G298048: DLT40 Optical Candidate. NASA GCN Circular 21531, 2017.

[120] P. G. van Dokkum. Cosmic-Ray Rejection by Laplacian Edge Detection. *The Publications of the Astronomical Society of the Pacific*, 113(789):1420–1427, 2001.

[121] J. van Paradijs, P. J. Groot, T. Galama, C. Kouveliotou, R. G. Strom, J. Telting, R. G. M. Rutten, G. J. Fishman, C. A. Meegan, M. Pettini, N. Tanvir, J. Bloom, H. Pedersen, H. U. Nørgaard-Nielsen, M. Linden-Vørnie, J. Melnick, G. Van der Steene, M. Bremer, R. Naber, J. Heise, J. in't Zand, E. Costa, M. Feroci, L. Piro, F. Frontera, G. Zavattini, L. Nicastro, E. Palazzi, K. Bennett, L. Hanlon, and A. Parmar. Transient Optical Emission from the Error Box of the Gamma-Ray Burst of 28 February 1997. *Nature*, 386(6626):686–689, 1997.

[122] S. Veilleux. CCD Gain Lab. ASTR310: Observational Astronomy, 2006.

[123] V. A. Villar, J. Guillochon, E. Berger, B. D. Metzger, P. S. Cowperthwaite, M. Nicholl, K. D. Alexander, P. K. Blanchard, R. Chornock, T. Eftekhari, W. Fong, R. Margutti, and P. K. G. Williams. The Ccombined Ultraviolet, Optical, and Near-Infrared Light Curves of the Kilonova Associated with the Binary Neutron Star Merger GW170817: Unified Data Set, Analytic Models, and Physical Implications. *The Astrophysical Journal Letters*, 851(L21):1–12, 2017.

[124] J. Weber. Detection and Generation of Gravitational Waves. *Physical Review*, 117(1): 306–313, 1960.

[125] D. C. Wells, E. W. Greisen, and R. H. Harten. FITS - a Flexible Image Transport System. *Astronomy and Astrophysics Supplement*, 44:363–370, 1981.

[126] R. M. West, A. Lauberts, H. E. Jørgensen, and H.-E. Schuster. Astrometry of SN 1987A and Sanduleak-69 202. *Astronomy and Astrophysics*, 177:L1–L3, 1987.

[127] D. J. White, E. J. Daw, and V. S. Dhillon. A List of Galaxies for Gravitational Wave Searches. *Classical and Quantum Gravity*, 28(8):1–13, 2011.

[128] A. E. Whitford. Advantages and Limitations of the Photoelectric Cell in Astronomy. *Publications of the Astronomical Society of the Pacific*, 52(308):244–249, 1940.

[129] S. Yang, S. Valenti, D. Sand, L. Tartaglia, E. Cappellaro, D. Reichart, and J. Haislip. LIGO/Virgo G298048: Continued Observation for DLT17ck. NASA GCN Circular 21579, 2017.

APPENDIX A

APPENDIX A

OBSERVATION FIELDS

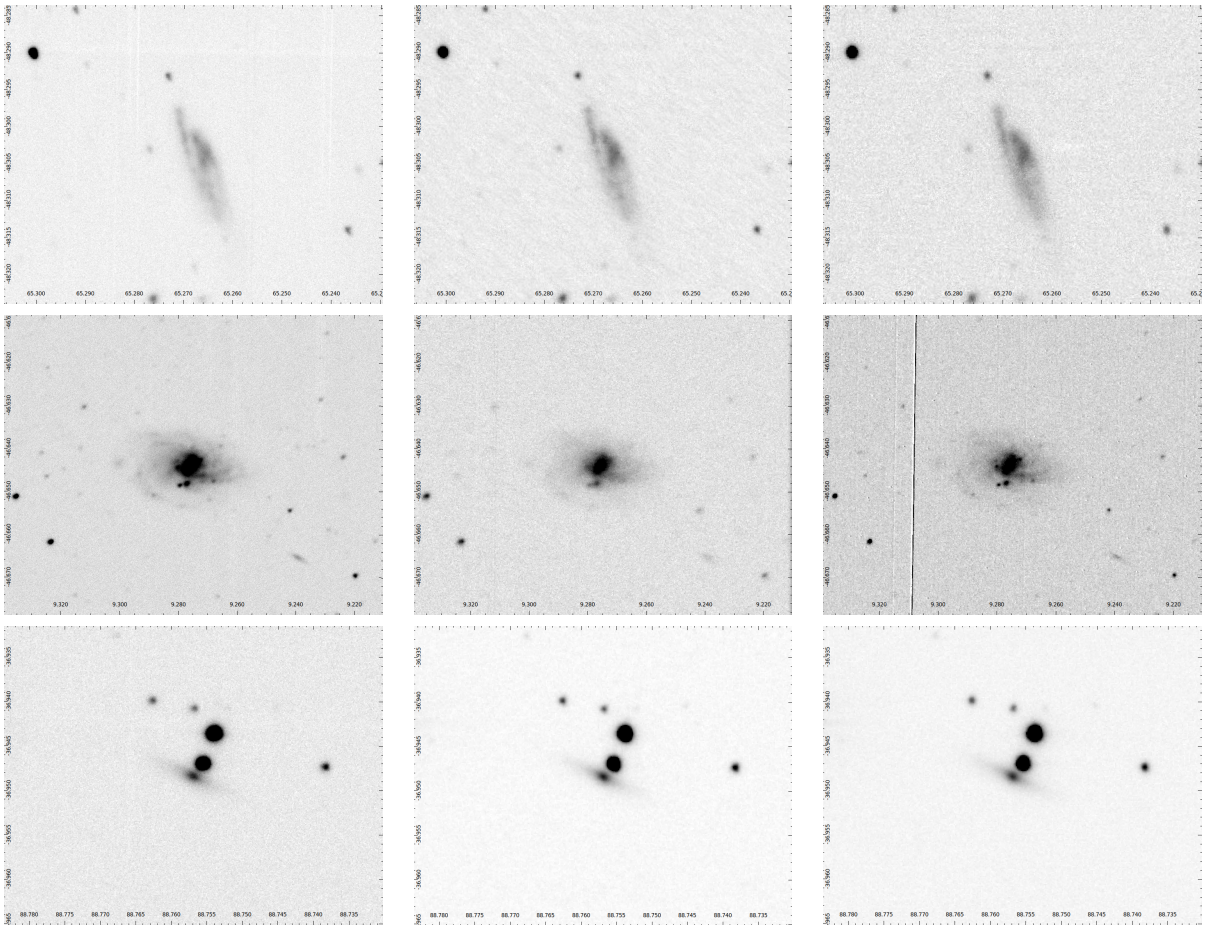

Figure A.1: Stacks from 1.54-meter EABA reflector for GW170104. From top to bottom is ESO 202-009 on 14 Jan (50×60), 16 Nov (40×40), 18 Nov (10×60); ESO 242-018 on 15 Jan (6×60), 18 Nov (20×30), 19 Nov (20×30); ESO 364-014 on 13 Jan (6×60), 16 Nov (21×30), 18 Nov (21×30).

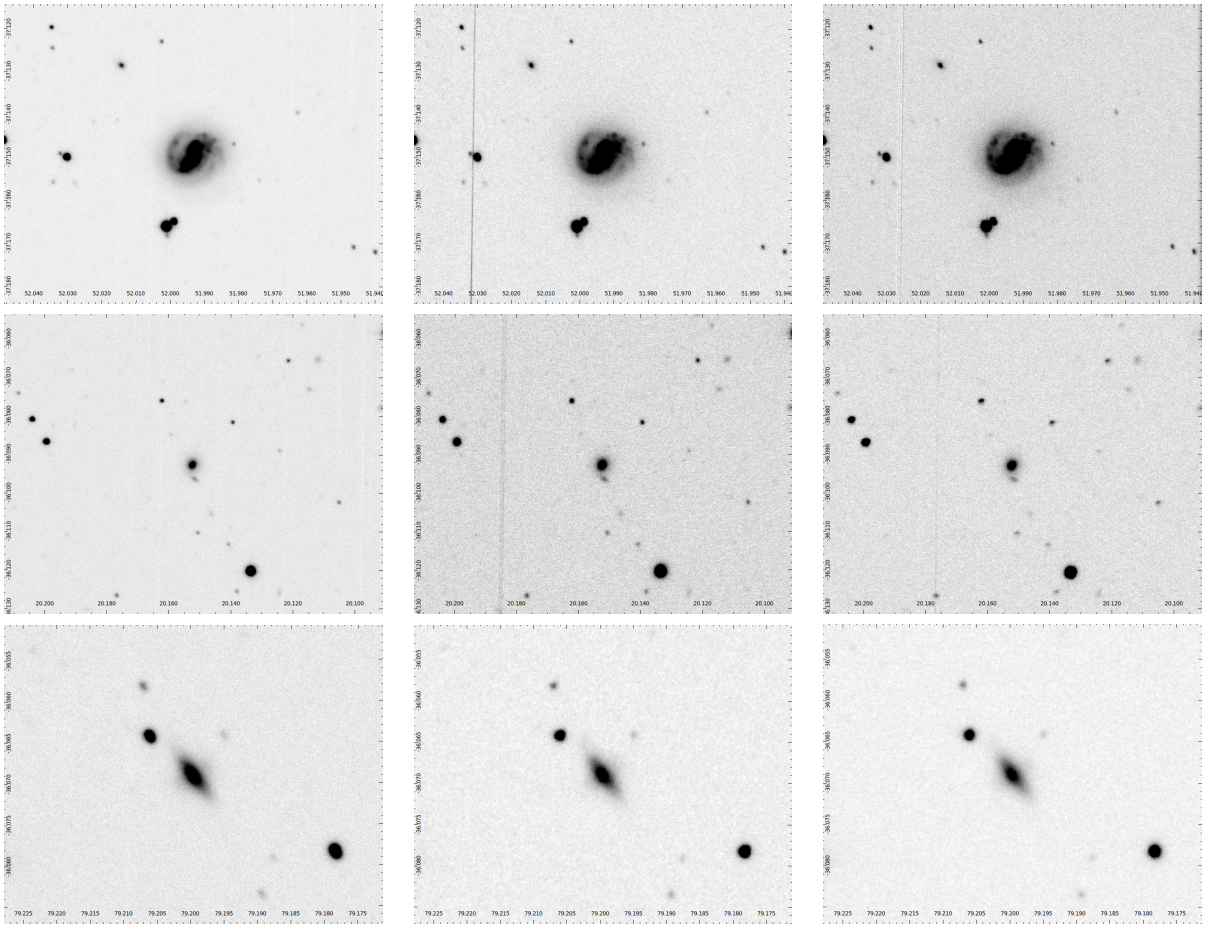

Figure A.2: Stacks from 1.54-meter EABA reflector for GW170104. From top to bottom is NGC 1341 on 13 Jan (51×60), 16 Nov (20×30), 19 Nov (20×30); PGC 073926 on 13 Jan (41×60), 16 Nov (20×30), 18 Nov (10×60); PGC 147285 on 14 Jan (22×60), 16 Nov (20×30), 18 Nov (20×30).

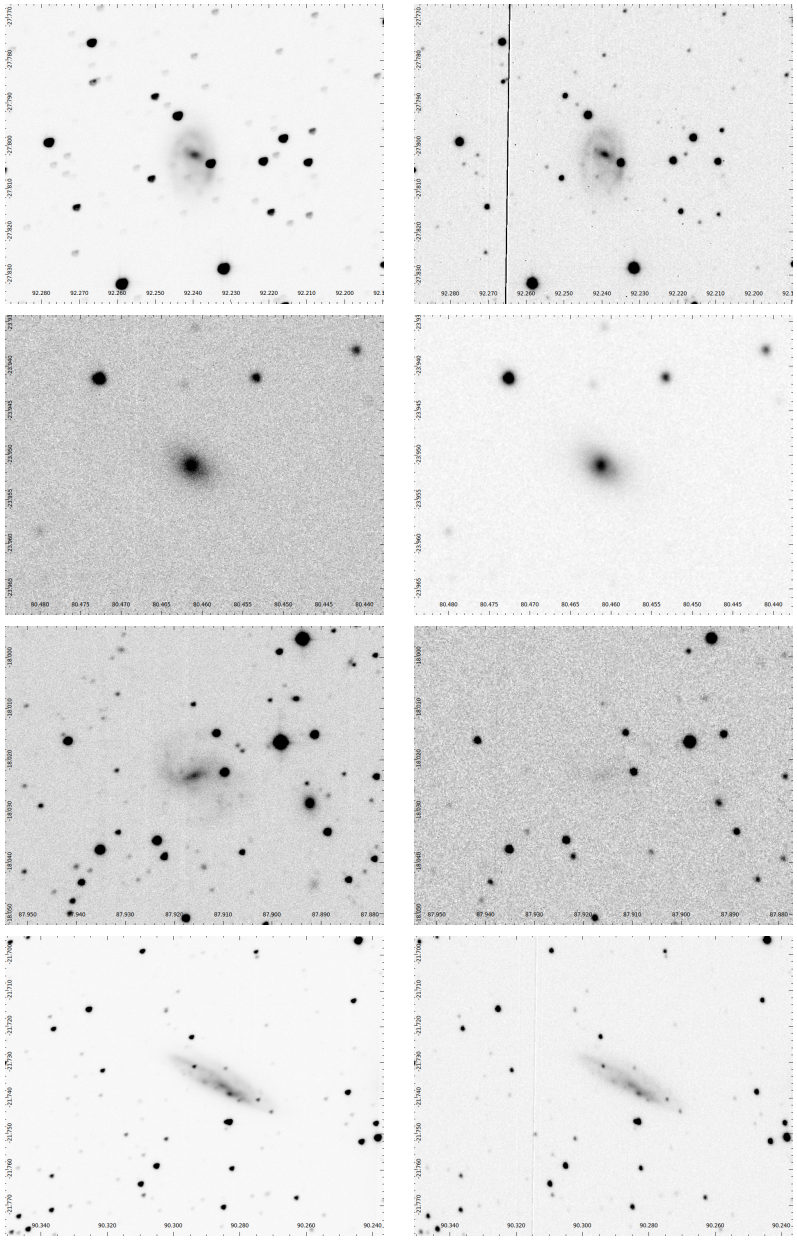

Figure A.3: Stacks from 1.54-meter EABA reflector for GW170104. From top to bottom is ESO 425-010 on 15 Jan (44×60) and 19 Nov (21×30); ESO 487-003 on 13 Jan (6×60) and 18 Nov (29×30); ESO 555-005 on 15 Jan (29×90) and 19 Nov (6×120); ESO 555-022 on 15 Jan (16×150) and 19 Nov (21×30).

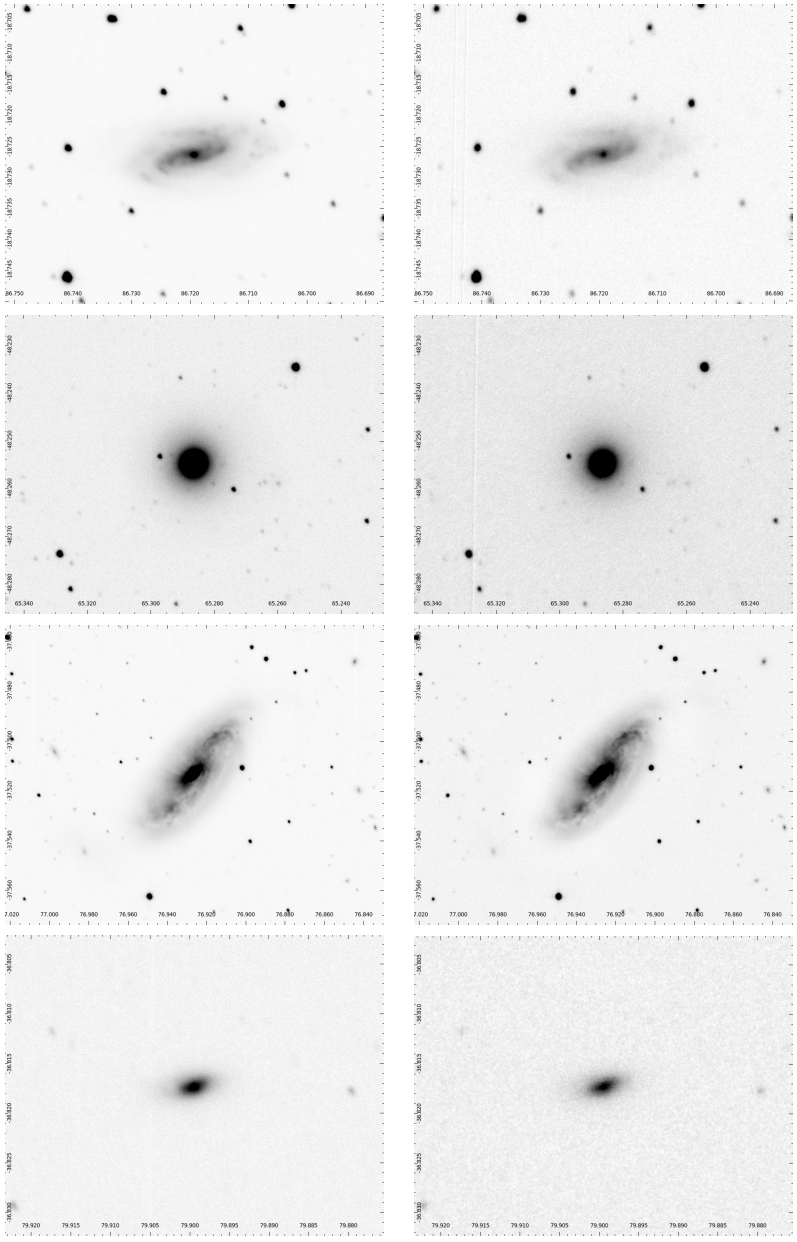

Figure A.4: Stacks from 1.54-meter EABA reflector for GW170104. From top to bottom is IC 2143 on 15 Jan (45×60) and 19 Nov (20×30); NGC 1567 on 15 Jan (13×120) and 16 Nov (40×30); NGC 1808 on 13 Jan (67×60) and 18 Nov (20×30); PGC 3080859 on 15 Jan (46×60) and 18 Nov (20×30).

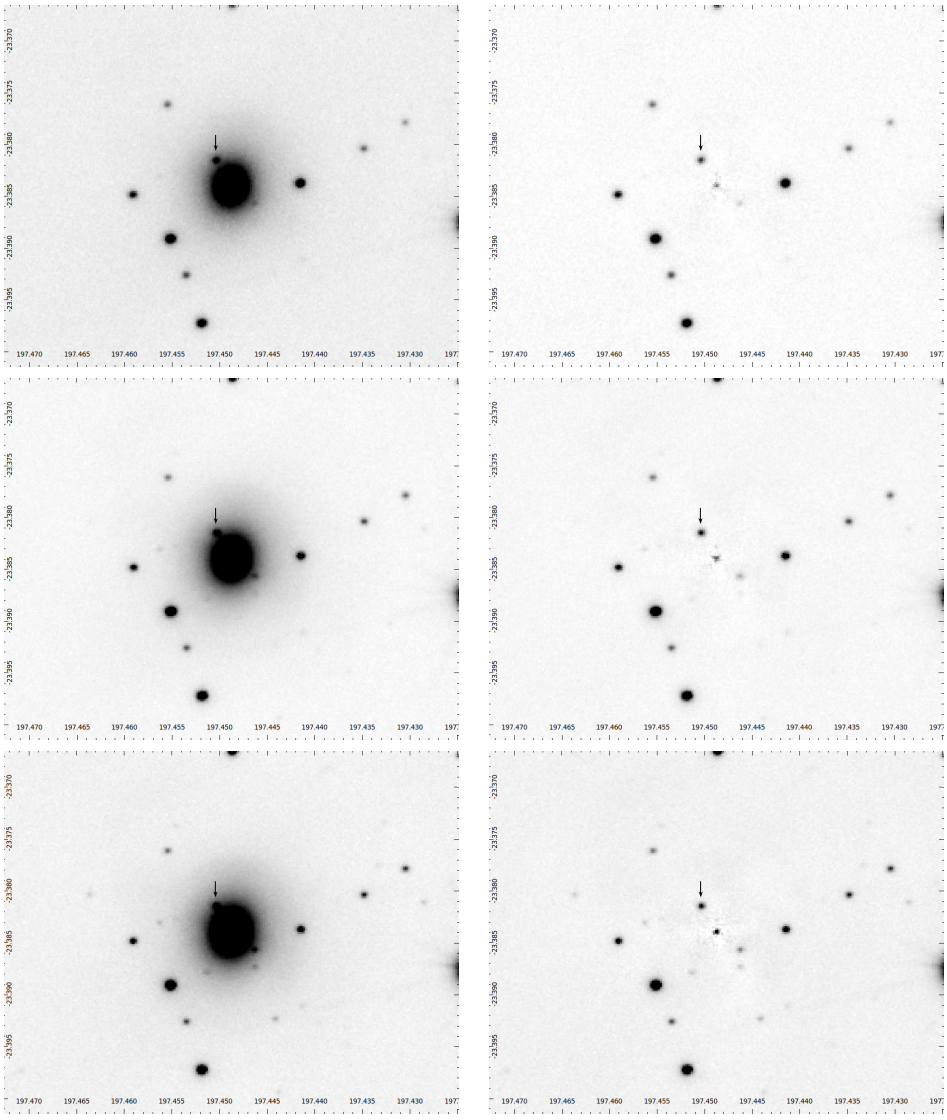

Figure A.5: Stacks of NGC 4993 by 0.83-meter T80S reflector on 18 August 2017 in *g*, *r*, and *i* bands (top to bottom), along with corresponding residual frames with subtracted host galaxy. The transient AT2017gfo is marked with an arrow.

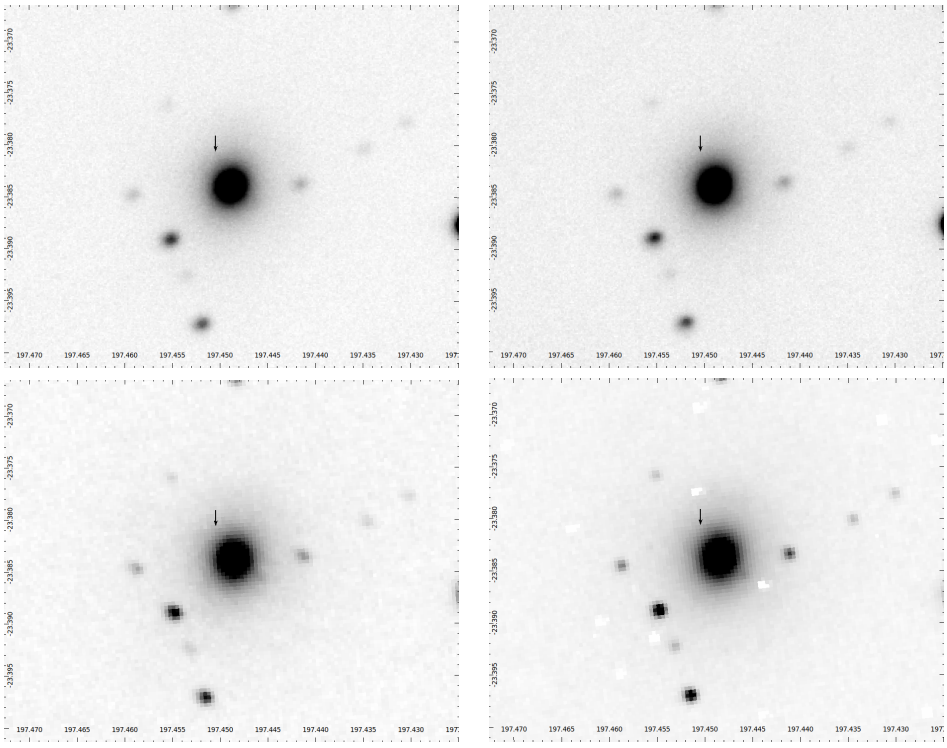

Figure A.6: Reference stacks of NGC 4993 by 1.54-meter EABA reflector on 4-5 September 2017 (top) and 17" CTMO astrograph on 1-2 July 2019 (bottom). The location of transient AT2017gfo is marked with an arrow.

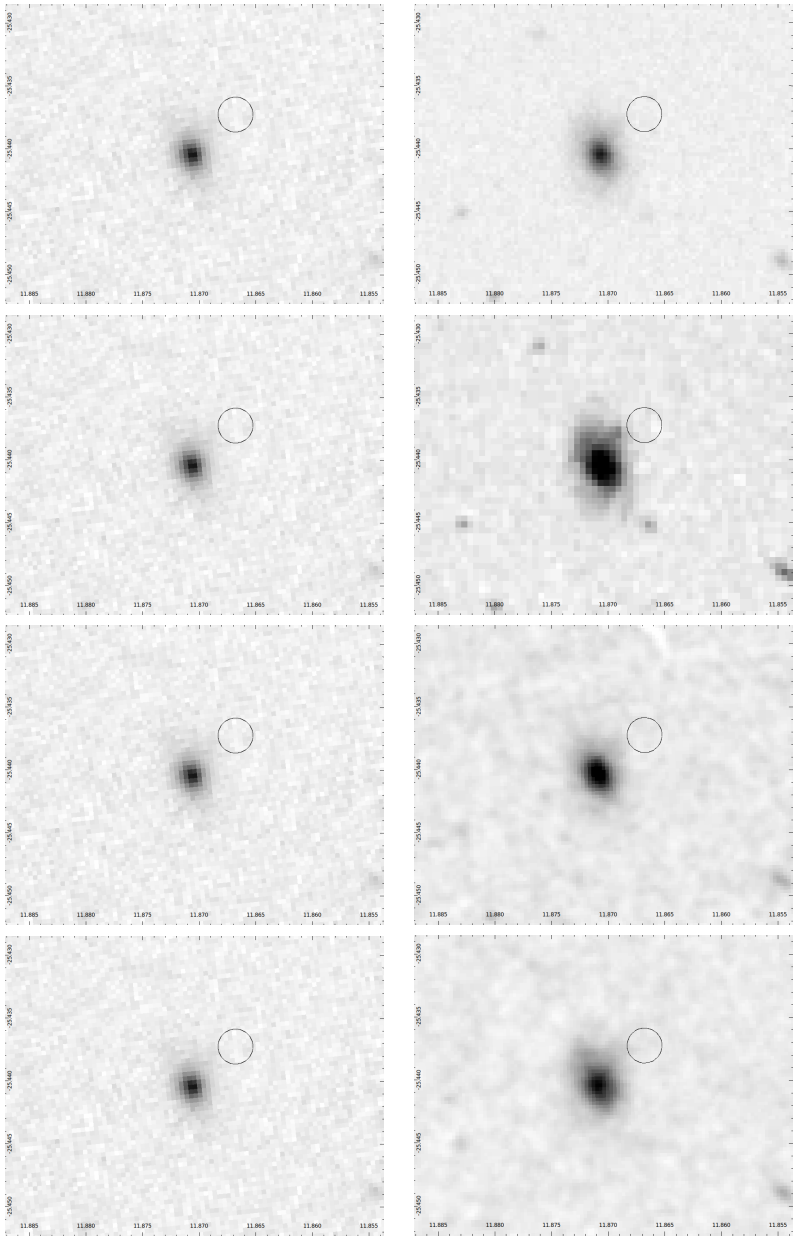

Figure A.7: Stacks from CTMO for S190814bv. The left column features the same image of 2MASX J00472894-2526263 taken by the CTMO 17" astrograph on 21 August 2019 (5×200 stack). The right column, from top to bottom, features reference images in the (1) POSS-II F-band, (2) POSS-II j-band, (3) POSS-I F-band, and (4) POSS-I j-band.

APPENDIX B

APPENDIX B

TABULATED PHOTOMETRY AT2017gfo

Time [JD - 2457984]	Magnitude	σ [mag]
0.675868	18.9	0.1
0.681551	19.12	0.09
0.682650	18.83	0.06
0.683727	18.88	0.06
0.691875	18.92	0.05
0.692975	18.95	0.04
0.694062	18.96	0.04
0.702072	19.05	0.04
0.703160	18.99	0.04
0.704225	19.01	0.04
0.712234	19.05	0.05
0.713322	19.00	0.04
0.714387	19.02	0.04
0.722338	19.20	0.05
0.723437	18.92	0.04
0.724514	18.97	0.04

Table B.1: Time series photometry in the SDSS *g*-band of the transient AT2017gfo from T80S data taken on 2017-08-18 UTC.

Time [JD - 2457984]	Magnitude	σ [mag]
0.684954	18.22	0.04
0.686042	18.29	0.03
0.687130	18.19	0.03
0.695266	18.14	0.03
0.696354	18.28	0.03
0.697419	18.34	0.03
0.705394	18.27	0.03
0.706493	18.14	0.03
0.707581	18.27	0.03
0.715556	18.27	0.03
0.716655	18.30	0.03
0.717743	18.58	0.04
0.725694	18.34	0.03
0.726782	18.35	0.03
0.727882	18.25	0.03

Table B.2: Time series photometry in the SDSS *r*-band of the transient AT2017gfo from T80S data taken on 2017-08-18 UTC.

Time [JD - 2457984]	Magnitude	σ [mag]
0.688310	17.80	0.04
0.689410	17.94	0.04
0.690498	18.09	0.04
0.698634	18.03	0.03
0.699734	18.00	0.03
0.700822	18.03	0.04
0.708762	17.86	0.03
0.709861	18.17	0.04
0.710961	17.96	0.04
0.718924	18.42	0.04
0.720023	18.21	0.05
0.721111	18.08	0.04
0.729039	18.13	0.04
0.730139	18.28	0.04
0.731215	18.09	0.04

Table B.3: Time series photometry in the SDSS *i*-band of the transient AT2017gfo from T80S data taken on 2017-08-18 UTC.

APPENDIX C

APPENDIX C

CCD GROWTH CURVES

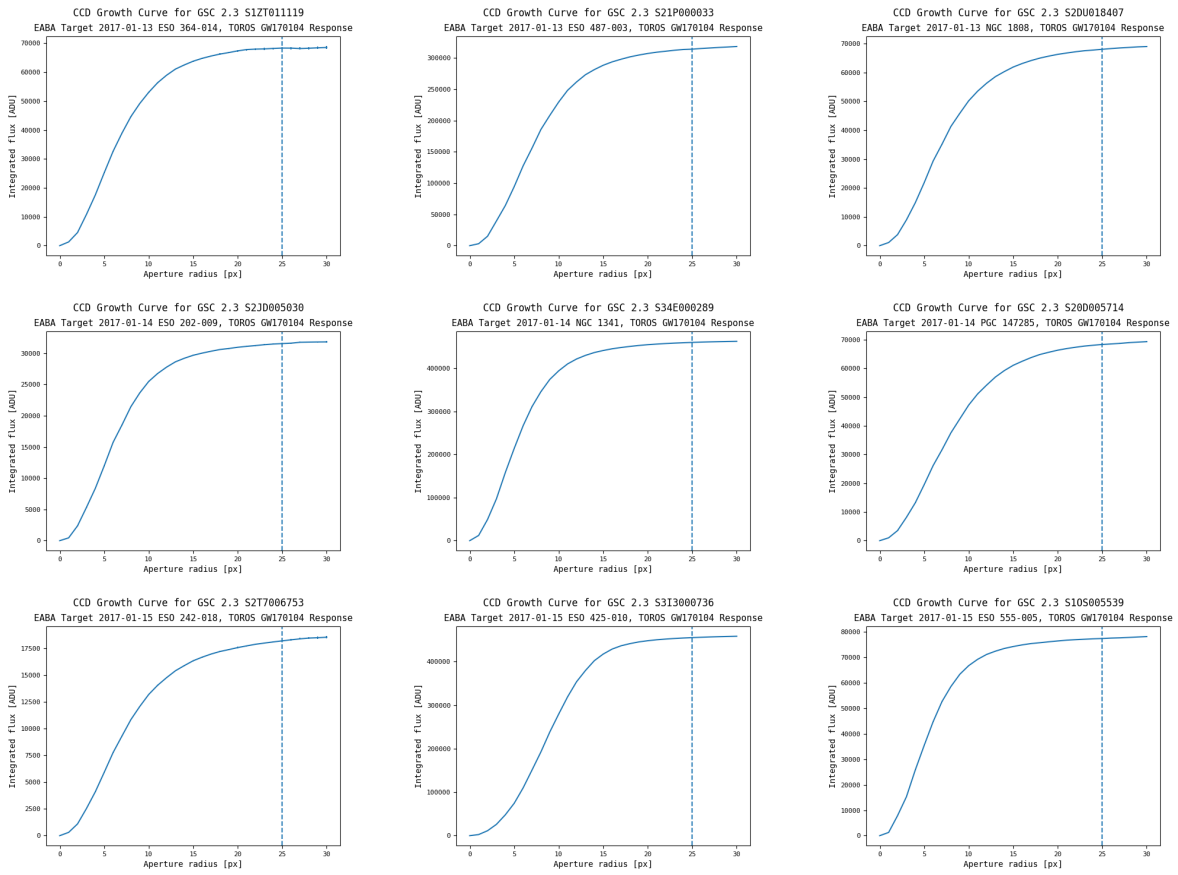

Figure C.1: Aperture curves of growth for test stars in EABA GW170104 target frames.

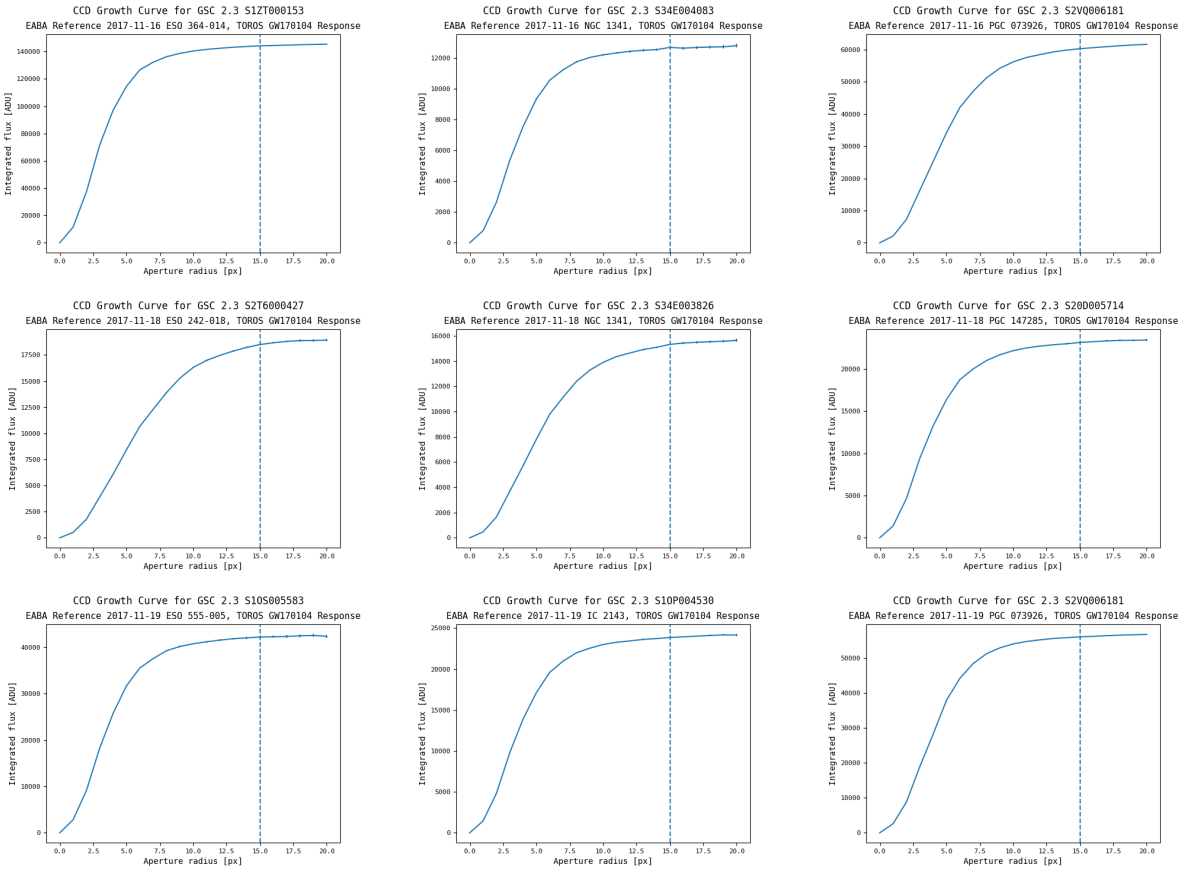

Figure C.2: Aperture curves of growth for test stars in EABA GW170104 reference frames.

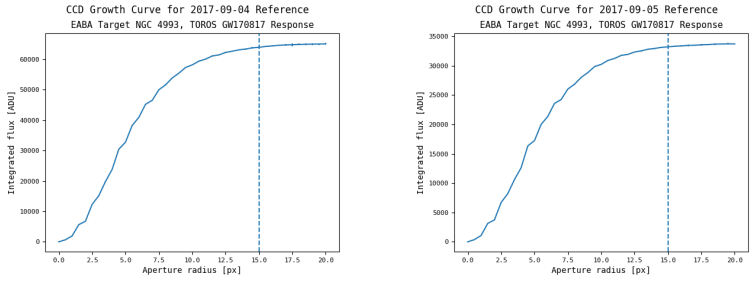

Figure C.3: Aperture curves of growth for averaged test stars in EABA GW170817 reference frames.

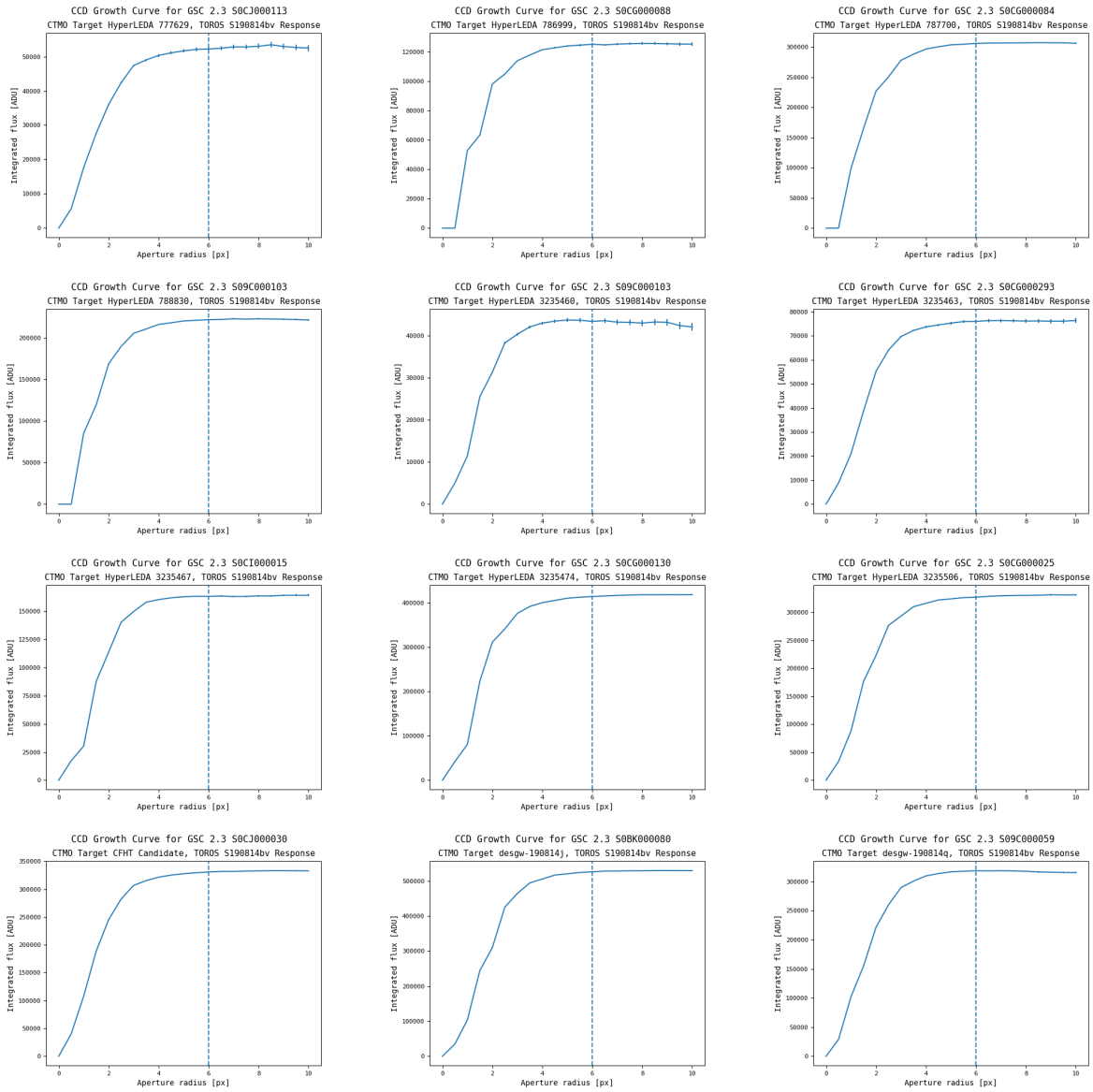

Figure C.4: Aperture curves of growth for test stars in CTMO S190814bv target frames.

APPENDIX D

APPENDIX D

CCD MEASUREMENTS

	STF-8300M	F16M	PL16803
Array size (px)	3326×2504	4096×4096	4096×4096
Dark current (e^-/px/s)	0.5 (0 C)	0.02	0.005 (35 C)
Full well capacity (e^-)	25500	95000	100000
Gain (ADU/e^-)	2.48 ± 0.01	0.699 ± 0.006	0.722 ± 0.006
Imaging area (mm)	17.96×13.52	36.8×36.8	36.8×36.8
Pixel size (μm)	5.4	9	9
Quantum efficiency (% @ 550 nm)	56	60	60
Read noise (ADU)	28.5 ± 0.5	9.7 ± 0.2	11.4 ± 0.2
Read noise (e^-)	11.5 ± 0.2	13.9 ± 0.4	15.8 ± 0.3
Sensor	KAF-8300	KAF-16803	KAF-16803
Temperature delta (C)	35 ± 0.1	45 ± 0.1	55 ± 0.1
Weight (kg)	0.8	1.9	2.6
Weight (lb)	1.8	4.2	5.9

Table D.1: Specifications for CTMO Generation 1 and 2 CCD cameras.

SBIG STF-8300M

The mean pixel value is plotted as a function of the variance in Figure D.1 for the SBIG STF-8300M. A weighted, linear fit to these data gives a measured gain of (2.48 ± 0.01) ADU/e^- and a measured readout noise of (28.5 ± 0.5) ADU or (11.5 ± 0.2) e^-. The linearity curve is plotted in Figure D.2 for the SBIG STF-8300M.

Apogee Alta F16M

The mean pixel value is plotted as a function of the variance in Figure D.3 for the Apogee Alta F16M. A weighted, linear fit to these data gives a measured gain of (0.70 ± 0.01) ADU/e^- and a measured readout noise of (9.7 ± 0.2) ADU or (13.93 ± 0.36) e^-. The linearity curve is plotted in Figure D.4 for the Apogee Alta F16M.

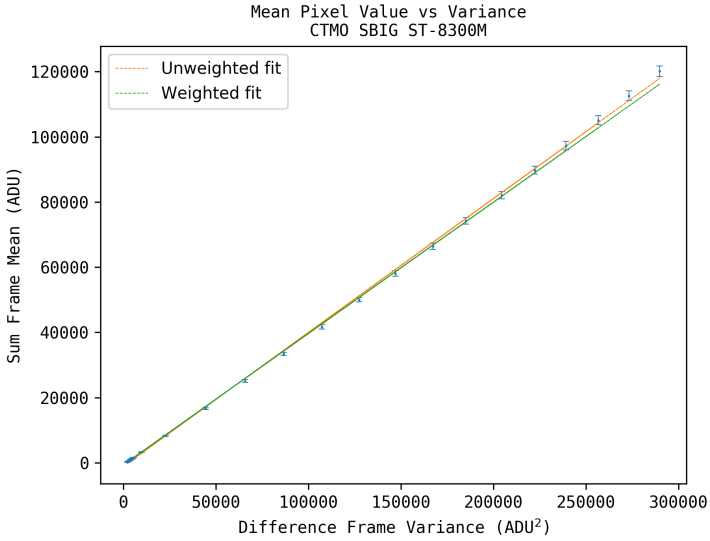

Figure D.1: Sum frame mean value versus difference frame variance for CTMO STF-8300M.

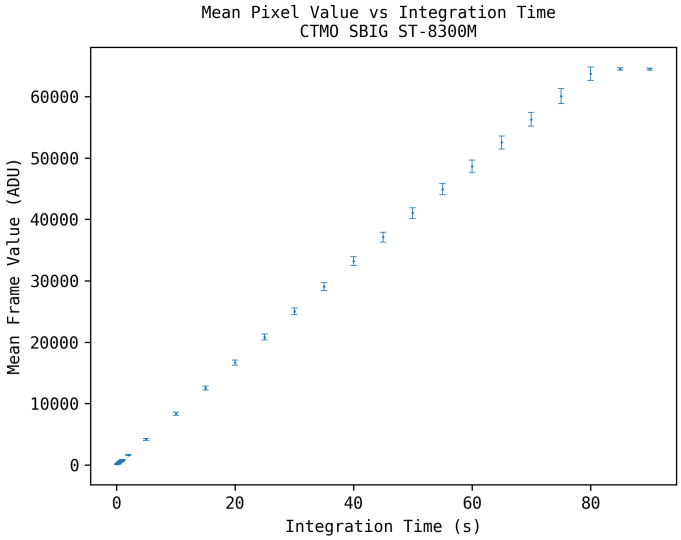

Figure D.2: Mean frame value versus integration time for CTMO STF-8300M.

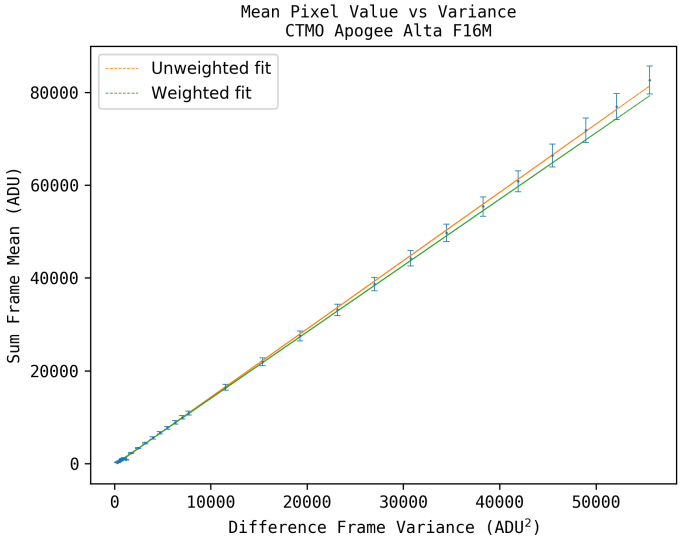

Figure D.3: Sum frame mean value versus difference frame variance for CTMO F16M.

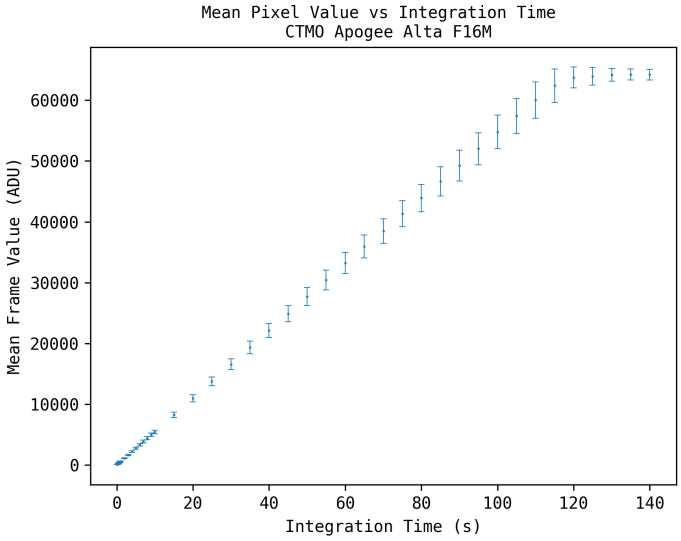

Figure D.4: Mean frame value versus integration time for CTMO F16M.

FLI PL16803

The mean pixel value is plotted as a function of the variance in Figure D.5 for the FLI PL16803. A weighted, linear fit to these data gives a measured gain of (0.72 ± 0.01) ADU/e^- and a measured readout noise of (11.4 ± 0.2) ADU or (15.8 ± 0.3) e^-. The linearity curve is plotted in Figure D.6 for the FLI PL16803.

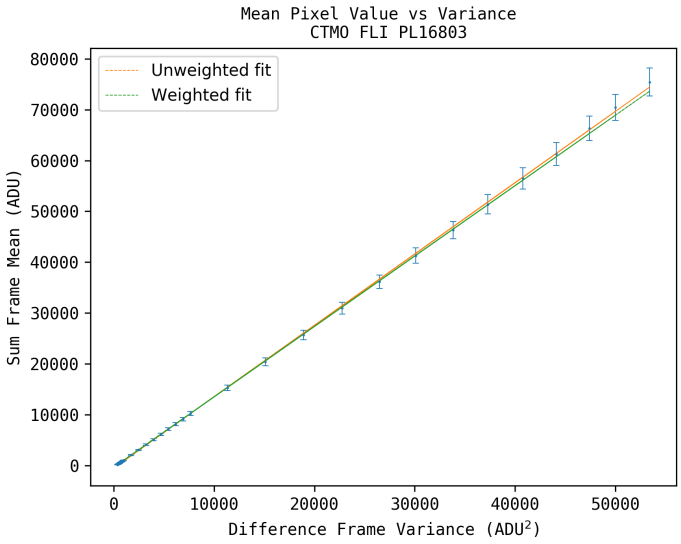

Figure D.5: Sum frame mean value versus difference frame variance for CTMO PL16803.

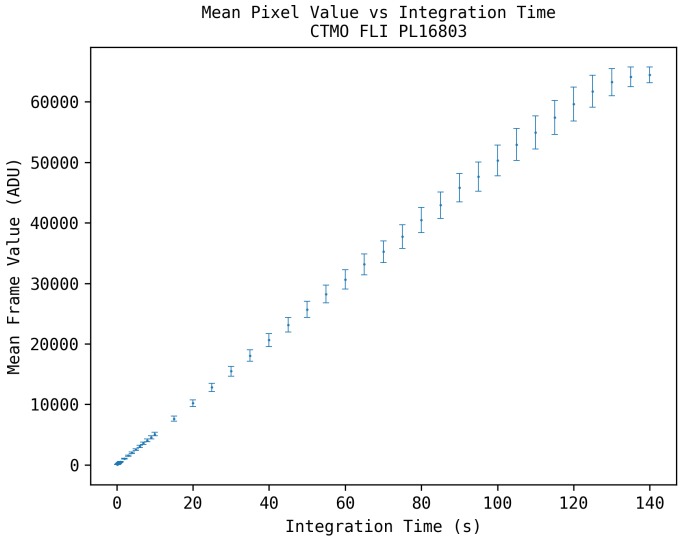

Figure D.6: Mean frame value versus integration time for the CTMO PL16803.

BIOGRAPHICAL SKETCH

Richard Camuccio is a native Pennsylvanian raised in rural Telford. He graduated from Souderton Area High School in 2012. He received a Bachelor of Arts in astrophysics from Franklin & Marshall College in 2016 and completed a thesis under Amy L. Lytle in experimental nonlinear optics. Richard was an observatory assistant at the Joseph R. Grundy Observatory in Lancaster, Pennsylvania.

Richard earned a Master of Science in physics from the University of Texas Rio Grande Valley in May 2020. He is assistant director of the Dr. Cristina Valeria Torres Memorial Astronomical Observatory in Brownsville, Texas. He is a member of the Transient Optical Robotic Observatory of the South Collaboration. He is a graduate research assistant at the Center for Gravitational Wave Astronomy and works in the Time Domain Astronomy Group and the Group for Advancing Instrumentation and Automation. Richard is a founding member of the South Texas Astronomical Society.

Email: richard.camuccio01@utrgv.edu